6. SITE 1067[1]

Shipboard Scientific Party[2]

HOLE 1067A

Position: 40° 40.950′N, 11° 35.750′W

Start hole: 2245 hr, 1 May 1997

End hole: 1815 hr, 10 May 1997

Time on hole: 211.5 hr (8.8 days)

Seafloor (drill pipe measurement from rig floor, mbrf): 5032.0

Total depth (drill pipe measurement from rig floor, mbrf): 5887.6

Distance between rig floor and sea level (m): 11.1

Water depth (drill pipe measurement from sea level, m): 5020.9

Penetration (mbsf): 855.6

Coring totals:

Type: RCB; Number: 23; Cored: 207.6 m; Recovered: 77.67 m; Average recovery: 37.4%

Sedimentary sequence:

Subunit IIB: (648.0–763.8 mbsf): claystone, calcareous claystone, calcareous siltstone to sandstone (middle Eocene to early(?)/late Paleocene)

(Note: this unit was numbered to be consistent with unit numbers defined during Leg 149 in the same area)

Basement:

Unit 1: (763.8–802.3 mbsf): strongly foliated amphibolite, tonalite gneiss

Unit 2: (801.9–822.6 mbsf): matrix-supported amphibolite breccia

Unit 3: (822.6–855.6 mbsf): foliated to weakly foliated amphibolite, meta-anorthosite

Principal results: Site 1067 lies in a water depth of 5021 m near the northern edge of the southern Iberia Abyssal Plain. The primary objective at this site was to drill and core down through acoustic basement (supposedly early postrift or synrift sediment or crystalline basement) to a strong extensive intrabasement reflector believed to represent a major synrift tectonic contact.

Coring commenced at 648 mbsf in Hole 1067A, and 115.8 m of sediment were drilled before basement rocks were encountered at 763.8 mbsf. The sediments are middle Eocene to early(?)/late Paleocene in age, and consist of claystones, calcareous claystones, calcareous silty claystones, and calcareous siltstones/sandy siltstones/sandstones. The cored interval is very similar to sediments of the same age recovered 800 m to the west at Site 900. The sediments drilled at Site 1067, therefore, are assigned to the lower part of Subunit IIB, as defined at Site 900. Upward-darkening units between 3 and 25 cm thick dominate the succession. They show a basal siltstone/sandstone overlain by calcareous claystone, and capped by claystone, and are interpreted as being deposited by turbidites close to the carbonate compensation depth (CCD), with evidence of some reworking by contour currents. Seismic reflection profiles in the Leg 149/Leg 173 area indicate that large-scale sedimentary structures produced by migrating seafloor bedforms related to contour currents are unequivocally present in Pleistocene to middle Eocene sediments. The sedimentological evidence from Site 1067 (and Site 900) shows that such currents were active at least as early as the late Paleocene. Cold Antarctic bottom waters would have been unlikely to have flowed over the west Iberia margin before the growth of an Antarctic ice sheet during the Oligocene. Therefore, during the Paleocene and Eocene, contour currents flowing along the west Iberia margin must have had another cause. A 2-cm-thick conglomerate horizon encountered in Paleocene sediments near the base of Subunit IIB contains 1- to 5-mm granules/pebbles of pale shallow-water limestones and dark gray pelite clasts that are similar in composition to clasts recovered in the Upper Jurassic and Miocene sediments drilled at Site 1065. Their presence suggests that metamorphic basement and Mesozoic shallow-water limestones were exposed in nearby uplifted areas, probably at the southern end of Galicia Bank about 15 km to the north.

Calcareous benthic foraminifers are commonly present throughout the section but are usually very small, being present in the size fraction below 125 µm. Agglutinated foraminifers occur sporadically. Planktonic foraminifers in the core-catcher samples vary in abundance and preservation; this is thought to be facies controlled. In the upper part of the sedimentary sequence, planktonic foraminifers are rare to few with poor to moderately good preservation, whereas in the lower part of the sequence the preservation is relatively poor. A few horizons of fossiliferous foraminiferal chalk have been identified. The interval between 658.4 and 763.8 mbsf is assigned a Paleogene age based on planktonic foraminiferal recovery. All Okada and Bukry (1980) calcareous nannofossil zones are accounted for, from Subzone CP13c (Zone NP15 of Martini, 1971) in Core 173-1067A-1R to Subzone CP8 (NP9) in Core 13R (representing early middle Eocene to late Paleocene). A Danian sample, which consisted of a pebble at the top of basement Core 173-1067A-14R, probably was not in place.

Basement was first recovered at a depth of 763.8 mbsf in Core 173-1067A-14R-1. The basement in general consists of strongly to weakly foliated amphibolite. Tonalite gneiss and weakly to moderately deformed meta-anorthosite occur as veins or patches distributed throughout the recovered sections. The basement has been divided into three units reflecting the dominant structural features. Unit 1 is found in Cores 173-1067A-14R-1 through 17R and consists of strongly foliated amphibolite (locally brecciated) with regions of tonalite gneiss and minor epidosite. Unit 2 starts at 801.9 mbsf in Core 173-1067A-18R and includes Core 173-1067A-19R and part of Core 173-1067A-20R. Matrix-supported amphibolite breccia is the dominant lithology throughout this unit, but amphibolite, tonalite gneiss to moderately deformed meta-anorthosite, and cataclasite also occur. Unit 3 starts within Section 173-1067A-20R-1 at 822.6 mbsf and continues through the bottom of Core 173-1067A-23R at 855.6 mbsf. Foliated to weakly foliated amphibolite occurs in this unit with disseminated meta-anorthositic veins and patches. Within the Unit 3 amphibolite, relict igneous textures (metagabbro) are preserved in Sections 173-1067A-23R-2 and 23R-3.

The foliation is weakly to clearly defined mainly by elongate amphibole crystals, plagioclase lenses, and quartz ribbons, depending on the mineralogy and the intensity of the deformation in the rocks. Dynamic recrystallization during shear deformation is extensive in quartz ribbons and is locally observed in plagioclase lenses. Deformation intensity appears to generally decrease downward. However, in the deepest section, there is a recurrence of well-developed foliation. The foliation dips steeply in the upper part of the cored section and shallows downhole (never less than 35°). Tonalite gneiss and meta-anorthosite occur as layers parallel or oblique to the foliation. Various types of folding occur throughout the section. Later fracturing is extensively but unevenly developed in the rocks. It led to a variety of veins filled mainly with epidote, chlorite, and calcite

[1]Whitmarsh, R.B., Beslier, M.-O., Wallace, P.J., et al., 1998. *Proc. ODP, Init. Repts.*, 173: College Station, TX (Ocean Drilling Program).

[2]Shipboard Scientific Party is given in the list preceding the Table of Contents.

Prior Chapter Contents Next Chapter

and evolved locally into brecciation, particularly in Unit 2. In places the veins appear to be randomly oriented, but elsewhere epidote and chlorite veins tend to have a shallow dip and are crosscut by steep calcite veins. Small-scale normal faults with steeply plunging slickensides occur throughout the section.

The physical properties of the claystones and sandstones fall into two distinct populations. Sandstone porosities are generally less than 20% and bulk densities are greater than 2.4 g/cm^3, while claystone (brown or green) porosities are greater than 20% and bulk densities are less than 2.4 g/cm^3. Several samples of mixed lithologies have intermediate properties. There is a local maximum in claystone density between ~680 and 700 mbsf of unknown cause. Compressional wave velocities in the claystones are reasonably constant (~2400 m/s), except for several higher measurements within the depth interval of increased density. Sandstone velocities appear to increase with depth from less than 4000 m/s at 650 mbsf to 5700 m/s at 714 mbsf. Below 714 mbsf the sand layers are increasingly mixed with clays and a pure sand end-member velocity was not measured. Cores 173-1067A-7R through 9R may be enriched in U, K, or Th; this interval roughly coincides with an increase of brown claystone relative to green claystone. Magnetic susceptibility increases downward starting with Core 9R. However, some changes in MST measurements, such as magnetic susceptibility and natural gamma-ray counts, may simply reflect fuller core liners, which will produce greater signal strengths. Bulk densities of basement rocks vary from about 2.5 to 3.0 g/cm^3. Grain densities are uniformly high and relatively constant about a mean of 2.95 g/cm^3. Porosity is generally 10% or less. Velocities appear to be lithology dependent; breccias are less than 5,000 m/s and amphibolites range from around 5,000 m/s to over 6,000 m/s, depending, most likely, on the amount of fracturing and alteration.

Methane concentrations in headspace gases were very low, varying from 2 to 5 ppm, and concentrations of other hydrocarbons and CO, CO_2, and H_2S were generally below detection limit. In Subunit IIB, calcareous siltstone/sandstone bases of turbidites generally have higher carbonate contents (mostly 45% to 65%) than associated overlying calcareous claystone (avg. 29%) and the darker claystones (avg. 7%) that mark the top of individual sequences. These data are consistent with the interpretation of turbidite emplacement close to or below the CCD, with accumulation of hemipelagic clay during the interval between individual turbidites. Subunit IIB sediments contain only trace amounts of organic carbon (avg. 0.1%), and the organic matter appears to have a marine origin.

Several magnetic polarity reversals are known to occur in the early/middle Eocene period during which most of the sediments were deposited. Pass-through measurements on the sediments yield dominantly positive inclinations (normal polarity) and indicate weak NRM intensities. Progressive alternating field (AF) and thermal demagnetization failed to substantiate any polarity changes and reveals a complex behavior. The data suggest the presence of multiple overprints that may be related to phases of magnetite reduction and iron-sulfide generation. Thus, it was not possible to construct a reliable magnetostratigraphy. Medium-grained metamorphosed mafic rocks from below 763.8 mbsf showed some resistance to AF demagnetization. The most potentially useful paleomagnetic results were obtained from thermal demagnetization of the discrete mini-core samples taken from long, continuous pieces of core. Preliminary results show both normal and reversed magnetic polarity. The thermal demagnetization data, however, indicate the magnetization is complex and renders any polarity evaluation suspect. The unblocking temperatures and coercivities indicate that the dominant magnetic mineral in these samples is magnetite. At this time, the age and origin of the magnetic signal in the basement rocks are not well understood.

BACKGROUND AND OBJECTIVES

Whereas the contribution of normal faults in the upper lithosphere to the rifting of continental margins has been known for almost 20 years (e.g., on the North Atlantic margins by de Charpal et al., 1978; Keen et al., 1987a, 1987b; Le Pichon and Barbier, 1987; Groupe Galice, 1979; Mauffret and Montadert, 1987; Montadert et al., 1979), the mode of lithospheric extension at deeper levels in rifted areas is still controversial because of the difficulty of obtaining information there. More recently, low-angle detachment faults have been recognized as major structural features accommodating postcollisional extension (e.g., Lister and Davis, 1989, in the Basin and Range). The development of such features was then assumed to occur during continental rifting and breakup (e.g., Lister et al., 1986; Wernicke, 1985; Wernicke and Burchfiel, 1982), and some low-angle tectonic contacts in the Alps were identified as Mesozoic, rifting-related detachment faults (Froitzheim and Eberli, 1990). Accordingly, the subhorizontal S reflector, which lies within, or at the base of, the continental crust under the northern Bay of Biscay and Galicia Bank margins (de Charpal et al., 1978), was interpreted as the seismic expression of a low-angle fault representing simple shear of the continental lithosphere or at least the brittle crust (Boillot et al., 1988; Le Pichon and Barbier, 1987; Reston et al., 1996; Sibuet, 1992). However, the initial lithospheric rheology and temperature are significantly different for postcollisional lithospheric stretching than for rifting of a previously stable continental lithosphere. Thus, in the first case, gravitational collapse is postulated to play an important role during post-collisional stretching, whereas it is absent during the rifting of a stable continental lithosphere. Therefore, other modes of lithospheric stretching and breakup at rifted continental margins were then proposed. For example, the S reflector was interpreted as the tectonic contact between the (upper?) crust and the mantle resulting from the development of conjugate shear zones in the ductile lower crust and upper mantle during necking of the whole lithosphere (Beslier and Brun, 1991; Brun and Beslier, 1996).

Although no such clear example of a low-angle tectonic reflector is known from the southern Iberia Abyssal Plain, several deeply penetrating reflectors with subhorizontal parts have been recognized recently on at least three east-west profiles (Beslier et al., 1995; Dean et al., 1996; Krawczyk et al., 1996; Pickup et al., 1996). Normally, such reflectors are deeply buried and inaccessible to the drill, but any opportunity to core through such a tectonic contact would yield valuable information on the petrologic and structural evolution of the rocks close to such a major extensional feature and on the physical contrasts that produce the reflections.

One such reflector has been interpreted to rise under the crest of a basement high within the ocean/continent transition of the southern Iberia Abyssal Plain. The high is crossed by the east-west multichannel seismic reflection profile Lusigal-12, which shows at least two strong reflectors, labeled L and H, within the acoustic basement (Krawczyk et al., 1996; Fig. 1). The H reflector in particular rises toward, and possibly intersects, the crest of the basement high. Prestack depth migration in the vicinity of the crest of the high has been interpreted to suggest that a shallow eastward-dipping reflector, which appears to intersect the top of the acoustic basement, can be extrapolated downward to join the rising H reflector through a steeper zone in which the continuity of H is unclear (Krawczyk et al., 1996; Fig. 10, "Introduction" chapter, this volume). In this interpretation, the acoustic basement immediately east of the shallow reflector is regarded as upper plate and that to the west as lower plate. Recognizing the inherent difficulty and assumptions in producing such an image, Site 1067 was chosen on the basement high where the seismic image seemed to be both clearest and simplest (Fig. 10, "Introduction" chapter, this volume).

The principal objective of Site 1067 was to core through an uppermost basement layer of possible upper continental crust, or early synrift or prerift sediments, and then to pass through the H reflector to sample the underlying rocks (Fig. 10, "Introduction" chapter, this volume), with a view to determining their nature and to determine petrostructural evolution at, and above and below, the tectonic contact and the physical explanation for its reflective character. The

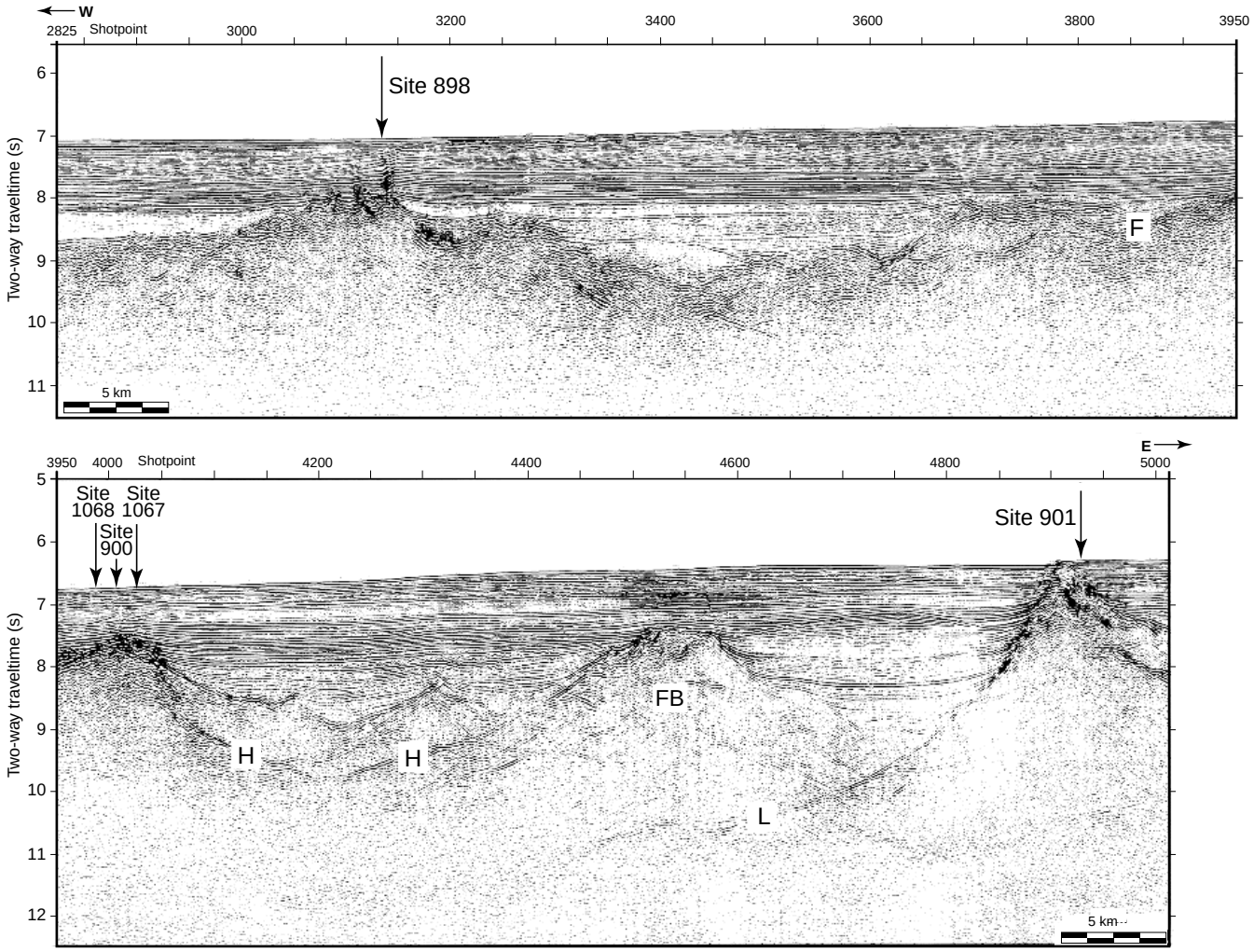

Figure 1. Lusigal-12 time-migrated section (from Krawczyk et al., 1996). H and L = intrabasement reflectors; F = fault; FB = fault block. See Figure 3 for location.

overlying basement layer was estimated to be 400 m thick on the seismic depth section, based on an interval velocity of 4.0 km/s derived from depth-focusing error analysis (C.M. Krawczyk, pers. comm., 1995). The H reflector appears to crosscut the top of the basement a short distance to the west of the site in the vicinity of Site 900 (Sawyer et al., 1994). We expected the underplated(?) synrift gabbro cored there to come from the lower plate to H. Two other nearby seismic lines (CAM 146 and CAM 159) also image H and have been prestack depth migrated, too, but the images near the top of basement are less clear (Fig. 2; see Figs. 65 and 66 in Appendix, this chapter).

Site 1067 lies in a water depth of 5021 m near the northern edge of the southern Iberia Abyssal Plain (Fig. 3). The contoured basement chart (Fig. 4) shows that the site lies on a triangular local high on a more elongated ridge at least 22 km long, which trends roughly north-northeast. The site is crossed by an east-west seismic reflection profile, Lusigal-12, that has been time and depth migrated (Figs. 1, 2; Fig. 10, "Introduction" chapter, this volume); the north-south Sonne-21 line passes about 550 m west of the site (Figs. 2, 5). The site was picked at shotpoint 4020 on profile Lusigal-12 but the borehole location was shifted back (westward) along *Le Suroît*'s track by 70 m to allow for the offset between the watergun array and the ship's GPS aerial. At SP4020 on the time section there is 0.74 s TWT (710 m) of postrift sediment, and on the depth section there is ~750 m of postrift sediment. Therefore, we expected to encounter 710–750 m of postrift sediments (presumed to be turbidites and pelagites by analogy with Site 900, which lies 800 m to the west) and about 400 m of upper continental crust, or early synrift or prerift sediments, before penetrating the H reflector.

OPERATIONS

The vibration-isolated television (VIT) camera was left deployed while the ship was moved from Site 1066 to Site 1067 (proposed site IBERIA-09A). No subsea cables were visible on the seafloor. Hole 1067A was spudded at 0100 hr, 2 May 1997. It was at this time that the core technician noticed a spooling problem with the coaxial winch. While the ship was offset to the southwest in search of deeper water, an additional 30 m of line was paid out and the problem was corrected. After about 2.5 hours the ship was back on location and ready to re-spud the hole.

Hole 1067A was "officially" spudded at 0330 hr, 2 May 1997. The VIT was retrieved during a jet-in test to a depth of 5092.8 mbrf or 60.8 mbsf. Drilling with an RCB/center bit commenced at 0600 hr;

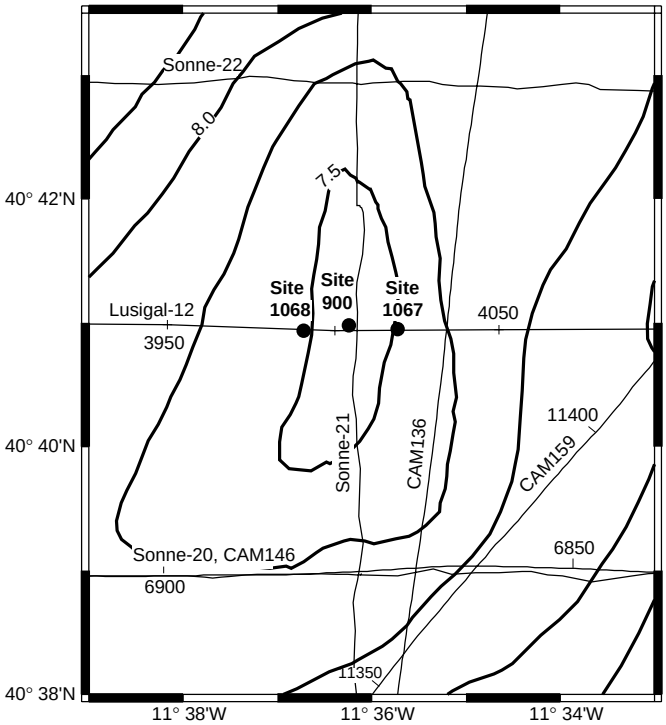

Figure 2. Basement contours (contour interval 0.25 s TWT, ~250 m) and tracks of multichannel seismic reflection profiles in the vicinity of Site 1067. Shotpoints are given for profiles in the Appendix.

however, 2.5 hours later, at a depth of 109.0 mbsf, the WKM valve developed a severe leak, causing the drilling operation to be halted for less than 2 hr. Drilling continued to a depth of 5680.0 mbrf averaging 14.5 m/hr. Drilling weight on bit was limited to 15,000 lb to prevent overloading/torquing the core barrel latch and latch sleeve. It required 44.75 hr to drill to 648.0 mbsf, including time to recover and inspect the center bit four times.

Continuous RCB coring began at this depth and, after encountering basement at approximately 764 mbsf, coring continued to 855.6 mbsf (Table 1). Between Cores 173-1067A-17R and 18R, a short trip of the drill string was required in order to replace 10 stands of drill pipe fitted with aluminum pipe protectors with standard 5-1/2-in pipe. Given the length of pipe that was removed, this short trip raised the bit to a level above that of the sediment-basement contact. A wash barrel was used while running the pipe back to the bottom of the hole, and Core 18R was taken using this same core barrel. Thus, the numerous claystone and siltstone pebbles at the top of Core 18R are almost certainly derived from sediments overlying the sediment-basement contact.

When coring had proceeded to 855.6 mbsf, the original core bit had 101.6 rotating hours and the rate of penetration for Core 23R was down to 0.9 m/hr. A sepiolite mud pill was circulated and the drill string was pulled to a depth of 185.0 mbsf. During the trip the only tight spot in the hole was encountered at a depth of 744.0 mbsf. After rigging and dropping a free fall funnel (FFF), the VIT was deployed. On the first attempt at pulling clear of the seafloor, the core bit snagged the casing joint on the FFF. The bit was immediately lowered back down hole ~9 m and another attempt was made. This time the bit came clear of the FFF without incident and at 0600 hr 9 May 1997 the bit cleared the sea floor. The VIT was retrieved as the pipe trip continued to the surface and the bit was on deck at 1400 hr.

A new bit and a rebuilt mechanical bit release (MBR) were being made up to the outer core barrel when a vertical crack ~2 in long was identified running down from the shoulder of the MBR box connection. The cracked MBR Top Connector, used previously in Hole 1065A, was replaced and the drill string was tripped to the seafloor. With the VIT deployed, the vessel maneuvered for 3.5 hr before reaching a position over the FFF. Reentry was made at 0415 hr. on 10 May 1997. At the time of reentry, vessel heave was causing the weight indicator to fluctuate 20,000–40,000 lb. Once inside the hole the drill string was lowered slowly until 0430 hr when the bit reached a depth of 80.0 mbsf. At this point the weight on the bit was 20,000–25,000 lb, indicating an obstruction.

The drill string could not be rotated or run in at normal speeds until the VIT was retrieved. Use of the heave compensator or rapid downward movement of the drill string could have jeopardized the safe recovery of the VIT system because of cable wraps around the drill pipe. While retrieving the VIT (~45 min), the string was worked up/down slowly three times with 20,000–25,000 lb weight in an attempt to pass the obstruction and place the BHA in a less vulnerable position. When the drill string was picked up the second time an approximate 20,000-lb loss in string weight was noted and the drill string was pulled back to 5102 mbrf where the circulating head was made up and circulation started. The drill string was not moved again until the camera frame was recovered.

After recovering the VIT frame, a rotary core barrel was run in on the wire line. If the BHA had been intact, the core barrel should have landed at 5108 mbrf. Instead, the barrel repeatedly landed at 5032 mbrf or 76 m above the landing point. This indicated that there had indeed been a failure in the BHA, most likely in a drill collar connection. The wire line was retrieved, the top drive set back, and the drill string was pulled back to the surface. While pulling pipe the beacon was released and subsequently recovered at 1745 hr on 10 May 1997. The BHA cleared the rotary table at 1815 hr that same day officially ending Hole 1067A.

A BHA failure was confirmed in the connection between 8-¼-in drill collars #7 and #8. While the vessel was moved in DP mode to Site 1068 (IBERIA-09C) the two remaining 8-¼-in drill collars and the tapered drill collar were inspected using magnetic particle techniques with no indications of any cracks. As a result of the BHA failure, Hole 1067A was abandoned short of the primary depth objective.

LITHOSTRATIGRAPHY

A simplified summary of the lithostratigraphy cored at this site and other Leg 173 and Leg 149 sites is shown in Figure 6. The succession drilled at Site 1067 is very similar to that of the same age found 800 m to the west at Site 900 (Shipboard Scientific Party, 1994a). Therefore we assign the sediments drilled at Site 1067 to the lower part of lithostratigraphic Subunit IIB as defined at Site 900.

The sedimentary section drilled at Hole 1067A consists of one lithostratigraphic subunit overlying basement. It is middle Eocene to late Paleocene in age and consists of claystones, calcareous claystones, calcareous silty claystones, calcareous siltstones/sandy siltstones, and rare nannofossil claystones.

Rotary coring (RCB) was employed in Hole 1067A, resulting in moderate recovery of the sediments of Subunit IIB (53%). Coring began within Subunit IIB at 648 mbsf, and terminated at 763.8 mbsf. Figure 7 summarizes the core recovery, lithologies, and ages of the lower part of lithostratigraphic Subunit IIB recognized in Hole 1067A. The ages, lithologic compositions, overall colors, facies and depositional environments, and cored intervals of Subunit IIB are summarized in Table 2.

Subunit IIB

Cores 173-1067A-1R-1, 0 cm, through 13R-CC, 21 cm
Depth: 648–763.8 mbsf
Age: middle Eocene to early(?)–late Paleocene

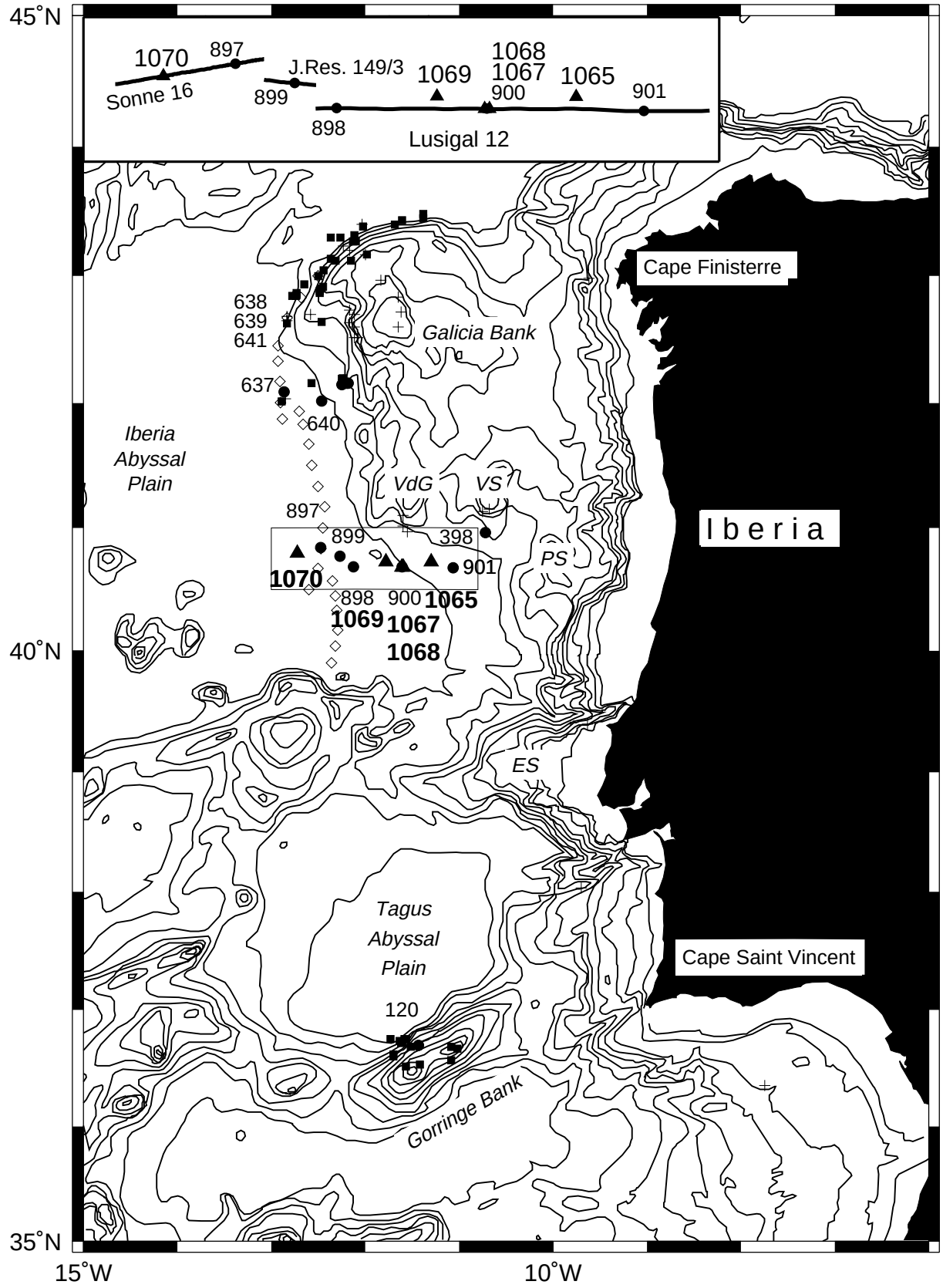

Figure 3. Contoured bathymetric chart of the West Iberia margin. Contours at 200, 500, 1000, 1500 through 5000 m. Leg 173 sites are shown by triangles with bold numbers; sites drilled on earlier legs are shown by solid circles. PS, VS, and VdG correspond to Porto, Vigo, and Vasco da Gama Seamounts, respectively. ES denotes the Estremadura Spur. Solid squares and crosses denote rock samples obtained by submersible and dredge, respectively. The inset is a composite of seismic tracks showing the relative locations of Leg 173 and other drill sites.

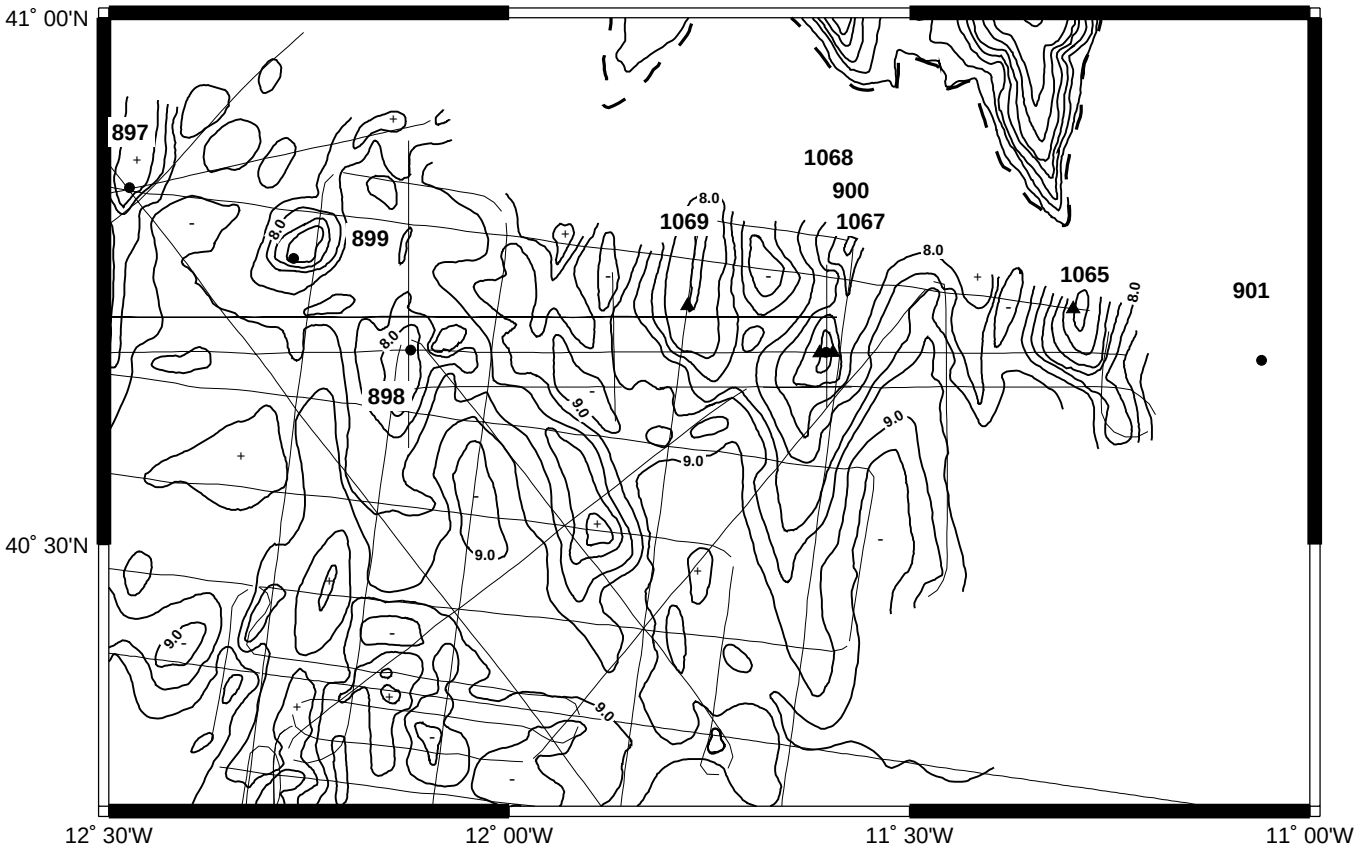

Figure 4. Contour chart of two-way traveltime (TWT) to basement (contour interval 0.25 s TWT m, ~250 m; contouring based on work by C.M. Krawczyk, L.M. Pinheiro, S.M. Russell, and R.B. Whitmarsh) combined with bathymetry of the relief bordering the Iberia Abyssal Plain (contour interval 250 m; courtesy J-C. Sibuet). Dashed line denotes edge of the abyssal plain. Leg 149 and Leg 173 sites are shown by solid circles and solid triangles, respectively. Fine lines are tracks of seismic lines used to contour basement. Selected basement highs and lows are indicated by + and –, respectively.

General Description

Core disturbance is generally slight to moderate, but in Sections 173-1067A-13R-2 and 13-CC strong biscuiting is present.

Subunit IIB (1067A-1R to 1067A-13R) is dominated by 3- to 25-cm-thick upward-darkening sequences of calcareous siltstone/sandstone, calcareous silty claystone, and claystone (Fig. 8). Some of these sequences show upward-fining, but in some cases there may be no grain-size change between the lighter colored, more carbonate-rich sediments and the overlying phyllosilicate claystones. Lighter colored lithologies contain higher proportions of carbonate than the darker ones (see Fig. 56). Because the upward-darkening sequence commonly, but not always, corresponds to an upward-fining, we have generally indicated these sequences with the upward-fining symbol on the barrel sheets (see Section 3). We used the symbol for "calcareous chalk" to represent calcareous claystone, as the AppleCORE program does not include a symbol for the latter lithology.

Minor lithologies include nannofossil claystone (identified in smear slides at Samples 173-1067A-7R-3, 8 cm, and 13R-1, 55, 87, and 107 cm, and in thin section at Sample 173-1067A-8R-1, 26–29 cm (Fig. 9D), and a 2-cm-thick matrix-supported conglomerate consisting of pebbles (1–5 mm) of pale limestone and dark gray pebbles (Sample 173-1067A-13R-1, 124–128 cm; Fig. 10).

Intervals of light gray calcareous siltstone to sandstone, 0.5 cm to 3 cm thick, typically occur at the bases of the upward-darkening sequences. They show a variety of features: massive bedding, lenticular bedding, planar lamination, wavy lamination, and rare cross-lamination. Within a given sequence the contact between calcareous siltstone/sandstone and overlying greenish gray calcareous silty claystone and calcareous claystone is usually sharp and planar or wavy, but gradational contacts also occur. Bioturbation (?*Planolites*) extends downward from the darker claystones into the calcareous silty claystone or calcareous claystone intervals. *Chondrites* was observed only rarely.

Figure 11 shows that at both Sites 900 and 1067 that there is a similar downward increasing, then decreasing, proportion of calcareous silty and sandy sediments.

A change in sediment color first appears in Core 173-1067A-3R. Here some of the claystones are pale brown instead of the greenish gray to grayish green characteristic of these lithologies in higher cores. Below Core 173-1067A-8R almost all the claystones are brown, as are a high proportion of the calcareous claystones. The same color change occurs at a similar level at Site 900 (Fig. 11). The presence of a few reduction spots in the cores, in which ovoid greenish gray areas as much as 2 cm across are surrounded by brown color, suggests that immediately after deposition the sediment was brown, but during burial was reduced to give the greenish gray color observed today.

Petrography

Examination of smear slides (Section 4, CD-ROM, back pocket, this volume), thin sections (Sections 5 and 6, CD-ROM, back pocket, this volume), and X-ray diffraction (XRD) data reveal the following

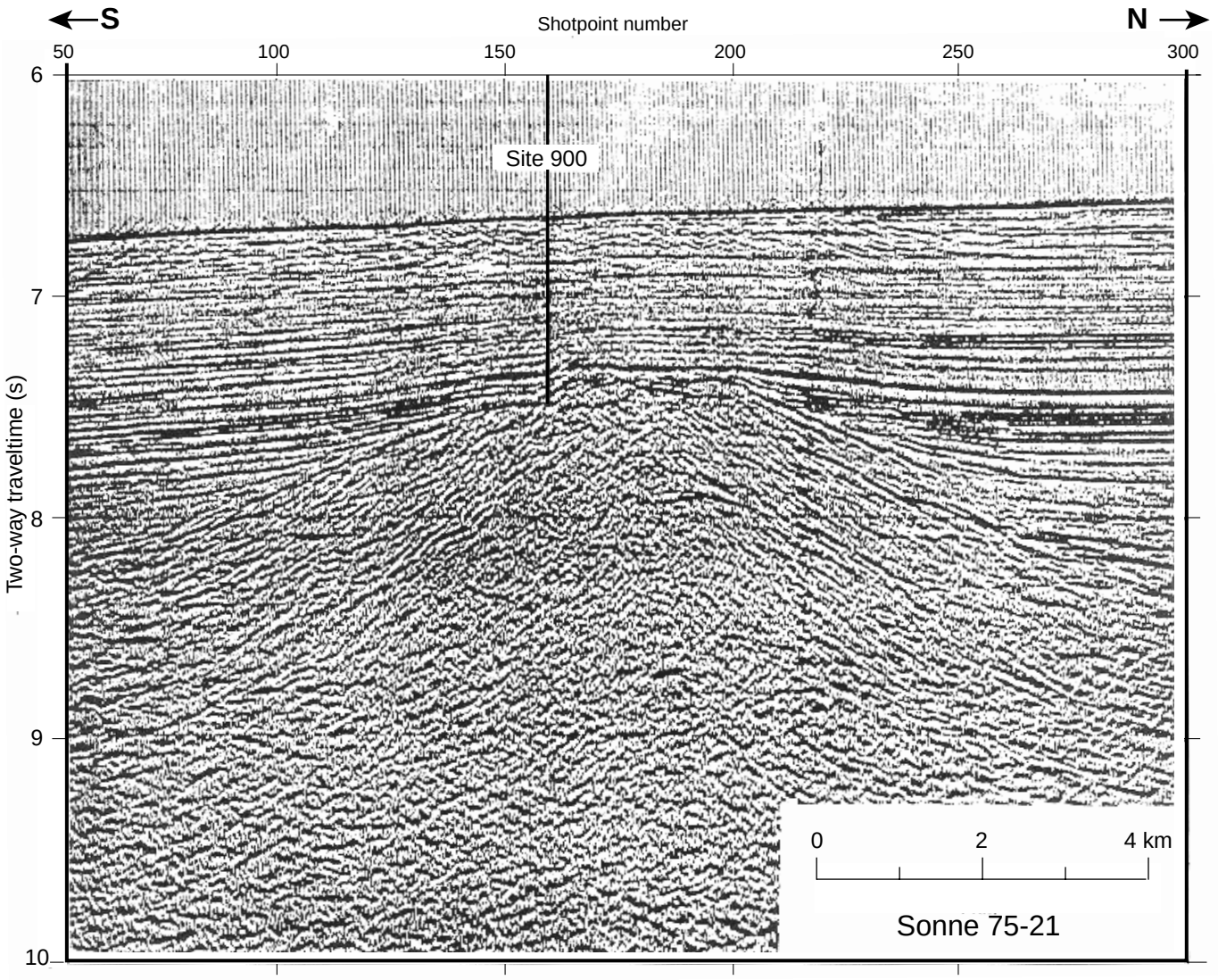

Figure 5. Sonne-75 Line 21 time-migrated section across Site 900 (courtesy of K. Hinz). For location see Figure 2.

key features of the lithologies present in the upward-darkening sequences. The basal calcareous sandy siltstones and sandstones are dominated by angular to extremely angular quartz clasts (Fig. 9), rare to common mica flakes, and rare feldspar. Traces of silt-sized peloids occur. The matrix consists of calcite spar or microspar (Fig. 9). In some cases the clasts are entirely matrix supported, suggesting that the matrix originated by neomorphism of an original micrite (nannofossil?) matrix. Some sparry calcite crystals contain ovoid-shaped areas of inclusions indicating the former presence of allochems, and rare examples of syntaxial overgrowths over echinoderm fragments occur. Some of the calcareous siltstones and sandstones contain laminae in which the matrix is finer grained (microspar or micrite) than that of the dominant lithology (Fig. 9). Calcareous sandstones invariably contain laminae in which complete and fragmented tests of planktonic(?) foraminifers occur (Fig. 9). These fossils also occur in trace amounts in the finer grained calcareous sediments. A few thin beds of foraminiferal chalk were noted (Fig. 9), which occur at the bases of upward-darkening sequences.

One example of a conglomerate occurring at the base of a calcareous sandstone was observed in interval 1067A-13R-1, 126–128 cm (Fig. 10A). Most of the pebbles are light colored, and in thin section can be seen to consist of a variety of shallow-water limestone lithologies (Fig. 10B) similar to those observed in Units II and V at Site 1065. Several dark gray pebbles are also present, but were not seen in thin section; they are probably composed of pelites.

The compositions of the silt-sized clasts in the calcareous claystones are similar to those in the coarser lithologies described in the previous paragraph. The matrix appears to be a mixture of micrite and phyllosilicate clay, including illite. In one thin section, small diameter burrows (probably *Chondrites*) are lined with darker material, and are not filled with sediment. Larger burrows (1.5 mm deep and over 5 mm in length) are filled with an orange-brown material. Under crossed polars this appears to be optically pseudocontinuous (Fig. 12), a property commonly observed in the claystones (see below). The surrounding calcareous claystones do not show such continuity.

Greenish gray and pale brown claystones are dominated by clay minerals (including illite), with only rare or trace levels of quartz silt and carbonate grains. X-ray diffraction analysis indicates that feldspar is also present. The only difference that could be observed in smear slides between the greenish gray and pale brown lithologies was that the latter contain aggregates of clays coated with reddish iron oxide. When observed under crossed polars, some thin sections

Table 1. Site 1067 coring summary.

Core	Date (May 1997)	Time (GMT)	Interval (mbsf)	Length cored (m)	Length recovered (m)	Recovery (%)
Drilled from 0.0 to 648.0 mbsf						
173-1067A-						
1R	04	2300	648.0-657.6	9.6	5.57	58.0
2R	05	0110	657.6-667.3	9.7	3.82	39.4
3R	05	0350	667.3-676.9	9.6	5.29	55.1
4R	05	0655	676.9-686.5	9.6	4.49	46.8
5R	05	1015	686.5-696.1	9.6	4.12	42.9
6R	05	1330	696.1-705.8	9.7	3.18	32.8
7R	05	1800	705.8-715.5	9.7	3.95	40.7
8R	05	2210	715.5-725.2	9.7	5.25	54.1
9R	06	0140	725.2-734.8	9.6	7.18	74.8
10R	06	0520	734.8-739.6	4.8	4.79	99.8
11R	06	0910	739.6-744.5	4.9	4.73	96.5
12R	06	1445	744.5-754.2	9.7	1.86	19.2
13R	06	2045	754.2-763.8	9.6	2.44	25.4
14R	07	2359	763.8-773.4	9.6	0.90	9.4
15R	07	0410	773.4-782.9	9.5	0.53	5.6
16R	07	0715	782.9-792.4	9.5	1.45	15.3
17R	07	1010	792.4-801.9	9.5	0.80	8.4
18R	07	1730	801.9-811.5	9.6	1.81	18.9
19R	07	2325	811.5-821.1	9.6	4.02	41.9
20R	08	0635	821.1-830.8	9.7	1.80	18.6
21R	08	1055	830.8-840.4	9.6	1.02	10.6
22R	08	1540	840.4-850.0	9.6	3.51	36.6
23R	08	2340	850.0-855.6	5.6	5.16	92.1
			Cored totals	207.6	77.67	37.41
			Drilled	648.0		
			Total	855.6		

An expanded version of this table with individual section lengths is on the CD-ROM, back pocket, this volume.

of the claystone are seen to be optically pseudocontinuous, with large areas showing extinction parallel to the bedding. This phenomenon is probably the result of significant compaction resulting in the clay minerals becoming almost perfectly aligned parallel to one another. Examination of thin sections of calcareous claystones revealed no evidence for such intense compaction.

A pebble-sized pinkish gray piece of very fine-grained noncarbonate material encased in moderate brown claystone occurs in interval 173-1067A-11R-3, 79–80 cm; XRD analysis showed this to be composed entirely of apatite.

Depositional Processes

Whereas the bases of the upward-darkening sequences that dominate Subunit IIB are composed of calcareous silts and/or sands, the overlying sediments do not exhibit the clear normally graded signature characteristic of turbidites (Bouma, 1962). The upward change in color reflects a change in composition from carbonate-rich to almost carbonate-free lithologies. The upward decrease in carbonate content can be explained by postulating two alternative origins for the lighter carbonate-rich lithologies at the base of the upward-darkening sequences. (1) They were deposited below the CCD by turbidity flows carrying carbonate and phyllosilicate clay sediment from sources above the CCD. The overlying carbonate-poor claystones originated as hemipelagic deposits; the remains of any calcareous pelagic organisms were dissolved before they reached the seafloor or were buried. Alternatively, (2) the calcareous claystones are pelagic/hemipelagic deposits, with the overlying carbonate-poor claystones being deposited by turbidity flows. The second hypothesis seems unlikely, as it does not explain the presence of the basal siliciclastic sandy laminae in the calcareous claystones, nor the absence of scouring at the base of the dark claystones. Therefore, we follow the Leg 149 Shipboard Party's interpretation that the upward-darkening sequences observed in Subunit IIB at Sites 897–900 are turbidites (Sawyer, Whitmarsh, Klaus, et al., 1994). Thus the upward-darkening sequences exhibit turbidite facies Tc (basal sandy sediment), Td (lighter colored calcareous claystone), and Te plus possible hemipelagite (darker carbonate poor claystone).

In addition to compaction, syndepositional processes may have played a part in producing the above-mentioned different orientation of clay minerals in the claystones and calcareous claystones. Hemipelagic settling would have resulted in clay mineral flakes settling on the seafloor oriented parallel to bedding: this alignment would have been enhanced during compaction. However, the mixture of clay mineral flakes and fine-grained carbonate was probably deposited relatively rapidly from turbidity flows, and so immediately after deposition the clay particles would not have shown a strong bedding parallel orientation. The carbonate component of the sediment would have largely prevented any further significant clay mineral orientation during compaction.

Sedimentary structures within the basal calcareous siltstones and sandy siltstones (scour and fill, lenticular bedding, planar and wavy lamination, and rare cross-lamination) are characteristic features of turbidite facies Tc. However some of the features exhibited by them are not consistent with a turbidite origin. These include the presence of sharp and erosional upper boundaries, isolated lenses and laminae of sandy siltstone in silty claystone, the concentration of foraminifer tests into discrete laminae within the quartz sands, and the lack of normal grading. The Leg 149 Shipboard Scientific Party (Sawyer, Whitmarsh, Klaus, et al., 1994) suggested that all these features point to reworking by contour currents, as described by Stow and Piper (1984); we agree with this conclusion.

Subunit IIB was deposited at the base of the continental rise on the northeastern margin of the southern Iberia Abyssal Plain. The turbidity flows probably originated on the steeper parts of the adjacent continental rise to the north and east. The inference that contour currents reworked turbiditic sediments is supported by reflection geometries observed on seismic sections that are characteristic of seafloor bedforms and associated large-scale sedimentary structures produced by such currents (Wilson et al., 1996).

Seismic reflection profiles in the Leg 149/173 area indicate that sedimentary structures produced by migrating seafloor bedforms related to contour currents are unequivocally present in Pleistocene to middle Eocene sediments. The sedimentological evidence from Sites 900 and 1067 shows that such currents were active at least as early as the late Paleocene. Cold Antarctic bottom waters would have been unlikely to have flowed over the west Iberia margin before the growth of an Antarctic ice sheet during the Oligocene. Therefore, during the Paleocene and Eocene, contour currents flowing along the west Iberia margin must have had another cause.

The 2-cm-thick conglomerate horizon encountered in Paleocene sediments near the base of Subunit IIB contains granules and pebbles of pale shallow-water limestones and dark gray pelite clasts that are similar in composition to clasts recovered in the Upper Jurassic and Miocene sediments drilled at Site 1065. Their presence suggests that basement rocks and Mesozoic shallow-water limestones were probably exposed during the Paleocene in nearby uplifted areas about 15 km to the north of Site 1067.

BIOSTRATIGRAPHY

Calcareous microfossils are common and generally well preserved at the top of the cored sedimentary section. They become less well preserved downward and numerous samples toward the base of the hole are barren of calcareous microfossils. For the most part, the deeper sediments were deposited close to or below the calcite compensation depth (CCD). Biostratigraphically, the section is essentially continuous (taking into account the moderate recovery of about 50% in the upper portion) and ranges in age from middle Eocene to late Paleocene; one isolated sample near the base is Danian.

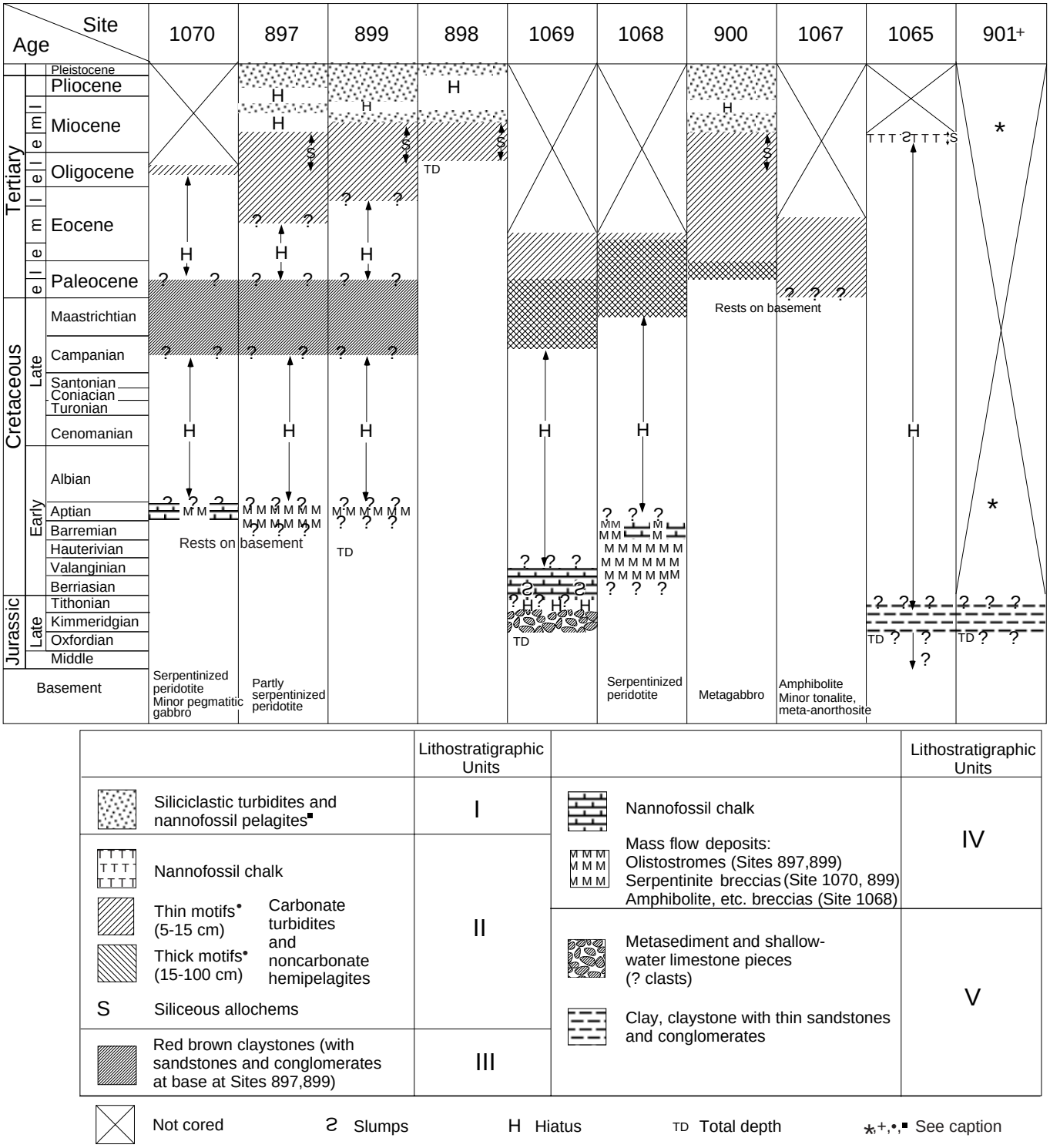

Figure 6. Simplified summaries of stratigraphic successions cored at Leg 149 and Leg 173 sites. Unit III is almost barren of fossils and so its age is very uncertain. + = Unit V as shown in Site 901 was designated by Shipboard Scientific Party (1994d) as Unit II, following the normal ODP practice of numbering units sequentially downhole; * = a washed core recovered Miocene nannofossil ooze and a 5-mm-thick layer of gray clay of Aptian age. Solid square = nannofossil pelagites dominant at Site 900. Solid circles = "Motifs" refers to types of upward-darkening sequences shown in Figure 2 of the "Site 1068" chapter and Figure 8 of the "Site 1069" chapter (both this volume). The cross-hatched symbols on the summary chart indicates that both thin (Motif 2) and thick (Motif 1) sequences are present.

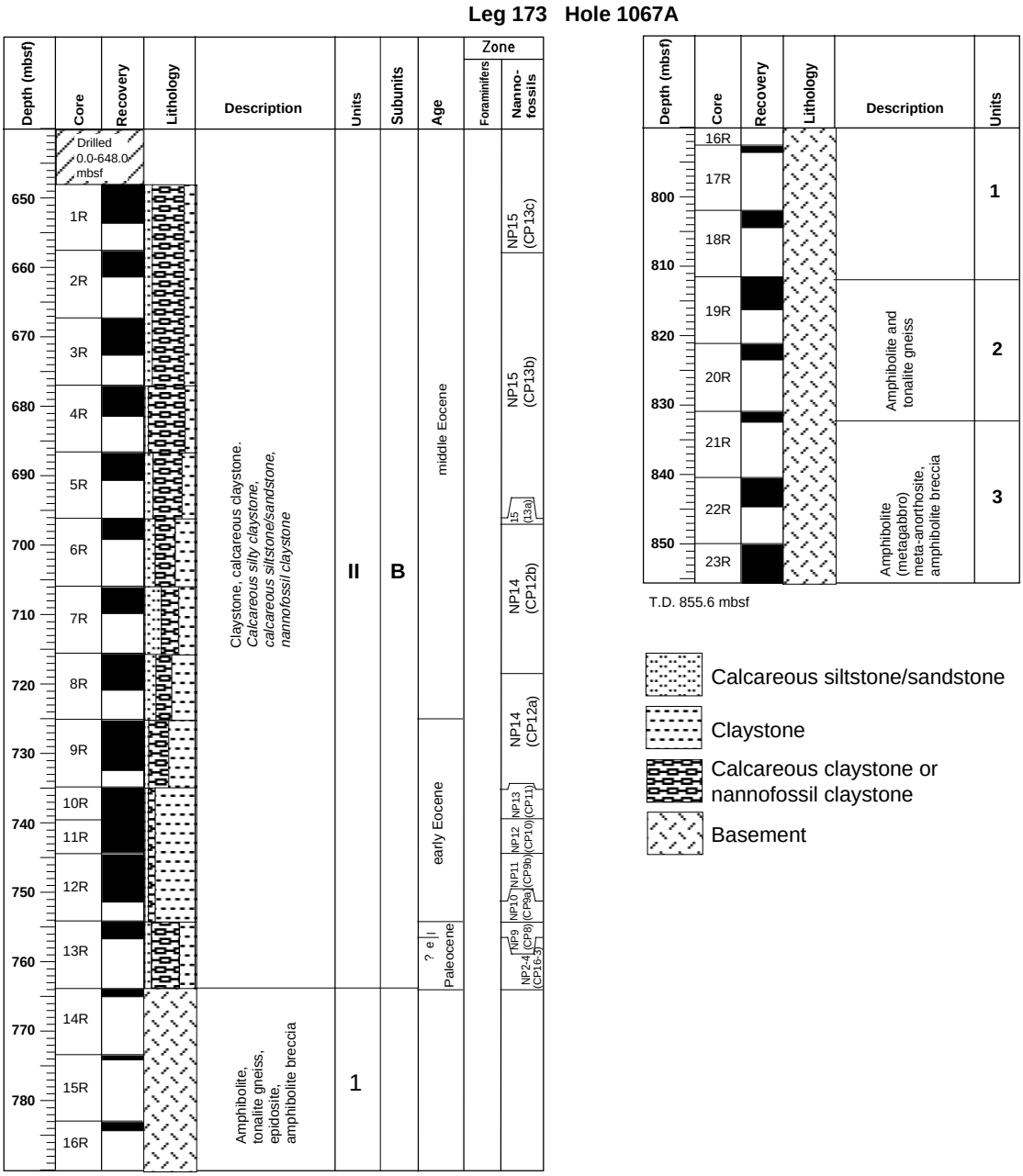

Figure 7. Summary lithostratigraphic column for Hole 1067A. Note that the middle lithologic symbol in the lithology column denotes calcareous claystone. Minor lithologies are listed in italics.

Table 2. Summary of lithostratigraphic Subunit IIB at Site 1067.

Subunit IIB age	Thickness* (m)	Major lithology *Minor lithology*	Abundance (%)	Color	Facies and *environment* (total meters described)	Intervals (mbsf)	Occurrence
	>115.8	Claystone	50	Grayish green, moderate brown	Contourites,		
middle Eocene to					turbidites,	648	1R-1, 0 cm
late Paleocene,		Calcareous claystone	30	Greenish gray	hemipelagites	to	to
(?)early Paleocene**		*Calcareous silty claystone*	<10	Greenish gray	*Base of continental rise/*	763.8	13R-CC, 21 cm
		Calcareous siltstone	<10	Light gray	*edge of abyssal plain*		
		and sandstone			(62.71)		
		Nannofossil claystone	<5	Greenish gray			

Notes: Lithostratigraphic unit as defined at Site 900 (Leg 149); * = drilling commenced within Subunit IIB. ** = (?) early Paleocene age was obtained from a piece of nannofossil chalk at the top of Core 14R.

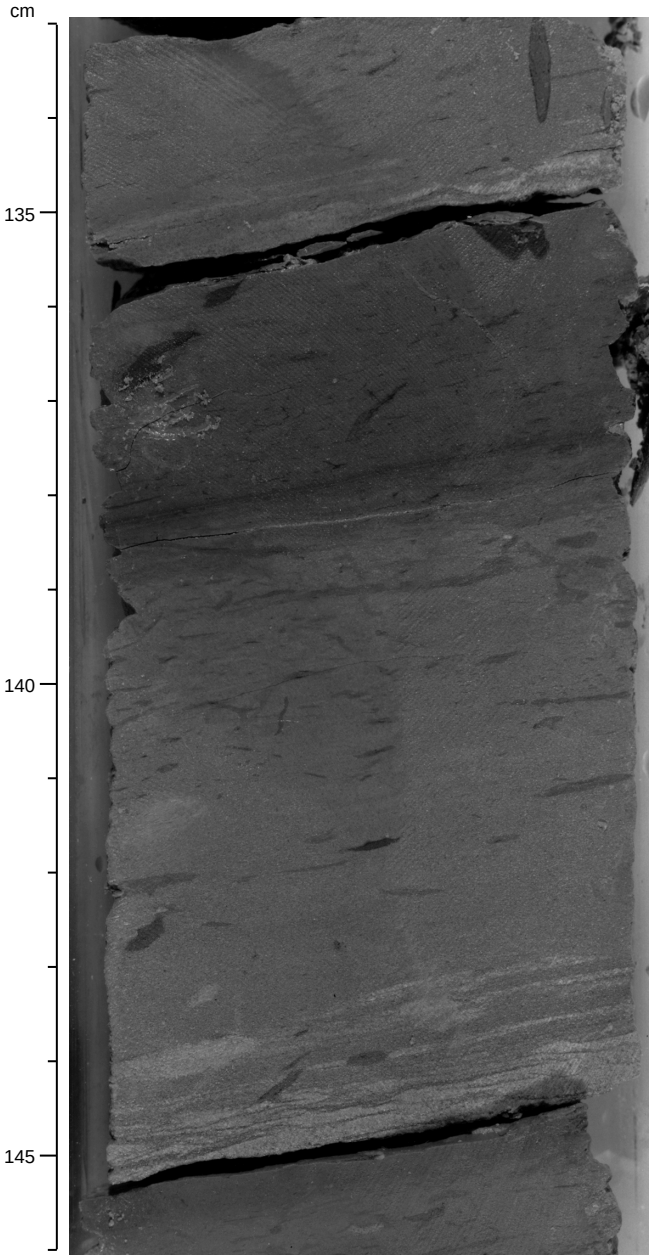

Figure 8. A typical upward-darkening sequence (interval 173-1067A-1R-1, 133–146 cm). The lower part of the sequence (139–145.3 cm) consists of lighter calcareous claystone (or silty claystone) overlain by darker claystone (136–139 cm); burrows penetrate down from the upper lithology. The base of the sequence contains lenticular laminae of sandy siltstone (144.0–145.0 cm).

Calcareous benthic foraminifers are commonly present in samples analyzed throughout the section but are usually very small, being present in the size fraction of <125 µm. Sporadic occurrences of agglutinated foraminifers are recorded.

Planktonic foraminifers recovered in the core-catcher samples vary in abundance and preservation. Their abundance is thought to be facies controlled. In the upper part of the sedimentary sequence, between Samples 173-1067A-1R-CC and 173-1067A-4R-CC, planktonic foraminifers are rare to few with poor to moderately good preservation. Sample 173-1067A-5R-CC yielded more common, moderately diverse, poorly preserved specimens. In Samples 173-1067A-6R-CC through 173-1067A-13R-CC, planktonic foraminifers are recorded as rare with poor preservation. A few horizons of fossiliferous foraminifer chalk have been identified within the cored sequence. The interval between 653.53 mbsf and 756.55 mbsf is assigned a Paleogene age based on planktonic foraminifer biostratigraphy.

Within the sedimentary sequence, all Okada and Bukry (1980) calcareous nannofossil zones are accounted for from Subzone CP13c (Zone NP15 of Martini, 1971) in Core 173-1067A-1R to Subzone CP8 (NP9) in Core 13R. The isolated Danian sample mentioned above was not in place, but consisted of a pebble at the top of basement in Core 14R.

The age-depth plot for this site (Fig. 13; Table 3) indicates high sedimentation rates for the middle Eocene (roughly 45–49 Ma), where there is considerable pelagic carbonate in a sequence deposited well above the CCD. Very low rates are indicated for the lower Eocene (50–54 Ma), where carbonate dissolution was intense because of deposition close to and below the CCD and because the site at that time was located on a topographic high, whereby turbidites bypassed the essentially pelagic cap being deposited on the exposed summit. A break in the curve between 46 and 48 Ma may represent a hiatus. Sedimentation rates were greater again in the short upper Paleocene section (55.0–56.2 Ma) where nannofossils are abundant and quite well preserved.

Calcareous Nannofossils

Calcareous nannofossils were generally abundant, diverse, and well preserved in the upper (middle Eocene) portion of the cored interval. All of these qualities diminish downhole. However, the lower Eocene sediments were deposited when the site lay close to or below the CCD; hence, the barren intervals beginning in Core 173-1067A-9R (Table 4). In some cores, nannofossils are best preserved in the greenish, sandy intervals associated with turbidites; these alternate with brown hemipelagites (see "Lithostratigraphy" section, this chapter). Preservation and abundance improve in the first section of Core 173-1067A-13R (upper Paleocene) and is good in the Danian, which is represented by a single pebble recovered at the top of basement from Core 173-1067A-14R. Virtually all assemblages contained trace amounts of reworked Upper Cretaceous nannoliths; these are plotted with lower-case letters for abundance on the right side of Table 4.

All Martini (1971) and Okada and Bukry (1980) nannofossil zones and subzones are represented in the middle Eocene–upper Paleocene section as indicated in the distribution chart (Table 4). A single, but perfectly preserved specimen of *Chiasmolithus gigas* in Sample 173-1067A-1R-3, 36–37 cm, marks the top of Subzone CP13b. For purposes of this zonation, single occurrences of *Reticulofenestra umbilica* in Samples 173-1067A-1R-CC and 3R-CC are ignored as these do not represent a consistent first occurrence of the species (which is often used in practice to mark the base of Zone NP16/CP14). Rare to few *Nannotetrina pappii* in Cores 173-1067A-2R and 3R are consistent with the subzonal assignment. Dissolution-susceptible *Braarudosphaera* and *Micrantholithus* are common in the first three cores, indicating deposition well above the CCD.

Rare *Nannotetrina fulgens* denote the base of Zone NP15 (CP13a). These specimens are strongly overgrown and often broken at the tips. The interval represented by Subzone CP13a (denoted by the presence of *Nannotetrina fulgens* in the absence of *C. gigas*) is quite short, limited to only one sample as at nearby Site 900 (see Liu, 1996, table 7). This abbreviated interval might indicate a local disconformity.

Rare specimens of *Rhabdosphaera inflata* mark the base of Subzone CP12b (NP14) in Sample 173-1067A-8R-2, 36–37 cm. These are usually broken, but fragments can often be recognized by their rugose surface texture, which gives the outline of the spine a serrated appearance when viewed in polarized light. *Discoaster sublodoensis*,

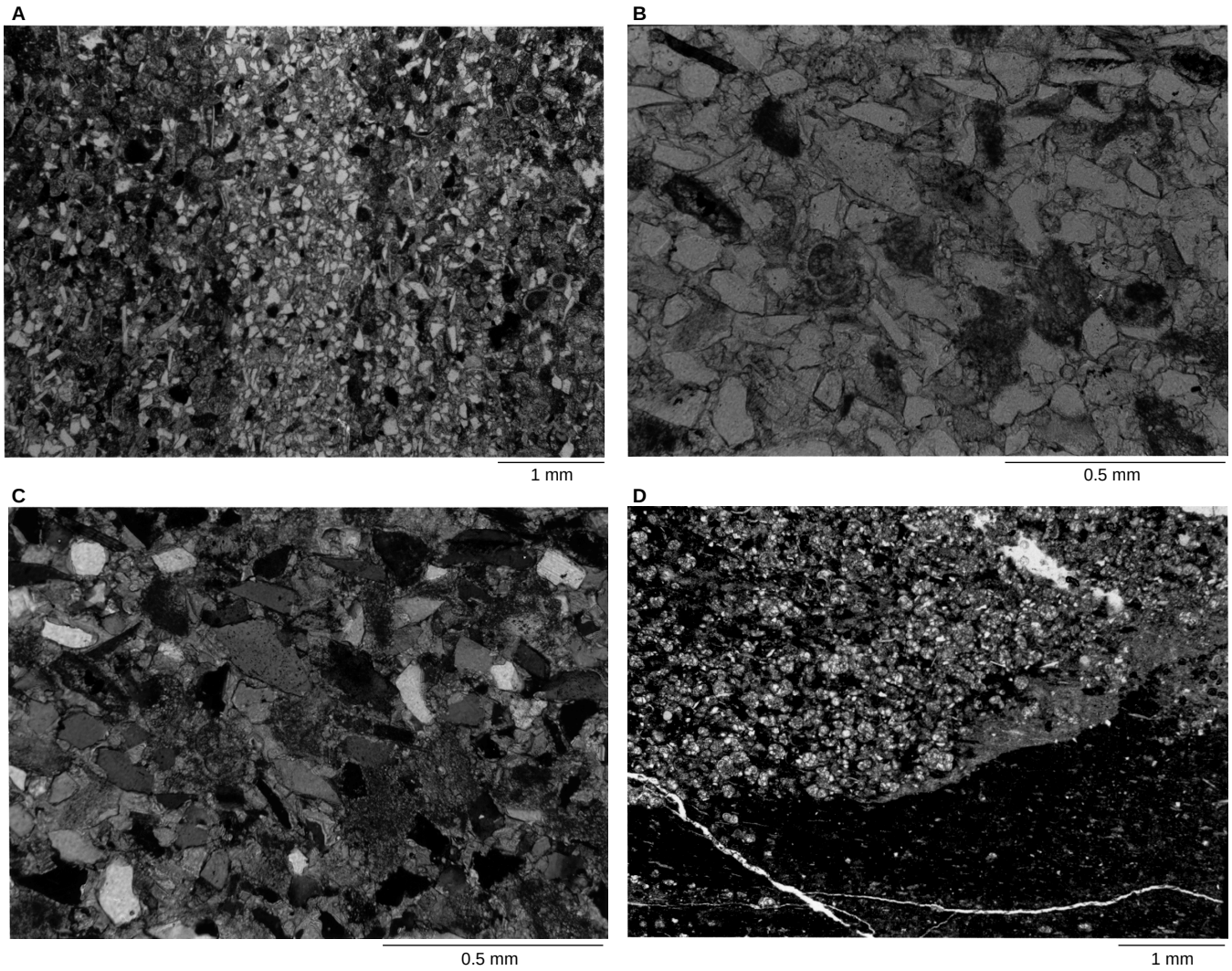

Figure 9. Photomicrographs of calcareous lithologies occurring in Subunit IIB, Hole 1067A. **A.** Laminated calcareous sandstone, Sample 173-1067A-5R-3, 88–91 cm. The lighter lamina is composed of calcite cemented angular quartz clasts. The matrix in the darker areas is composed of micrite and microspar (?neomorphosed nannofossil chalk) with scattered foraminifers. Muscovite flakes are more abundant in the darker areas. **B, C.** Plane polarized (B) and crossed polar views (C) of a calcareous sandstone at Sample 173-1067A-6R-2, 17–18 cm. Angular quartz clasts and peloids are cemented by sparry calcite. The dark flake at the upper left is a biotite clast. Two fragments of foraminifers occur slightly left of center. **D.** Contact between foraminiferal chalk (top) filling a burrow and dark claystone (bottom) at Sample 173-1067A-8R-1, 26–29 cm. The fractures resulted from thin-section preparation.

the major marker for Zone NP14 (CP12), is rare to common within the interval. Although most specimens have been distorted by diagenesis, this taxon has tentatively been traced down to Sample 173-1067A-9R-CC. At this point the brown hemipelagites are barren (or nearly so) of nannofossils (e.g., Sample 173-1067A-9R-2, 121–123 cm), which are best sought in the greenish lithologies. Taxon diversity also begins to decrease noticeably at this point in the section where the more dissolution-susceptible species are missing from the assemblages (see Table 4).

Discoaster lodoensis, the nominate taxon for the "gap" Zone NP13 (CP11), is common to abundant within the more carbonate-rich intervals, although it is commonly overgrown with secondary calcite. It co-occurs with *Tribrachiatus orthostylus* in Sample 173-1067A-11R-3, 40–41 cm, to mark the upper limit of NP12 (CP10). Although abundant, most specimens of *T. orthostylus* are heavily encased in secondary calcite and appear as small triangular objects. These are even more concentrated in the light brown sediment, Sample 173-1067A-12R-1, 10–12 cm, which resembles a veritable *T. orthostylus* ooze. This is a residual assemblage that has undergone severe dissolution during deposition close to the CCD. Preservation improves slightly in Sample 173-1067A-12R-1, 46–47 cm, to the point that positive identification of *T. orthostylus* can be made. *Discoaster lodoensis* is absent throughout Section 173-1067A-12R-1 which is, therefore, assigned to NP11 (CP9b). Sample 173-1067A-12R-2, 47–48 cm, is barren of nannofossils but Sample 173-1067A-12R-CC, 25–27 cm, contains a somewhat diverse, moderately preserved assemblage containing *Tribrachiatus contortus*, the upper marker for Zone NP 10 (CP9a). Despite a diligent search, no other sample in the core catcher or in the core section above this sample contained this lowermost Eocene zonal assemblage.

Preservation improved dramatically in the greenish calcareous claystones in Section 173-1067A-13R-1, which contains a highly diverse upper Paleocene assemblage from Zone NP9 (CP8). Deposition well above the CCD is indicated not only by the reappearance of the holococcolith *Zygrhablithus bijugatus*, but by the excellent preservation and high diversity of the assemblage. Notable is the large number of fasciculith species, most of which were first described by Perch-Nielsen (1971) from DSDP Site 119 in the nearby Bay of Biscay, just

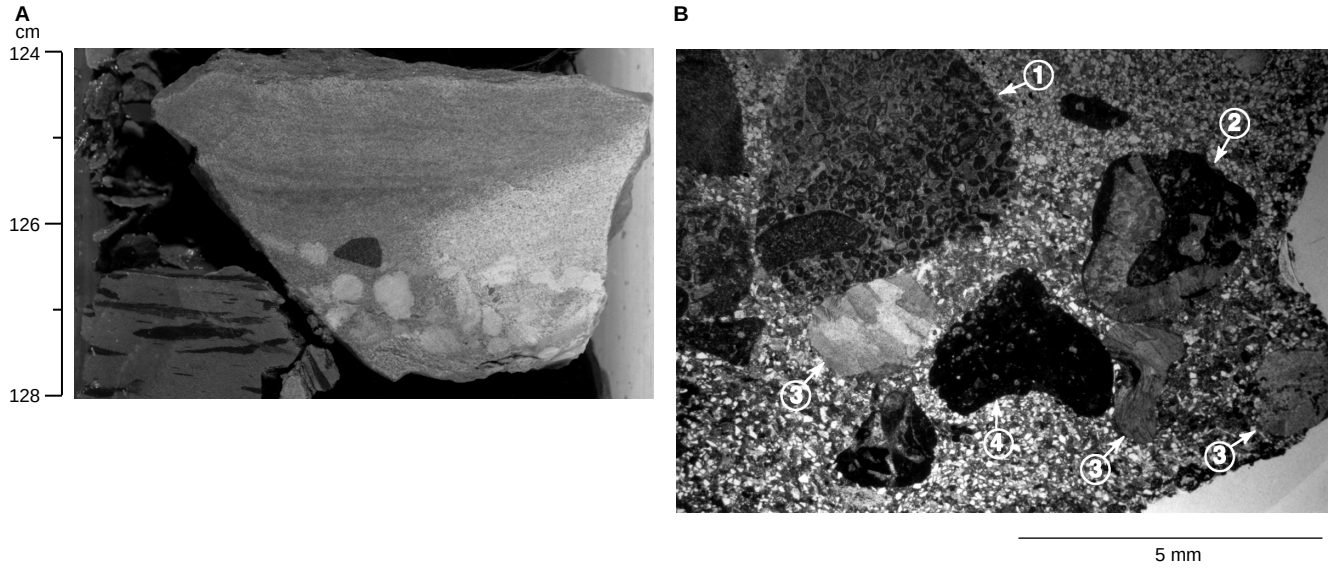

Figure 10. Conglomerate at 1067A-13R-1, 124–128 cm. **A.** Close-up core photo showing matrix-supported pebbles of pale limestone and one dark gray (?)pelite clast. **B.** Photomicrograph taken in plane polarized light showing shallow-water limestone clasts encased in calcareous sandstone matrix. Numbers indicate the following lithoclast types: 1 = Intraclast/peloid grainstone with calcite spar cement: the large allochem at the bottom left is possibly a large benthic foraminifer; 2 = lithoclast of bivalve fragment and aggregate of micritized skeletal debris in micritic/microspar matrix; 3 = bivalve fragments; 4 = fragment of encrusting cyanobacterial micrite.

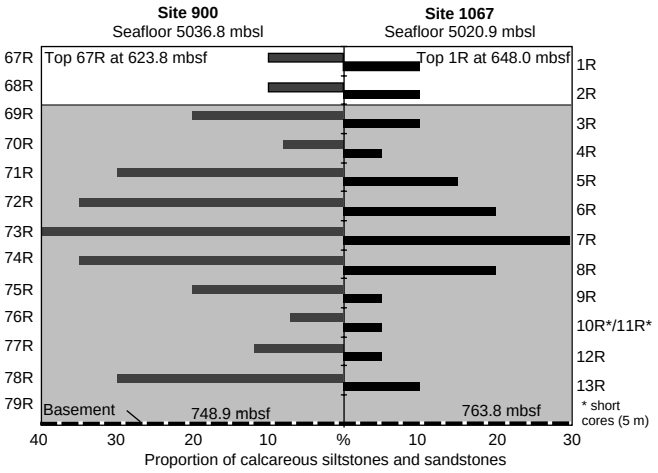

Figure 11. Comparison of visual estimates of the proportions of calcareous siltstones and sandstones present in sediments from lithostratigraphic Subunit IIB at Sites 900 and 1067. The occurrence of brown claystones is also shown in both holes as shaded area. Note that preliminary results show sedimentation rates at the two sites were different. This is because the boundary between nannofossil zones NP15 and NP14 occurs at the top of 149-900A-70R, and between 173-1067A-5R and 6R; the NP14 and NP13 boundary occurs between 149-900A-74R and 75R, and between 173-1067A-9R and 10R; the NP12 and NP11 boundary occurs between 149-900A-76R and 77R, and between 173-1067A-11R and 12R.

northwest of the Iberian peninsula. The presence of *Heliolithus cantabriae* in this assemblage along with *Discoaster multiradiatus* suggests that it represents the lower part of Zone NP9 (CP8; Perch-Nielsen, 1985, fig. 37). Immediately below this richly fossiliferous interval, the brown clays of Section 173-1067A-13R-2 and Sample 173-1067A-13R-CC were barren.

Sample 173-1067A-14R-1, 0–3 cm, is a light buff to pink calcareous claystone that was retrieved at the top of the first basement core. The well-preserved assemblage is dominated by *Coccolithus pelagicus* and large (>8 µm) *Cruciplacolithus tenuis* with well-developed "feet." *Cruciplacolithus primus* is rare. The large size of the *C. tenuis* in the absence of *Fasciculithus* spp. indicates upper Zone NP2 or higher (NP3–NP4). However, the lower NP4 index taxon, *Ellipsolithus macellus*, is absent throughout the Paleogene section at this site, and no *Chiasmolithus danicus*, the NP3 lower zonal marker, has been positively identified. Thus, a more refined age assignment cannot be made without further detailed examination.

Planktonic Foraminifers

Planktonic foraminifers recorded from Hole 1067A in the size fraction 125–500 µm are generally poorly to moderately well preserved, occur rarely, and are represented by low-diversity assemblages (Table 5). Although the in situ species found in these samples are consistent with the Paleocene through middle Eocene ages determined using calcareous nannofossils, no diagnostic age index forms have been recovered that indicate zonal boundaries. Samples 173-1067A-1R-CC through 173-1067A-8R-CC, all dated as middle Eocene, yielded species that include *Globigerina lineaperta, Acarinina bullbrooki, Truncorotaloides rohri*, and *Pseudohastigerina wilcoxensis.* Lower Eocene sediments in Samples 173-1067A-10R-CC through 173-1067A-12R-CC contain specimens that include *Morozovella aragonensis, Acarinina primitiva*, and *Pseudohastigerina wilcoxensis.* Samples 173-1067A-7R-CC and 173-1067A-9R-CC are barren of planktonic foraminifers, whereas Sample 173-1067A-13R-CC contains only very rare, and very poorly preserved, indeterminate planktonic foraminifers.

Benthic Foraminifers

Calcareous benthic foraminifers are present as rare to few specimens throughout the section and are often very poorly preserved or silicified in the size fraction above 125 µm. Agglutinated benthic foraminifers rarely occur in samples analyzed in this sequence. Species recovered are characteristic of relatively deep-water habitats and include such forms as *Bathysiphon* spp., *Glomospira* spp., and *Saccam-*

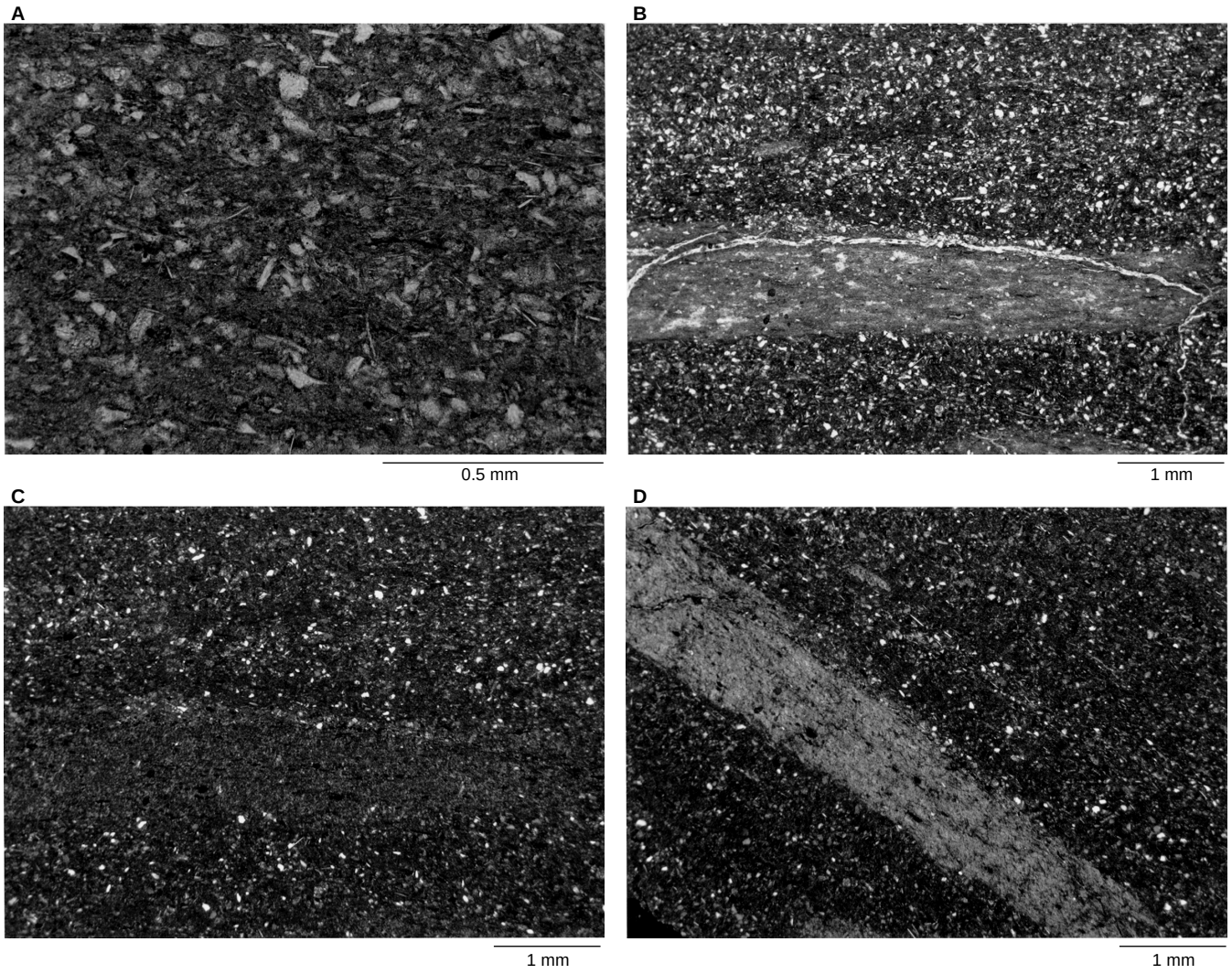

Figure 12. Photomicrographs of thin sections of silty claystone, Sample 1067A-1R-1, 142–145 cm. **A.** Plane polarized light. Clasts of angular quartz and muscovite floating in clay matrix. **B.** Plane polarized light; fracture resulted from thin-section preparation. **C, D.** Burrow in silty clay is filled with lighter colored (light brown) claystone, in which individual clay grains are optically aligned, so that the entire burrow fill goes into extinction parallel to bedding almost simultaneously (C = crossed polars; D = brightest interference colors at 45°).

mina spp. The deep-water agglutinated forms such as *Spiroplectammina spectabilis* and *Rzehakina epigona*, commonly present in Atlantic Paleogene deeper water sediments, are notably absent in these samples.

Other Components

Radiolarians are abundant in Sample 173-1067A-1R-CC. Rare ostracodes are present in Sample 173-1067A-6R-CC, and rare ichthyoliths occur in Sample 173-1067A-4R-CC.

Common to abundant planktonic and benthic foraminifers occur in the size fraction 63–125 µm throughout the uppermost (Samples 173-1067-2R-CC to 173-1067-5R-CC) and lowermost (Samples 173-1067-10R-CC to 173-1067-13R-CC) parts of the cored section, although no detailed analyses of these faunas were undertaken during Leg 173. These assemblages are considered to be size sorted and reworked. Because of the high diversity of these fossil assemblages, including a range of morphotypes from the flat, elongate *Bolivina* spp. to the coiled, subspherical shape of *Lenticulina* spp., plus the lack of abrasion to the tests, it is thought that the assemblages have not traveled a great distance before redeposition occurred. If the paucity of calcareous benthic and planktonic foraminifers in the larger size fractions (i.e., between 125–500 µm) is attributable to the proximity of the CCD at, or shortly after, the time of redeposition, then it is possible that the forms in the size fraction 63–125 µm were protected from dissolution by rapid burial in fine-grained, impermeable sediments. These assemblages are absent from the 63–125 µm fractions examined in the interval 173-1067A-6R-CC through 173-1067A-9R-CC, and it is possible either that deposition of this sequence was at a slower rate (thereby allowing dissolution of all calcareous material) or that the initial sedimentation occurred in an environment further downslope and below the CCD.

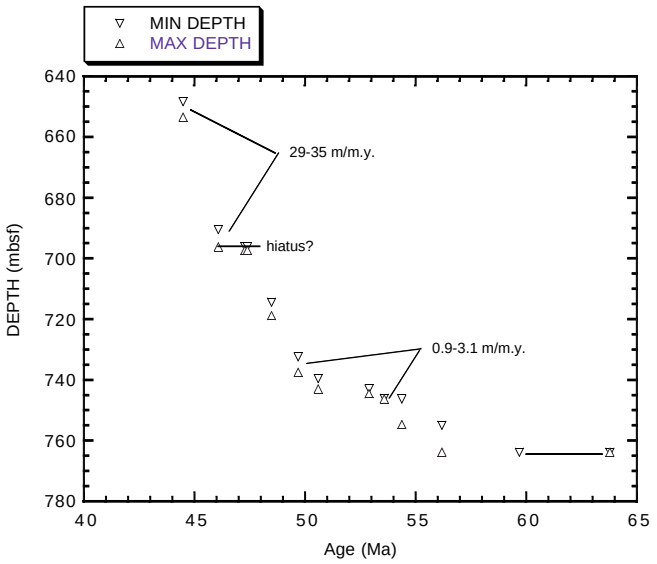

Figure 13. Age-depth plot for Site 1067 (see Table 3 for datums used).

Table 3. Calcareous nannofossil datums used to construct the age-depth plot in Figure 13.

Biozones		Biostratigraphic datums	Age (Ma)	Core, section, interval (cm)	Min. depth (mbsf)	Max. depth (mbsf)
CP13c	t	*C. gigas*	44.5	1R-CC, 21-23	648.34	653.5
CP13b	b	*C. gigas*	46.1	5R-CC, 14-16	690.5	696.2
CP13a	b	*N. fulgens*	47.3	6R-1, 5-6	696.2	697.3
CP12b	t	*R. inflata*	47.4	6R-1, 121-123	696.2	697.3
CP12b	b	*R. inflata*	48.5	8R-2, 36-38	714.4	718.8
CP12a	b	*D. sublodoensis*	49.7	9R-CC, 21-22	732.4	737.5
	t	*T. orthostylus*	50.6	11R-3, 40-41	739.6	743
CP10	b	*D. lodoensis*	52.9	11R-3, 40-41	743	744.6
CP9b	t	*T. contortus*	53.6	12R-CC, 25-27	746.1	746.3
	b	*T. contortus*	54.4	12R-CC, 25-27	746.3	754.8
CP8a	b	*D. multiradiatus*	56.2	13R-1, 80-81	755	763.8
CP4	b	*H. kleinpellii*	59.7	14R-1, top (Piece 1)	763.8	
CP4	b	*C. danicus*	63.8	14R-1, top (Piece 1)	763.8	763.8

Note: b = bottom; t = top.

Kuhnt and Collins (1996) found similar, very fine-grained, rich, and diverse fossiliferous sediments in this area from nearby Hole 900A and interpreted this facies as redeposited sediment.

Mineral grains found in the washed residues suggest transportation from a nearby source (e.g., quartz grains are generally angular and glassy). Heavy mineral grains such as hornblende and feldspars are commonly present in washed residues from Samples 173-1067A-12R-CC and 173-1067A-13R-CC and are believed to be derived from the underlying basement. Abundant muscovite present throughout most of the section was not derived from the underlying basement rocks at this site and possibly originated from nearby, but unidentified, greenschist facies rocks.

PALEOMAGNETISM

Magnetic measurements were made on the archive halves of cores from Hole 1067A using the pass-through cryogenic magnetometer as described in the "Paleomagnetism" section, "Explanatory Notes" chapter (this volume). Generally, most sections were progressively demagnetized using peak alternating fields (AF) of 10, 15, 20, 25, 30, 35, and 45 mT; some sections were AF demagnetized as high as 70 mT. Thirty additional discrete samples, taken from the working half of the core, were progressively AF and thermally demagnetized to determine directional stability and to check the reliability of the measurements from the archive half. The volume magnetic susceptibility was measured at 5-cm intervals on most of the cores from Hole 1067A.

Remanence and Susceptibility of the Sedimentary Unit

Approximately 116 m of claystone was cored at Hole 1067A before crystalline bedrock was encountered. The sediments recovered from this interval (~57 m; Cores 173-1067A-1R through 13R; 648–763.8 mbsf) display two different lithologies. The NRM intensities and magnetic susceptibilities are similar to sediments of the same age from Leg 149, Site 900, 800 m to the west. Upon AF demagnetization to 30 mT, a significant decrease in intensity was observed (Fig. 14). The colors of the sediments from the upper 75 m of this cored interval, composed predominantly of greenish gray to light gray claystone and silty claystone, are noticeably different from those from the lower 40 m, which are predominantly brownish red to red claystone and silty claystone (see "Lithostratigraphy" section, this chapter). Correspondingly, the upper sediments have lower NRM intensities (~10^{-4} A/m) and magnetic susceptibilities (~5–25 × 10^{-5} SI units) than the lower sediments (~10^{-3} A/m and ~15 to >40 × 10^{-5} SI units, respectively; Figs. 14, 15). Exceptionally, the brown sediments (Core 173-1067A-12R, 744.5–754.2 mbsf; see bottom part of Fig. 14) at the base of lithostratigraphic Subunit IIB, are not weakly magnetized and also display higher values of magnetic susceptibility (Fig. 15). Interestingly, a similar phenomenon was observed at Leg 149, Site 900. Core 149-900A-77R, also at the base of Subunit IIB (720.0 mbsf), has the same age (early Eocene), rock type and color, and the same characteristic peaks in NRM intensity and volume susceptibility (see Shipboard Scientific Party, 1994a). This characteristic brown bed and the associated peaks in NRM intensity and volume susceptibility may serve as one of the stratigraphic markers for Leg 173 drill sites. At sea, we were unable to relate the significance of this observation to the sediment mineralogy or regional paleoceanographic conditions.

Magnetostratigraphy of the Sediments

Pass-through measurements of the archive halves of the cores yielded dominantly positive inclinations (normal polarity). The only evidence for a possible reversed chron or subchron occurs at the tops of Cores 173-1067A-10R and 11R (734.8–744.5 mbsf; Fig. 16). Further measurements and progressive demagnetization results from corresponding discrete samples failed to substantiate these polarity changes. Figure 17 exhibits typical demagnetization behavior of these sediments during AF demagnetization. Although AF demagnetization of 15 to 20 mT generally removes the steep component of drilling-induced magnetization (inclinations greater than 70°), it is not clear whether a primary depositional remanent magnetization has been isolated in any of these weakly magnetized samples. Complex behavior was also observed during thermal demagnetization (Fig. 18). The erratic changes in direction and intensity after thermal demagnetization at 200°C suggest the presence of multiple overprints that may be related to phases of reduction of magnetite and generation of iron sulfide.

Table 4. Distribution of calcareous nannofossils, Hole 1067A.

Age	Martini Zone (Martini,1971)	Okada & Bukry Zone (Okada and Bukry, 1980)	Core, section, interval (cm)	Depth (mbsf)	Abundance	Preservation	*Birkelundia staurion*	*Braarudosphaera bigelowii*	*Campylosphaera dela*	*Chiasmolithus bidens*	*Chiasmolithus californicus*	*Chiasmolithus consuetus*	*Chiasmolithus expansus*	*Chiasmolithus gigas*	*Chiasmolithus grandis*	*Chiasmolithus solitus*	*Chiasmolithus titus*	*Coccolithus eopelagicus*	*Coccolithus formosus*	*Coccolithus pelagicus*	*Coccolithus subpertusus*	*Coronocyclus prionion*	*Coronocyclus serratus*	*Cruciplacolithus tenuis*	*Cyclicargolithus* cf *floridanus*	*Cyclicargolithus floridanus*	*Discoaster barbadiensis*	*Discoaster bifax/praebifax*	*Discoaster binodosus*	*Discoaster* cf *diastypus*	*Discoaster* cf *kuepperi*	*Discoaster diastypus*	*Discoaster distinctus*	*Discoaster gemmifer*	*Discoaster helianthus*	*Discoaster kuepperi*	*Discoaster lodoensis*	*Discoaster martinii*	*Discoaster mohleri*	*Discoaster multiradiatus*	*Discoaster nonaradiatus*	*Discoaster robustus*	*Discoaster saipanensis*	*Discoaster* spp. (overgrown)	*Discoaster sublodoensis*
			173-167A-																																								
middle Eocene	NP15	CP13c	1R-1, 34-36	648.34	A	G		C	R			F	F	C	C	C	F	F	C	C					F	C					F									F		
middle Eocene	NP15	CP13b	1R-CC, 21-23	653.53	A	G		C					F		C	C	F	F	C	C		F				F	C					F									F		
middle Eocene	NP15		2R-CC, 13-16	661.39	A	G	F	F	F				R	F	C	F	R	R	C	C		R				F	C										r	R					
middle Eocene	NP15		3R-CC, 23-25	672.57	A	G	F	F	R				R	F	F	F	F	R	A	C		C					C		R					R			R		r				
middle Eocene	NP15		4R-CC, 18-20	681.37	A	M	R	P	P				R	R	F	F	F	F	C	C		P				P	C							P									
middle Eocene	NP15		5R-2, 57-58	688.57	T	P														F																							
middle Eocene	NP15		5R-CC, 14-16	690.52	A	G	R	C	F				R	R	R	F	F	F	C	C		F					C	F													F		
middle Eocene	NP15	CP13a	6R-1, 5-6	696.15	A	G		R							R	F	R		C	C					F		C													F		
middle Eocene	NP14	CP12b	6R-1, 121-123	697.31	A	G	R		R				R		F	R		C	C	A							A	R	R							R			R				R
mid–early Eocene	NP14	CP12a	8R-CC, 23-25	720.73	C	VG	F		F				R		F	C	R	F	A	A		C				F	A							R				R				R
mid–early Eocene			9R-2, 118-119	727.88	B																																						
early Eocene	NP13	CP11	10R-2, 119-120	737.49	C	G						F			F			F	A							C		F		C								R				
early Eocene	NP12	CP10	11R-3, 40-41	743	C	M						F			R			C	A		R	P				F		R	F							F						
early Eocene	NP11	CP9b	12R-1, 10-11	744.6	F	P				F									R							C										A						
early Eocene			12R-2, 47-48	745.97	B																																						
early Eocene	NP10	CP9a	12R-CC, 25-27	746.34	F	P				R		F							C							F				C								C				
early Eocene			13R-1, 7-8	754.27	B																																						
late Paleocene	NP 9	CP8	13R-1, 64-65	754.84	A	VG				C	F	C					F		A	C		F		R										R			F	F				
late Paleocene			13R-2, 50-51	756.2	B																																						
late Paleocene			13R-CC, 16-17	756.55	B																																						
early Paleocene	NP2-4	CP1b-3	14R-1, 0-3	763.8	C	G		C											A	C				C																		

Note: Abundances of reworked taxa are plotted in lower-case letters; reworked Cretaceous forms are on the right hand side of the chart (last 10 columns).

Table 5. Distribution of planktonic foraminifers, Hole 1067A.

Age	Zone	Core, section	Depth (mbsf)	Abundance	Preservation	*Truncorotaloides rohri*	*Acarinina bullbrooki*	*Acarinina pentacamerata*	*Globigerina lineaperta*	*Globigerina eocaena*	*Globigerina* spp.	*Morozovella aragonensis*	*Acarinina primitiva*	*Pseudohastigerina wilcoxensis*	*Acarinina broedermanni*	*Acarinina soldadoensis*	*Globigerina cryptomphala*	*Morozovella quetra*	*Globigerinatheka senni*	*Turborotalia cerroazulensis possagnoensis*	Indeterminate spp.
		173-1067A-																			
middle Eocene	P11	1R-CC	653.53	R	P		R	R	R	R							R	R			
middle Eocene	P11	2R-CC	661.39	F	P	R	R	R	R		R		R								
middle Eocene	P11	3R-CC	672.57	F	P	R	R	R						R					R	R	
middle Eocene	P11	4R-CC	681.37	F	P	R			R		R			R					R		
middle Eocene	P10	5R-CC	690.52	F	P	R	R	R	R	R	R			R	R	R					
middle Eocene	P10	6R-CC	699.26	R	P							R			R	R					R
middle Eocene	P10	7R-CC	709.69	B																	
middle Eocene	P10	8R-CC	720.73	R	P				R	R		R	R	R							
early Eocene	P9	9R-CC	732.37	B																	
early Eocene	P8	10R-CC	739.57	R	P					R		R	R								
early Eocene	P7	11R-CC	744.31	F	P					R	R			R							
early Eocene	P6	12R-CC	746.34	F	P					R	R					R					
Paleocene	?	13R-CC	756.55	P	P																R

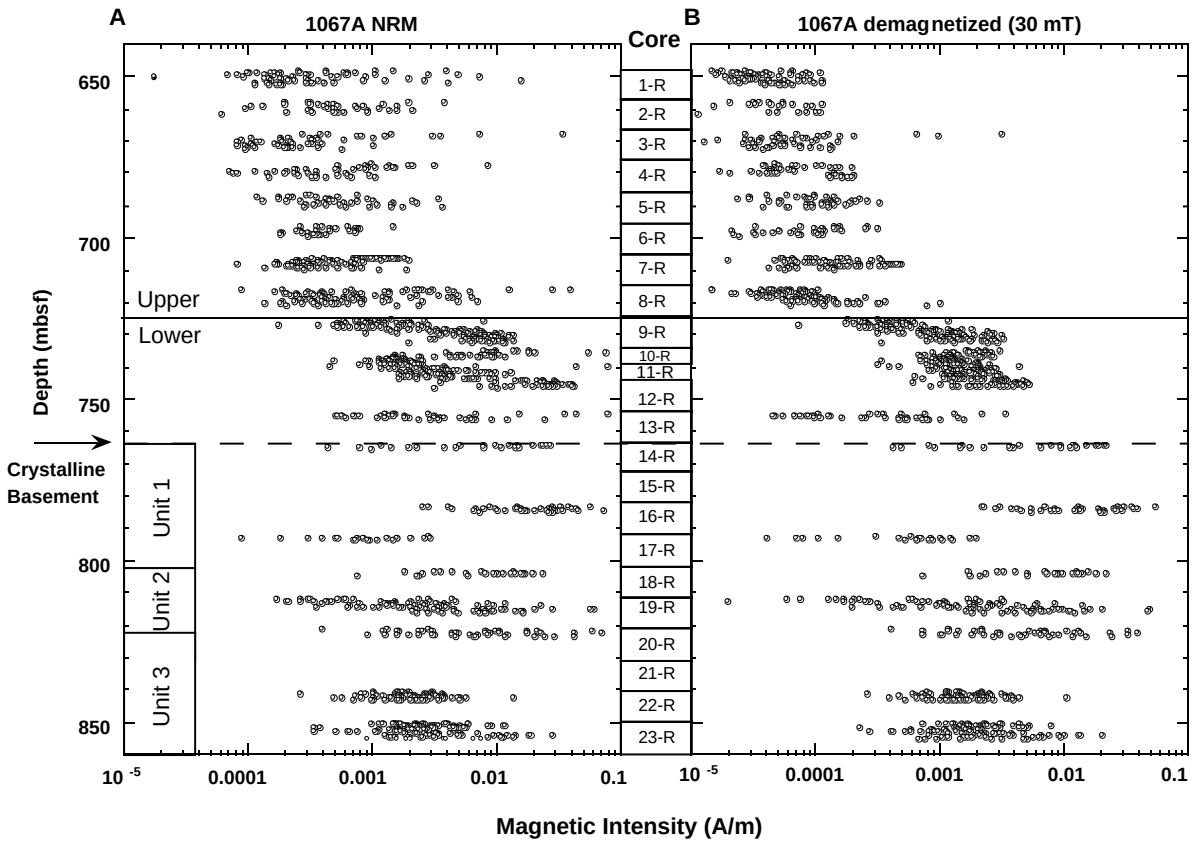

Figure 14. Plot of remanent intensity (**A**) before and (**B**) after 30-mT AF demagnetization as a function of sub-bottom depth for Hole 1067A. Upon demagnetization to 30 mT, a significant decrease in intensity was observed, suggesting that drilling-induced magnetization is present. Horizontal axis has a log scale. The boundary at 725 mbsf denotes a change in core color (see text).

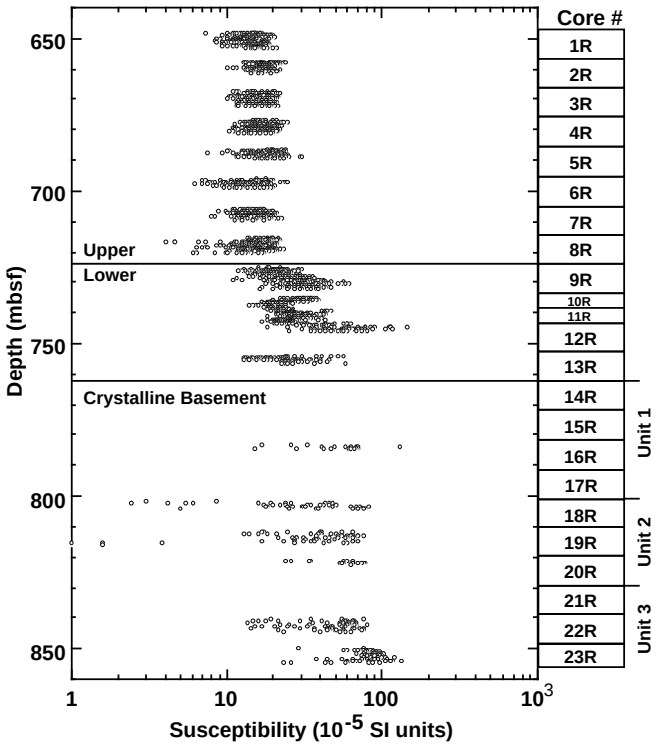

Figure 15. Plot of magnetic susceptibility as a function of sub-bottom depth from Hole 1067A. Horizontal axis has a log scale. The boundary at 725 mbsf denotes a change in core color (see text).

Biostratigraphic evidence indicates a Paleocene to middle Eocene age (see "Biostratigraphy" section, this chapter) for the recovered sediments. During this time interval there were several magnetic polarity reversals (see the revised time scale of Berggren et al., 1995). As discussed above, however, magnetic intensities were weak and no magnetic polarity reversals were observed in the sediment. AF and thermal demagnetization experiments indicate that the sediments have been magnetically overprinted one or more times. Thus, it was not possible to construct a reliable magnetostratigraphy.

Magnetic Characterizations of the Basement Rocks

Below Core 173-1067A-13R (763.8 mbsf), the recovered cores are medium-grained metamorphosed mafic rocks and can be divided into three units (see "Igneous and Metamorphic Petrology" section, this chapter). The magnetic intensities of Units 1 and 2 have average values consistently above 5×10^{-2} A/m and the Königsberger ratio Q (defined as the ratio of the NRM intensity to the induced magnetization in the local Earth's field, see "Paleomagnetism" section, "Explanatory Notes" chapter, this volume) is greater than 0.5, whereas the average intensity and Q in Unit 3 are only about 2×10^{-3} A/m and 0.07, respectively. The fact that the magnetic intensity and Q in Unit 3 are significantly lower than those of the overlying basement units probably reflects a change in deformation intensity. The increase in susceptibility toward the bottom of Unit 3 (Core 173-1067A-23R) appears to be consistent with the significant increase in the amount of pyrrhotite observed in the smear slides from that core.

Useful paleomagnetic results were obtained only from some of the discrete samples taken from long continuous pieces of core. As shown in Figure 19, thermal demagnetization of Samples 173-1067A-16R-2, 9–11 cm, and 173-1067A-18R-2, 77–79 cm, removed a "soft" component, probably of viscous origin, at low to intermediate temperatures (200°–500°C). After further demagnetization up to 580°–590°C, the stable component of magnetization was revealed in these samples. The unblocking temperatures and coercivities indicate that the dominant magnetic mineral in these samples is magnetite. Rocks from Unit 3, on the other hand, showed rather complicated demagnetization behavior. All the minicores from Cores 173-1067A-21R through 23R displayed signs of thermochemical alteration after thermal demagnetization above 400°C, as indicated by sharp increases in remanent intensity and susceptibility. Judging from this critical temperature, pyrrhotite is the main candidate mineral responsible for this behavior.

Preliminary paleomagnetic results from Core 173-1067A-20R (821.1 mbsf) show negative inclinations (and, hence, reversed polarity?; Fig. 20). The relatively highly oxidized material indicates that the magnetization is complex and renders any polarity evaluation suspect. We also observed a positive correlation between the angles of the stable magnetic inclination and foliation planes (Table 6). This apparent relationship suggests that these rocks acquired their magnetization during deformation. The age and origin of the magnetic signal in the basement rocks are not well understood at this time. Information is lacking about core orientation, which precludes a more detailed interpretation of the paleomagnetic data at present. It may be possible after further work to investigate whether a component of viscous remagnetization parallel to the present-day magnetic field has been recorded in these rocks that may be used to orient the azimuth of these cores to the geographic reference frame.

IGNEOUS AND METAMORPHIC PETROLOGY

Basement was penetrated to a depth of 92 m in Hole 1067A. The metamorphic rock cores consist of a series of variably deformed and brecciated amphibolites, tonalite gneisses, and meta-anorthosites. Amphibolite is the dominant lithology, making up 70%–80% of the recovered core. These rocks were first found in Section 173-1067A-14R-1 at 763.8 mbsf and continued to the bottom of the hole (855.6 mbsf; Core 173-1067A-23R). Recovery was highly variable, ranging from less that 10% in Cores 173-1067A-14R, 15R, and 17R to 92% in Core 173-1067A-23R. A total of 21.0 m of core was recovered with an average recovery of 23%.

General Lithologic Description

Three units were defined in the metamorphic rock cores (Fig. 21) largely on the basis of structural characteristics, but some lithologic and mineralogic variations are also evident. In brief, basement Unit 1 is characterized by strongly foliated amphibolite and tonalite gneiss; Unit 2 is intensely brecciated, with local development of fault gouge and matrix-supported breccias; and Unit 3 is dominated by weakly to strongly foliated amphibolites and anorthosites, some of which retain original igneous textures. Tonalitic rocks are rare or absent in Unit 3.

Unit 1

Unit 1 is first encountered in Section 173-1067A-14R-1 (763.8 mbsf) and continues to the top of 18R (801.9 mbsf). Recovery in this unit was poor (9.6% recovery, 3.7 m of core). The unit consists of 75% strongly foliated amphibolite, 20% tonalite gneiss, and minor epidosite and amphibolite breccia (Fig. 21). Because of poor recovery, it is uncertain if the core is representative of the overall character of Unit 1.

The characteristic lithology of this unit is a very strongly foliated, medium- to coarse-grained greenish black amphibolite (Fig. 22). Macroscopically, the foliation is defined by elongate amphibole crystals and pods of recrystallized plagioclase (rarely plagioclase porphyroclasts) up to 4 mm in maximum dimension. In some cases, thin (<2 mm), discontinuous, felsic stringers can be traced through the rock

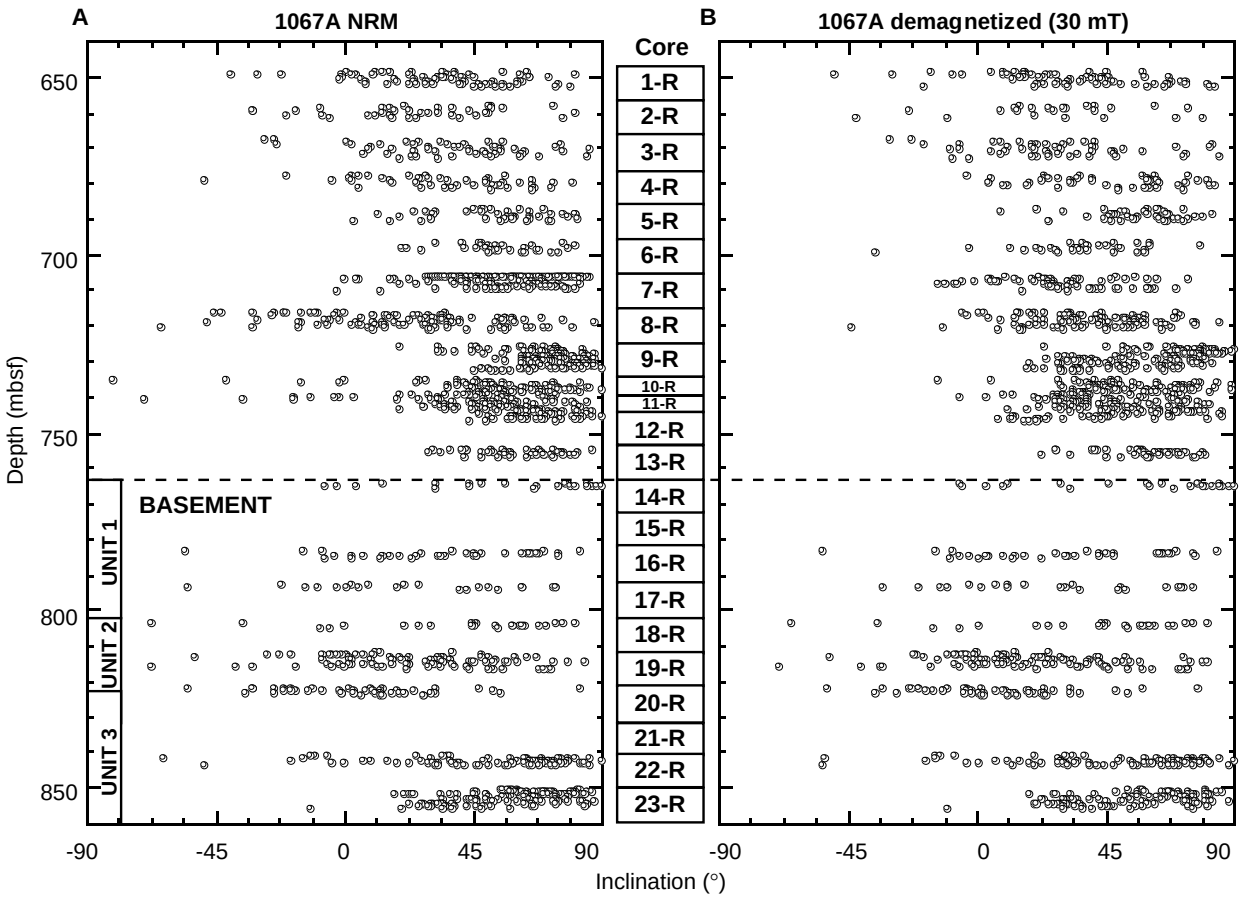

Figure 16. Downhole variation of inclination (**A**) before and (**B**) after 30-mT AF demagnetization for Hole 1067A.

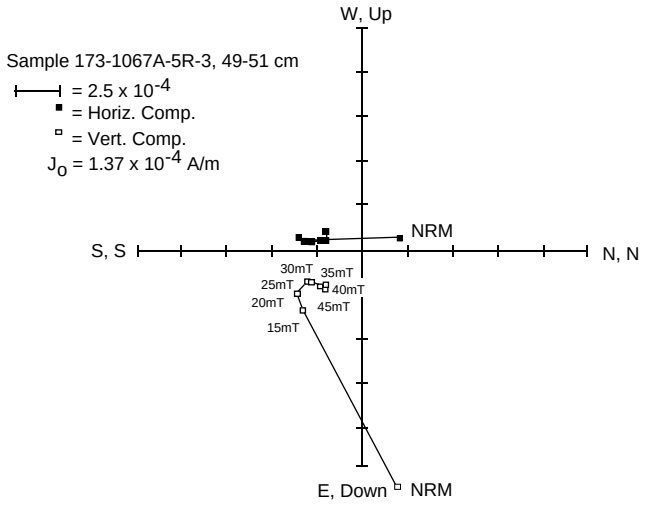

Figure 17. Representative vector end-point diagrams showing the results of AF demagnetization for discrete Sample 173-1067A-5R-3, 49–51 cm. Closed and open squares represent the projection of the magnetization vector end points on the horizontal and vertical planes, respectively (the declination values in this figure have not been corrected; see "Paleomagnetism" section, "Explanatory Notes" chapter, this volume).

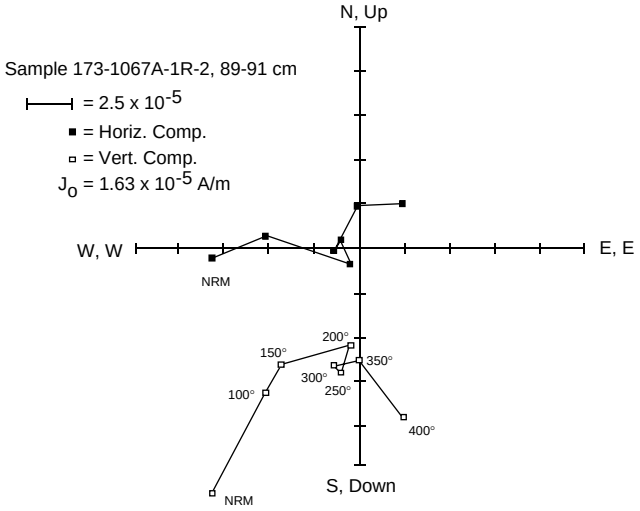

Figure 18. Representative vector end-point diagrams showing the results of thermal demagnetization for discrete Sample 173-1067A-1R-2, 89–91 cm (the declination values in this figure have not been corrected; see "Paleomagnetism" section, "Explanatory Notes" chapter, this volume). Symbols as in Figure 17.

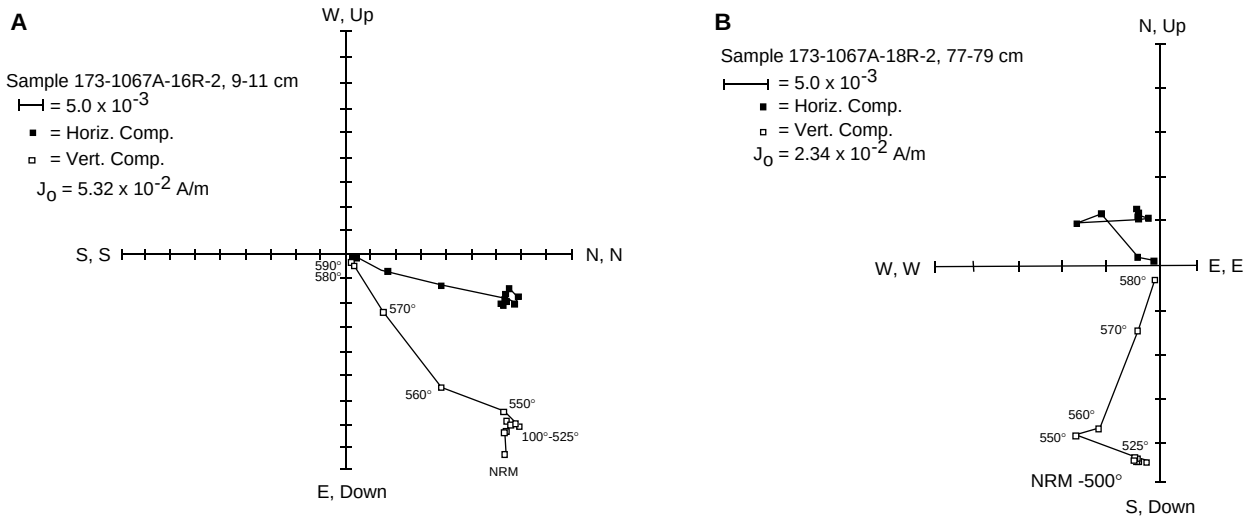

Figure 19. Representative vector end-point diagrams showing the results of thermal demagnetization for (**A**) Sample 173-1067A-16R-2, 9–11 cm, in basement Unit 1 and (**B**) Sample 173-1067A-18R-2, 77–79 cm, in basement Unit 2 (the declination values in this figure have not been corrected; see "Paleomagnetism" section, "Explanatory Notes" chapter, this volume). Symbols as in Figure 17.

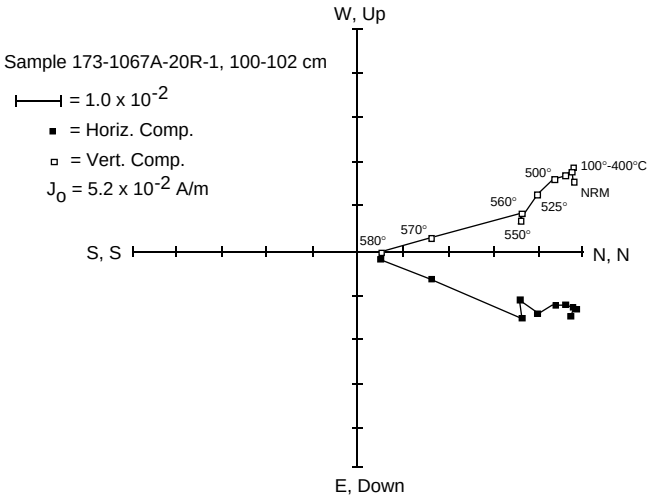

Figure 20. Vector end-point diagram of thermal demagnetization of discrete Sample 173-1067A-20R-1, 100–102 cm, from basement Unit 2, showing that the sample may be reversely magnetized (the declination values in this figure have not been corrected; see "Paleomagnetism" section, "Explanatory Notes" chapter, this volume). Symbols as in Figure 17.

Table 6. Observed inclinations of stable magnetization and the angles of foliation planes in the basement rocks, Hole 1067A.

Core, section, interval (cm)	Demagnetization range	Inclination (°)	Angle of foliation plane (° below horizontal)
173-1067A-			
Basement Unit 1			
14R-1, 49-51	560-580°C	74.7	68
16R-1, 83-85	25-70 mT	44.8	80
16R-2, 9-11	560-590°C	53.7	50
16R-2, 13-15	20-70 mT	28.1	No foliation
Basement Unit 2			
18R-2, 28-30	560-580°C	87.3	72
18R-2, 77-79	560-580°C	63.8	90
18R-2, 87-89	50-70 mT	55.6	90
19R-2, 28-30	560-580°C	18.3	No foliation
20R-1, 100-102	550-580°C	–13.9	No foliation
Basement Unit 3			
21R-1, 114-116	550-580°C	46.3	No foliation
22R-1, 29-31	570-580°C	55.6	40
23R-3, 4-6	NRM-300°C	66.3	41

Note: Demagnetization range = range of unblocking temperatures (°C) / coercivities (mT) of the characteristic component during thermal/AF demagnetization, respectively.

for several centimeters (Fig. 22). However, true compositional banding is absent in the amphibolite proper, although several samples do contain contacts with tonalitic gneiss that may originally have been intrusive. Rarely, the foliation in the amphibolite is folded around tight to open folds (see Fig. 46, "Structural Geology" section, this chapter and Frontispiece, part D). A single small piece (2 cm) of amphibolite in 173-1067A-13R-CC appears much less foliated than other amphibolites in this unit.

The tonalitic rocks are mottled, are pale red to pale orange and dark green, and are abundant in Unit 1, especially in Core 173-1067A-15R (Fig. 21). Equigranular fine- to coarse-grained (<1–5 mm) quartz and plagioclase are visible in some hand samples, but most of the tonalitic rocks are now deformed augen or microaugen tonalite gneisses (Fig. 23). In these rocks, equant to lensoid plagioclase porphyroclasts are set in a fine-grained, dark, microcrystalline matrix that, in thin section, consists largely of quartz ribbons and quartz aggregates (see "Petrography" subsection). In the coarsest augen gneisses, quartz (up to 3 mm) has crystallized within the pressure shadows of the plagioclase augen. Contacts between the tonalitic rocks and the amphibolite are commonly subparallel to the amphibolite foliation (Fig. 24). One tonalite vein or dikelet is clearly folded along with the foliation of its amphibolite host (see Fig. 46, "Structural Geology" section, this chapter). Several intervals of tonalite gneiss (e.g., Fig. 23) contain thin (1–5 mm), discontinuous bands of amphibolite parallel to the gneissic foliation.

Calcite-, epidote-, and chlorite-rich veins occur in Unit 1. Epidote- and chlorite-rich veins crosscut the foliation, the folds, and the tonalite-amphibolite contacts. They are, in turn, cut by later calcite-rich veins. Minor lithologies in Unit 1 include a single sample of epi-

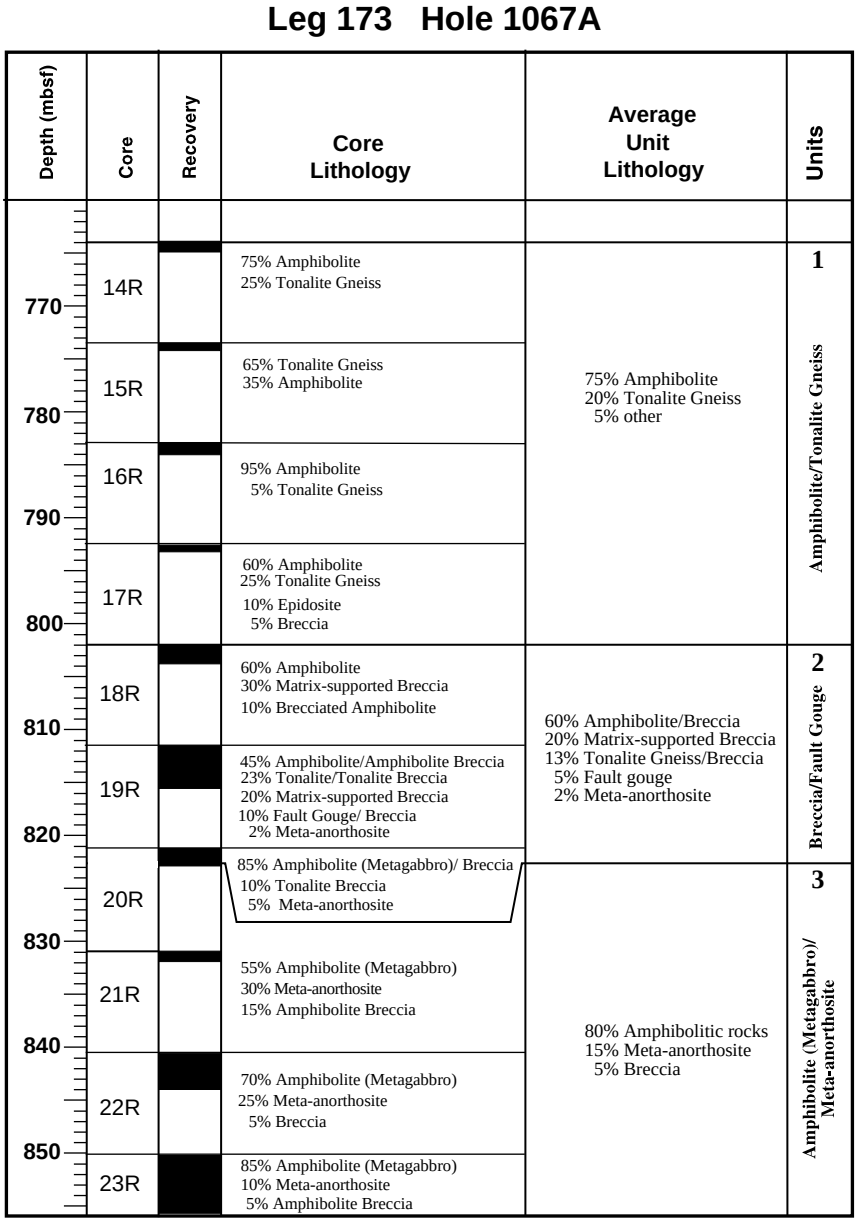

Figure 21. Schematic table showing the lithologic basis for the definitions of Units 1–3.

dosite and a few fragments of rock similar to matrix-supported amphibolite breccias that will be described in detail with the rocks of Unit 2. Both minor lithologies occur only in Core 173-1067A-17R.

Unit 2

The top of Unit 2 is defined as the top of Core 173-1067A-18R and occurs at 801.9 mbsf. The base of the unit is placed near the bottom of Core 173-1067A-20R at about 822.6 mbsf (Fig. 21). Unit 2 is defined on the basis of structural rather than lithologic characteristics and, in particular, by the presence of strongly brecciated rocks. Because of the heterogeneous nature of brecciation near the bottom of Unit 2, the placement of the lower boundary is subjective. We have placed the boundary 13 cm from the base of Section 173-1067A-20R-2, between Piece 6, a brecciated amphibolite, and Piece 7, an amphibolite (metagabbro) containing a large anorthosite pod. Average recovery from Unit 2 was 26% (7.5 m of core), of which 20% is matrix-supported breccia, 5% indurated fault gouge, and the remainder variably brecciated rocks, mostly amphibolite (60%), but including some meta-anorthosite and tonalite gneiss (15%).

Fault gouge occurs in interval 173-1067A-19R-1, 86–109 cm (see Fig. 54, "Structural Geology" section, this chapter), and in interval 173-1067A-19R-2, 117–138 cm. The upper interval of fault gouge is the better developed. It is a soft, light greenish gray rock consisting of sparse, rotated amphibolite clasts in a matrix of very fine-grained chlorite, calcite, plagioclase, and rock flour (see "X-ray Diffraction Studies" subsection, this chapter). The rock flour is presumably cemented and indurated by calcite and chlorite. The contact between the gouge and the underlying tonalitic breccia is marked by a thin vein of slickensided micro- to cryptocrystalline silica. The lower fault gouge is, in many respects, transitional between gouge and matrix-supported breccia. The cryptocrystalline to microcrystalline matrix is pale greenish yellow to dark greenish gray and appears to contain less calcite and more chlorite than the upper gouge. Clasts are

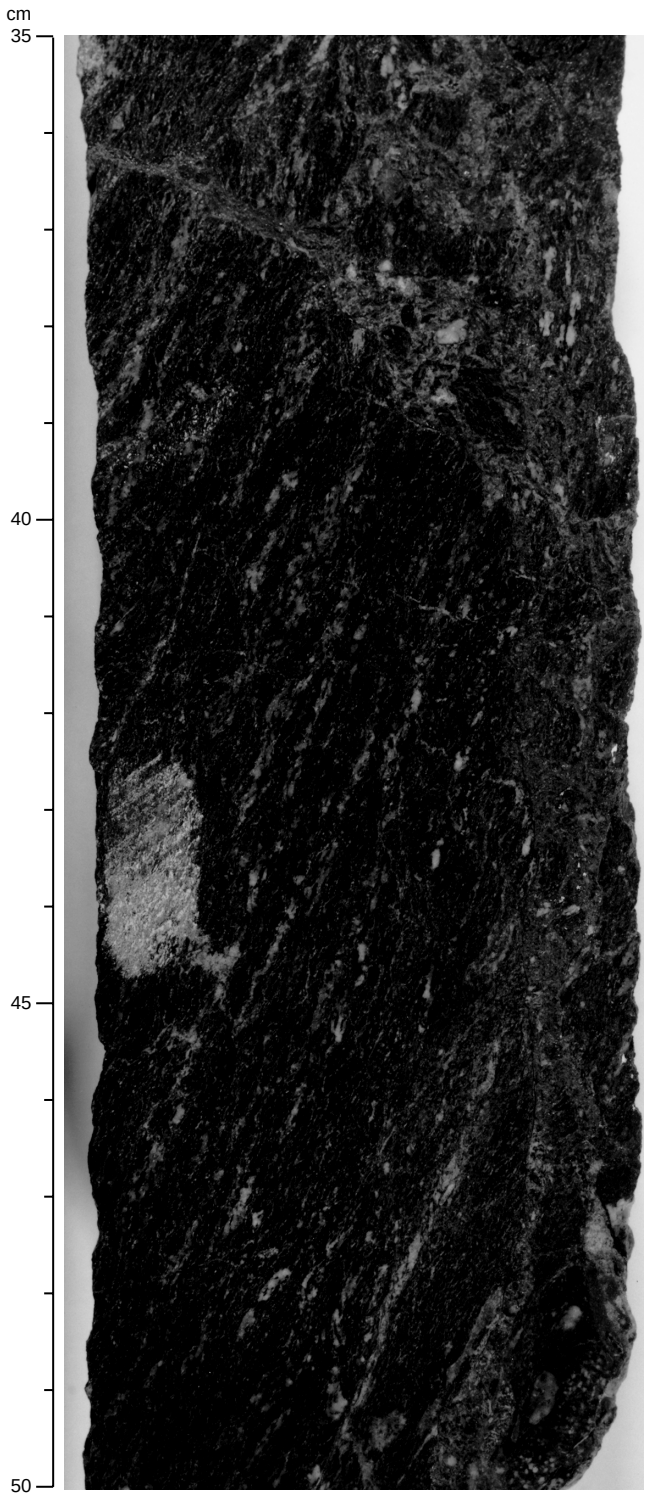

Figure 22. Typical foliated amphibolite from Unit 1 (interval 173-1067A-14R-1, 35–50 cm).

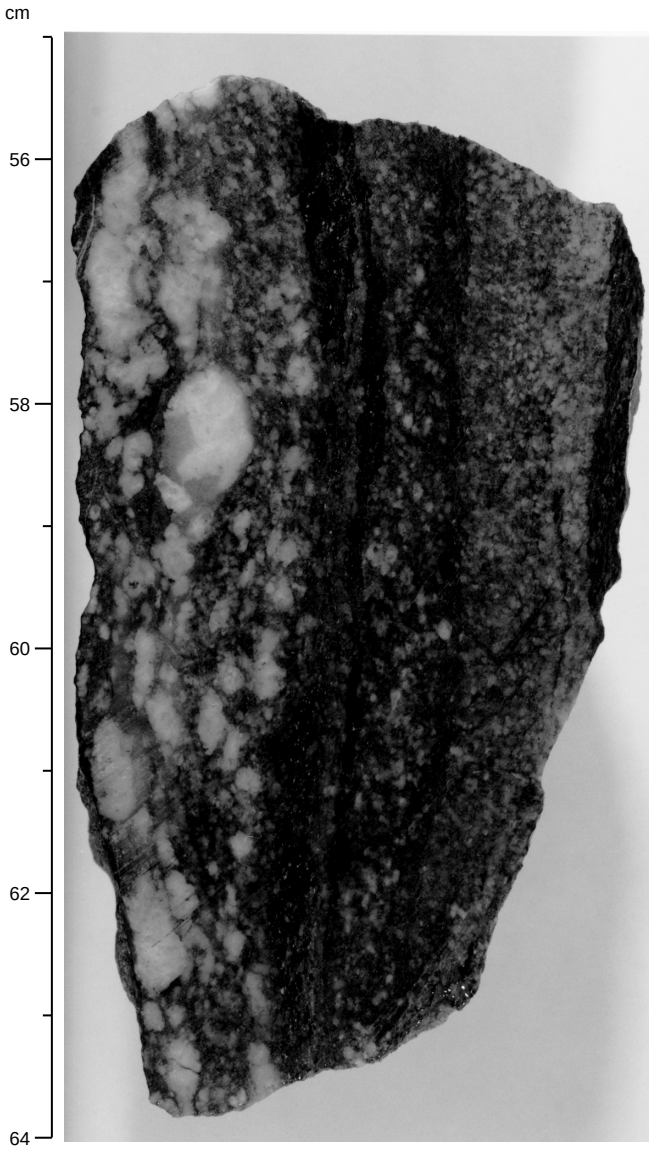

Figure 23. Typical tonalite gneiss from Unit 1 showing coarse plagioclase augen (interval 173-1067A-15R-1, 55–64 cm).

also more abundant, with quartzofeldspathic material more abundant than rotated amphibolite.

Matrix-supported breccias occur at the top of Unit 2 in Core 173-1067A-18R and sporadically throughout Sections 173-1067A-19R-1 and 2, as far down as the lowermost fault gouge. The breccia consists of a matrix of soft, greenish gray microcrystalline chlorite, calcite and rock flour (see "X-ray Diffraction Studies" subsection, this chapter) which contains 30%–70% clasts of rotated, foliated amphibolite, along with less abundant clasts of quartzofeldspathic and epidote-rich lithologies. The presence of finely divided plagioclase and amphibole and the absence of clay minerals or obviously sedimentary calcite in the matrix-supported breccias suggest that they are tectonic rather than sedimentary in origin.

An epidote-rich, intensely veined and altered breccia occurs beneath the upper fault gouge in Core 173-1067A-19R at the bottom of Section 1 and the top of Section 2. It is difficult to ascertain the protolith of this breccia or, in many cases, to define exactly where veining and "epidotization" ends and protolith clast begins. A few clasts appear amphibolitic, but many appear similar to strongly deformed tonalitic gneisses such as those from Unit 1. Thin sections from this breccia contain abundant plagioclase and strained, polycrystalline quartz, also suggesting a protolith rich in (if not dominated by) tonalite gneiss.

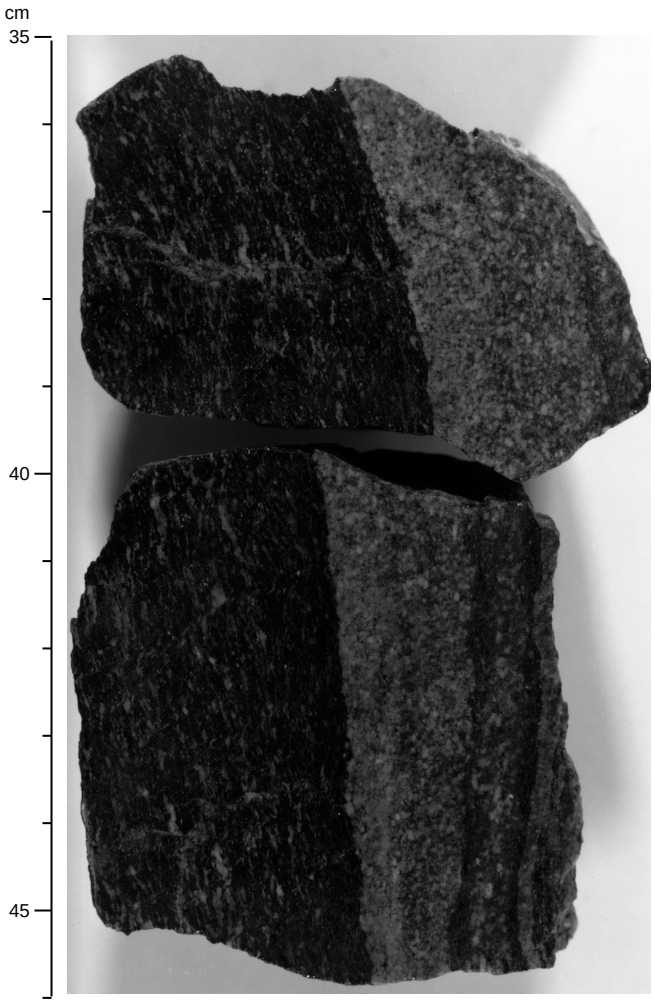

Figure 24. Contact between amphibolite and tonalite gneiss from Unit 1 (interval 173-1067A-15R-1, 35–46 cm).

Most of the remainder of Unit 2 consists of inhomogeneously brecciated amphibolite and meta-anorthosite. Brecciation ranges from fragmentation of the rock on a subcentimeter scale to relatively sparse veining. Even in the most intensely brecciated amphibolite, relicts of pre-existing fabric are recognizable. The pre-brecciation foliation in amphibolite from below the lower fault gouge appears to be relatively inhomogeneously developed and is often weaker than the foliation in Unit 1 amphibolites.

Veins in Unit 2 include epidote- and calcite-rich veins with the same general crosscutting relations seen in Unit 1. Chlorite-rich veins similar to those in Unit 1 also occur. The relative timing of veining and brecciation is complex (see “Structural Geology” section, this chapter), but the epidote veins are generally disrupted by the brecciation, while the calcite veins appear to postdate it. Some calcite veins are lined with drusy crystals. Chlorite veining appears to be associated with the brecciation.

Unit 3

Unit 3 includes the last 13 cm of Core 173-1067A-20R and all of Cores 173-1067A-21R through 23R. The top of the unit is at 822.6 mbsf, and it continues to the bottom of Hole 1067A at 855.6 mbsf (Fig. 21); a total of 9.8 m of core was recovered. The average recovery was 39%, but the recovery in Core 173-1067A-23R was 92%.

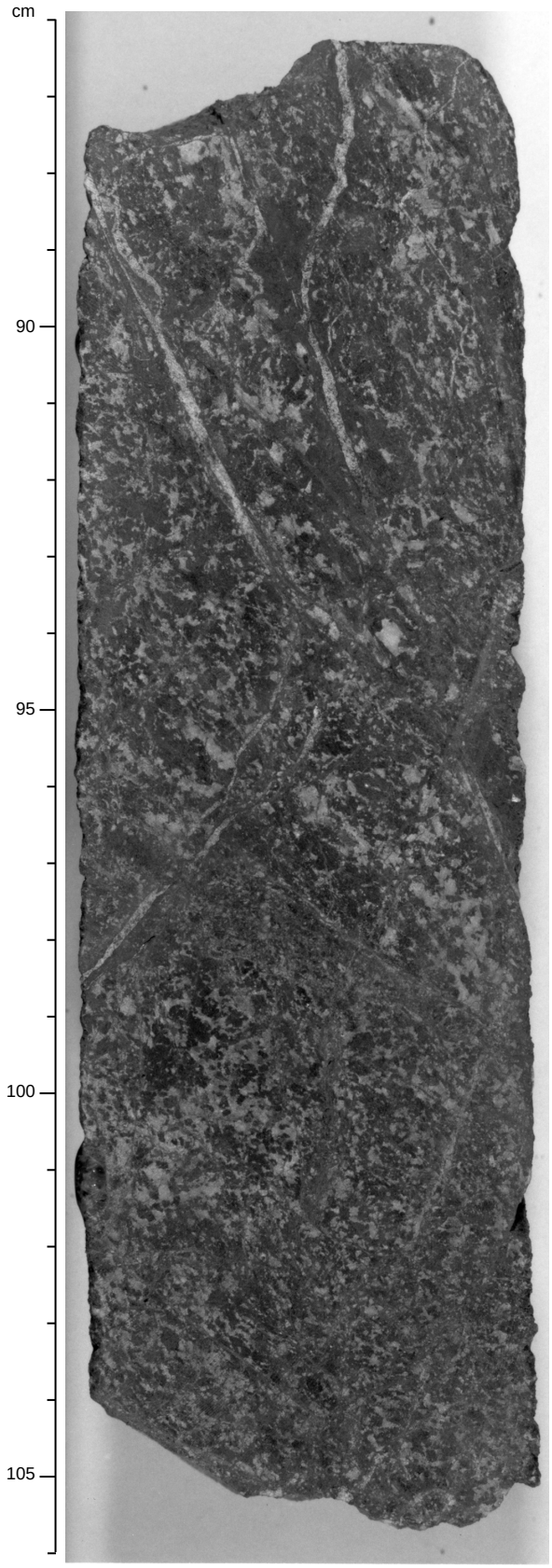

Figure 25. Amphibolite with relict hypidiomorphic to subophitic texture from Unit 3 (interval 173-1067A-22R-1, 86–106 cm). The amphibolite has been cut by veins of calcite, epidote, and chlorite.

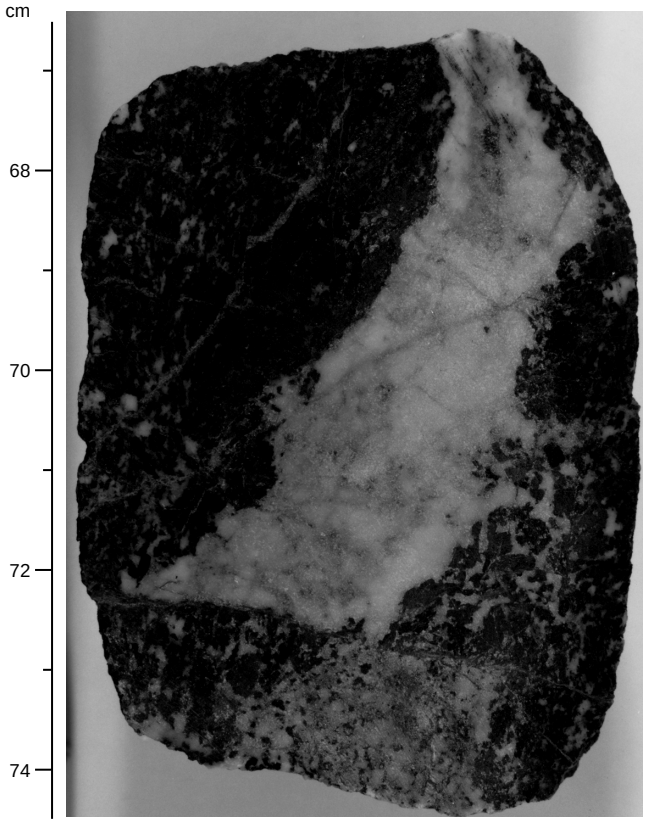

Figure 26. Typical anorthositic lens in amphibolite from Unit 3 (interval 173-1067A-20R-2, 66.5–74.5 cm). Note that some contacts are sharp, but the boundary is more diffuse in the lower part of the figure.

Core 173-1067A-23R includes one continuous segment nearly 2.5 m in length (bottom of Section 173-1067A-23R-1 to top of Section 23R-2). Unit 3 consists of 80% amphibolite (metagabbro), 15% fine- to coarse-grained meta-anorthosite, and 5% amphibolite breccia. No tonalitic rocks have been identified in Unit 3.

The amphibolites of Unit 3 are variably deformed greenish black to dark greenish gray, medium- to coarse-grained (grain size generally 1–4 mm), plagioclase-hornblende rock. In places, a strong foliation, defined by elongate amphibole and plagioclase (or aggregates of recrystallized plagioclase) is developed. The most strongly deformed amphibolites in this unit are effectively indistinguishable in hand sample from Unit 1 amphibolites. However, much of the amphibolite in Unit 3 is weakly foliated and, in some cores (e.g., Sections 173-1067A-22R-1 and 23R-2), it appears largely unfoliated and has relict plutonic fabrics. These include mesoscopic (and microscopic) hypidiomorphic to sub-ophitic textures (Fig. 25). One amphibolite (Section 173-1067A-23R-3) contains garnet (see "Petrography" subsection). Discontinuous, uneven, compositional banding, defined by elongate plagioclase-rich pods (meta-anorthosites) is seen in some of the more highly deformed amphibolites. The amphibolites are locally brecciated.

Two mesoscopically distinct examples of anorthositic rock types occur in Unit 3. The more obvious rock type has relatively coarse-grained, white plagioclase pods, patches, and lenses (about 5% of the core; Fig. 26). One such pod appears to contain a subhedral plagioclase crystal over 1 cm across. These pods often appear to have been disaggregated during foliation formation. In the most deformed amphibolites, plagioclase-rich pods are generally subparallel to the foliation and may be strung out along it. In relatively undeformed amphibolite, contacts with the coarse-grained meta-anorthosites are more diffuse. Other finer grained anorthositic rocks (10% of Unit 3) appear mesoscopically as dispersed, equant, angular to rounded plagioclase grains (1–2 mm) in a dark greenish black matrix (Fig. 26), locally grading into coarser grained, pinkish anorthositic amphibolites (metagabbros?). These rocks tend to occur in larger bodies than the coarse-grained meta-anorthosites, commonly making up most or all of several centimeters or even tens of centimeters of core. These finer grained meta-anorthosites appear to be preferentially associated with relatively deformed Unit 3 amphibolites.

Veins in Unit 3 include epidote, calcite, and chlorite. Calcite veining is late, cutting all other features of the rock. Some of these veins are open and contain drusy calcite. Epidote- and chlorite-rich veins cut the foliation in the amphibolite (see "Structural Geology" section, this chapter).

Petrography

In order to better constrain the microstructural and mineralogical characteristics of the metamorphic basement cores recovered from Hole 1067A, 31 thin sections were made that include the full range of lithologies and structures. In this section, petrographic observations from the main rock types (amphibolites, tonalite gneisses, meta-anorthosites, cataclastic breccias, and veins) are described and discussed in detail. These observations are summarized in Table 7.

Amphibolites

Typical amphibolite consists of 50%–70% green-brown to blue-green amphibole and 20%–30% plagioclase ($An_{31–36}$). In Unit 1, the amphibole is typically blue-green, whereas in Unit 3 it is distinctly green-brown. Quartz, chlorite, epidote, and rare garnet account for 10%–20% of the amphibolite. Fe-opaque minerals (mainly ilmenite), apatite, zircon, and sphene are present as accessory minerals. Ilmenite is particularly abundant (up to 2%) in Core 173-1067A-23R (Unit 3). The amphibolite has a well-developed foliation in Unit 1 (Fig. 27; Table 7) and weakly developed foliation in Unit 3 (Fig. 28). The foliation is defined by elongate patches of recrystallized plagioclase and alignment of prismatic elongated amphibole and is locally folded (Fig. 29). In the weakly deformed amphibolite from Unit 3, some relict igneous textures are preserved; for example, euhedral plagioclase (Fig. 30) is included in poikilitic amphibole (replacing pyroxene?). These igneous textures are overprinted by the foliation (Table 7).

In most of the thin sections, plagioclase is partially replaced by sericite, epidote and clay minerals. The amphibole is relatively fresh when compared to the other phases, but in some samples from Unit 1, amphibole is partially to totally replaced by chlorite. Porphyroblastic garnet, where present, is partially replaced by chlorite. Pervasive replacement of plagioclase and amphibole by epidote, albite, and chlorite occurs within microfractures, cleavage planes, and grain edges. This retrograde metamorphism is commonly associated with shallowly inclined veins, filled with epidote, plagioclase and chlorite, which crosscut the foliation. Late white calcite veins are mainly subvertical and perpendicular to the foliation. In Unit 2, as vein density increases in the amphibolites, veining is often transitional into cataclasis (see "Structural Geology" section, this chapter; Table 7). Also locally in Unit 2, amphibolite is transformed into epidosite, presumably in areas of intense fluid circulation.

The mineralogical and structural evolution of the amphibolites, deduced from petrographic evidence, can be summarized as follows. Relict igneous textures in the weakly deformed amphibolites suggest that they were formed in an early magmatic event (magmatic stage in Fig. 31). Euhedral plagioclase included in poikilitic amphibole and regions of subhedral equigranular plagioclase indicates a gabbroic origin. It is unclear whether amphibole originally crystallized from a melt (hornblende gabbro) or formed by replacement of magmatic py-

Table 7. Main mineralogical and textural characteristics of Hole 1067A rock types based on petrographic evidence.

Core, section, interval	Strong foliation	Folded foliation	Weak foliation	Igneous texture	Epidosite	Cataclasite	Veins
173-1067A-							
Unit 1							
13R-CC, 24-25			Amph				Cal/lim
13R-1, 138-141							
14R-1 (Piece 2, 4-8 cm)	?						
14R-1 (Piece 3, 8-15 cm)	Tona						Oxi
14R-1 (Piece 8, 17-18 cm)	Amph						Chl/epi
14R-1 (Piece 1, 87-91 cm)	Tona						Qtz/chl/epi
15R-1 (Piece 1, 0-4 cm)	Tona						Chl/epi
15R-1 (Piece 8A, 37-39 cm)	Amph/tona	Amph/tona		Tona		Chl	
15R-1 (Piece 11, 57-59 cm)	Tona						
16R-1 (Piece 4, 15-18 cm)	Tona						
16R-1 (Piece 1B, 5-9 cm)	Amph						
16R-1 (Piece 15, 103-106 cm)		Tona					
16R-2 (Piece 1B, 5-9 cm)	Amph						Cal
17R-1 (Piece 12, 82-85 cm)					Epid		
Unit 2							
18R-2, (Piece 7B, 89-91 cm)	Amph					Amph	Chl/cal
19R-1 (Piece 5C, 41-44 cm)	Amph/anor	Amph/anor		Anor			
19R-1 (Piece 7D, 108-112 cm)						Amph/tona/epi	
19R-2 (Piece 1B, 38-41 cm)						Amph/tona/epi	
19R-3 (Piece 3, 14-16 cm)						Amph/tona/epi	
20R-1 (Piece 5B, 70-72 cm)	Amph						Chl/epi
20R-1 (Piece 5B, 80-83 cm)		Amph					Cal
Unit 3							
21R-1 (Piece 16, 101-104 cm)						Amph	Plg
22R-2 (Piece 1, 3-6 cm)			Amph				Epi
22R-2 (Piece 3, 43-47 cm)			Anor				
22R-2 (Piece 4, 92-96 cm)				Amph/anor			
23R-1 (Piece 2B, 30-33 cm)						Amph	
23R-1 (Piece 2E, 113-116 cm)			Gnt/amph				Chl/epi
23R-2 (Piece 1C, 70-73 cm)			Amph			Amph	
23R-2 (Piece 1C, 80-83 cm)			Amph				
23R-2 (Piece 1D, 107-111 cm)			Amph	Amph			
23R-3 (Piece 1A, 19-23 cm)	Amph						
23R-4 (Piece 1, 1-4 cm)						Amph	
23R-4 (Piece 8, 74-77 cm)	Amph						Epi/chl/oxi
23R-5 (Piece 4C, 33-36 cm)			Amph/anor	Amph/anor			

Notes: Abbreviations for rock types: amph = amphibolite, anor = meta-anorthosite, epid = epidosite, and tona = tonalite gneiss. Abbreviations for minerals: cal = calcite, chl = chlorite, epi = epidote, gnt = garnet, lim = limonite, oxi = Fe-oxides, plg = plagioclase, and qtz = quartz.

roxene gabbro under later amphibolite facies (subsolidus) conditions. This magmatic stage has been overprinted by an amphibolite facies event giving rise to the development of a pervasive foliation defined by recrystallization of plagioclase and alignment of elongated amphibole (metamorphic stage I, Fig. 31). The recrystallization of plagioclase and amphibole demonstrates that the deformation took place under medium temperature conditions (amphibolite facies). Metamorphism continued under greenschist facies conditions and was largely facilitated by fluid infiltration (see "Structural Geology" section, this chapter), as suggested by the pervasive and static replacement of amphibole and plagioclase by chlorite and epidote, respectively, and by the occurrence of veins filled with epidote, albite, and chlorite (metamorphic stage II, Fig. 31).

Tonalite Gneiss

Tonalite gneiss occurs mainly in Unit 1 as <1- to 5-cm-wide layers that are concordant to slightly discordant with respect to the foliation in the amphibolites. In some cases, the tonalite gneiss layers are folded together with the amphibolite host (Table 7). The tonalite gneisses are commonly porphyroclastic to inequigranular (Fig. 32) and are composed of 60%–70% plagioclase (An_{20}) and 10%–20% quartz. Apatite, sphene, brown biotite, and zircon are present as accessory minerals. In thin section, gneissic textures of the tonalites are defined by 2- to 3-mm-wide quartzofeldspathic layers including porphyroclasts and neoblasts alternating with green biotite-rich layers (augen texture). In less deformed tonalites, some relict igneous textures, defined by subhedral plagioclase and brown biotite, are observed (magmatic stage; Fig. 33). Extensive dynamic recrystallization and reorientation of quartz and biotite and minor recrystallization halos surrounding plagioclase indicate a medium-grade deformational overprint (metamorphic stage I; Fig. 33). Veins and veinlets filled with epidote, albite, and epidote-quartz crosscut the metamorphic foliation (metamorphic stage II; Fig. 33).

Meta-anorthosite

The meta-anorthosites occur within the amphibolite in Unit 3 as lenses that are concordant or slightly discordant to the foliation (e.g., Samples 173-1067A-22R-2 [Piece 4, 92–96 cm], and 23R-5 [Piece 4, 33–36 cm]. These lenses are folded together with the host amphibolite in Sample 173-1067A-20R-2 (Piece 7, 66–73 cm). The textures of the meta-anorthosites range from equigranular to inequigranular (Fig. 34). The meta-anorthosites are composed of 80% plagioclase (An_{10} or An_{30}) and 20% chlorite, amphibole, epidote, and sericite. Relict igneous textures (for example, subhedral equigranular plagioclase + apatite ± amphibole) are very well preserved (e.g., Samples 173-1067A-22R-2 [Piece 4, 92–96 cm] and 173-1067A-23R-5 [Piece 4, 33–36 cm]). A weak foliation defined by the preferred orientation of the recrystallized plagioclase is observed in Sample 173-1067A-19R-1 (Piece 5C, 41–44 cm). Pervasive retrograde metamorphism of amphibole to chlorite, together with albite and epidote veining, occurred in the greenschist facies. The magmatic and metamorphic stages that affected the amphibolites, tonalite gneisses, and meta-anorthosite are summarized in Figure 35.

Breccia

Two types of breccia occur in Unit 2, polygenic breccia and "in situ" breccia. The polygenic breccias consist of amphibolite, tonalite, and epidosite fragments (see Table 7) within a matrix of very fine-grained epidote (<0.01 mm). These breccias have been observed

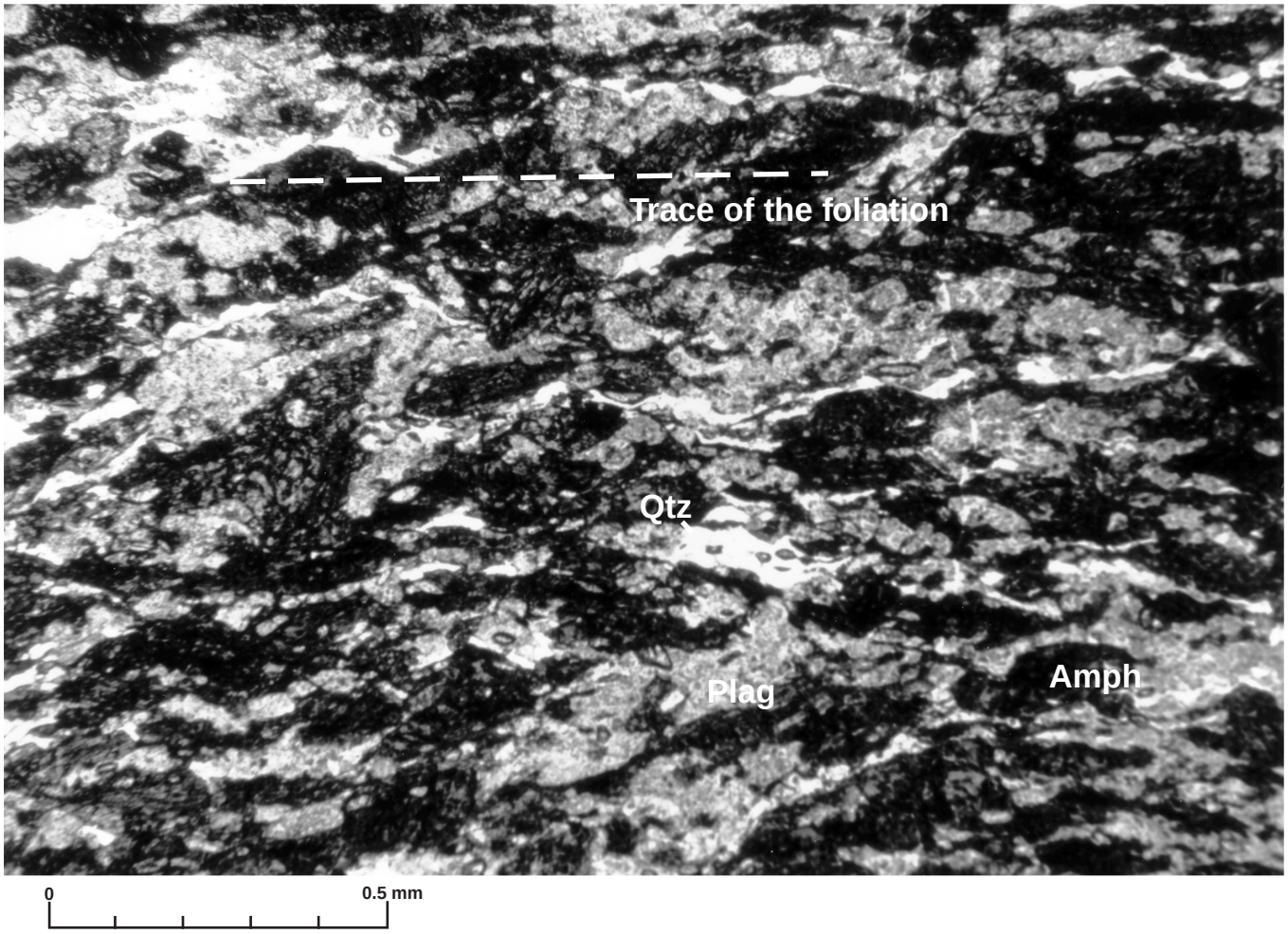

Figure 27. Photomicrograph of Unit 1 amphibolite with well-developed foliation (Sample 173-1067A-16R-2 [Piece 1B, 5–9 cm]). Mineral abbreviations are the same as those in Table 7.

mainly at the contact between amphibolite and tonalite gneiss. Fine-grained (<1 mm) foliated amphibolites in which amphibole and plagioclase have been replaced by chlorite and sericite, respectively, account for less than 20% of the clasts. The medium-grained (<4 mm) tonalite gneiss clasts make up to 60% of the clasts. The presence of epidosite clasts indicates that the brecciation occurred during or after greenschist facies retrograde metamorphism. Generally the matrix of the breccia shows an enrichment of iron oxide up to 10%. The "in situ" breccia occurs in Unit 2 amphibolite and consists of angular foliated amphibolite fragments (up to 3 cm) within a connected network of fractures (1–4 mm) filled with epidote, calcite, and amphibole and plagioclase clasts constituting the matrix of the breccia.

Veins

Veins have been observed in all the lithologies and display different compositions with respect to the sequence in which they formed. In amphibolites, 0.4- to 4.0-mm-wide veins filled with epidote occur subparallel to the foliation. A second generation of 0.2- to 0.5-mm-wide veins filled with plagioclase and epidote (or chlorite) crosscuts the foliation. Late 0.5–10 mm calcite veins crosscut the foliation and the previous generation of epidote and plagioclase-epidote veins. In tonalite gneisses, <0.2-mm-wide veins are filled with quartz, epidote, and, more rarely, chlorite. In the meta-anorthosites, 0.4-mm-wide veins are filled with plagioclase and epidote. A zone of epidote veining surrounding the edges of the clasts in the polygenic breccia is common and indicates that the brecciation of the rocks occurred under greenschist facies conditions, in agreement with the development of the epidote-rich matrix in the breccia, and was facilitated in part by fluid infiltration.

X-ray Diffraction Studies

Three samples were analyzed for fine-grained mineralogy using XRD. They are the matrix of a matrix-supported tectonic breccia, the matrix of a fault gouge breccia, and the matrix of a brecciated amphibolite (Fig. 36). In all diffraction patterns, the strongest peak is plagioclase, and there are also peaks suggesting the presence of an amphibole. Chlorite is a recognizable component of all breccias. It is possible that chlorite was inherited from the amphibolite host, but the presence of chlorite in low-temperature veins elsewhere in the cores suggests that it is, at least in part, part of the low-temperature matrix assemblage. The presence of abundant calcite was confirmed by XRD analysis of the matrix-supported breccia and the fault gouge

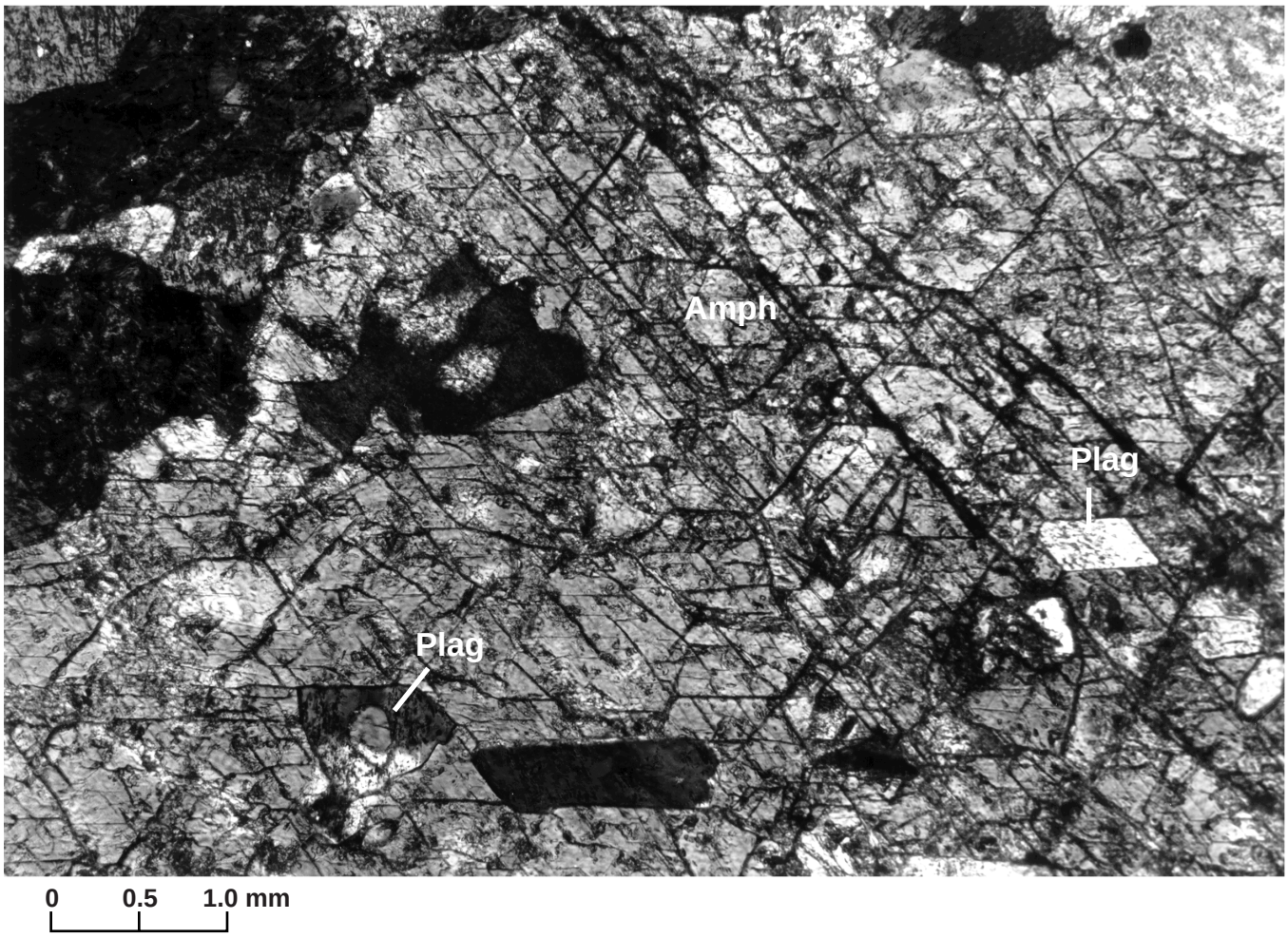

Figure 28. Photomicrograph of an amphibole in a Unit 3 amphibolite with weakly developed foliation (Sample 173-1067A-23R-2 [Piece 1D, 107–111 cm]). The plagioclase inclusions are interpreted as relict ophitic texture. Mineral abbreviations are the same as those in Table 7.

breccia. However, no calcite was found in the matrix of the brecciated amphibolite (Fig. 36C). Other minerals identified by XRD analysis are Fe-oxyhydroxide and magnetite. Magnetite was found in the fault gouge breccia and the brecciated amphibolite but was not detected petrographically in any sample, although the breccia contains abundant opaque minerals. No clay minerals were identified in the fault gouge or the matrix-supported breccia. The presence of abundant plagioclase and amphibole suggests that a major component of the breccia matrix is finely ground amphibolitic rock fragments. This suggests that the breccias are strongly cataclastic rocks. The presence of apparently unaltered finely ground amphibolite also suggests low temperature of breccia formation.

Major and Trace Element Geochemistry

Ten representative samples of the basement cores were chosen for shipboard whole-rock X-ray fluorescence (XRF) analysis. Of these samples, seven are amphibolites from Units 1–3, one is a tonalite gneiss from Unit 1, and two are matrix samples from breccias in Unit 2 (Table 8). The amphibolites were chosen from areas that did not exhibit mesoscopic tonalitic or anorthositic patches or veins.

In general, the amphibolites are amphibole-plagioclase rocks with mafic to intermediate compositions of 41.83 to 53.60 wt% SiO_2, whereas the tonalite gneiss is a plagioclase-quartz rock with a felsic composition of 76.30 wt% SiO_2. The breccia matrix samples have major and trace element compositions within the range of values for amphibolites. The TiO_2 abundances of the amphibolites are highest at the top of Unit 1 and bottom of Unit 3 (2.35–3.4 wt%; Fig. 37) compared to the rest of the amphibolites (2.00–2.17 wt%) and the breccia matrix samples (1.77–1.87 wt%). Mg-numbers range from 51 to 57 for the amphibolites and from 53 to 59 for the matrix samples (Fig. 37). However FeO*/MgO ratios of the amphibolites and the matrix samples are more uniform (Fig. 37).

Elements such as Ti, Y, Zr, and Nb are considered to be generally immobile during metamorphism (Ludden and Thompson, 1979). The Y abundances of all the samples range from 23 to 51 ppm, whereas the Zr contents vary from 108 to 420 ppm in the amphibolites, 137 to 208 ppm in the breccias, and 140 ppm in the tonalite gneiss (Table 8; Fig. 38). The trace element enrichments in the upper and lowermost amphibolites correspond with those showing the highest TiO_2 contents (Figs. 37, 38). The extreme Zr enrichment in Sample 173-1067A-23R-3, 19–23 cm, probably results from zircon accumulation within this sample as observed in thin section. V and Zn abundances in the amphibolites are fairly constant downhole (Fig. 38); they do not show an increase in Core 173-1067A-23R as expected from petrographic evidence for an increase in the modal proportions of Fe-Ti

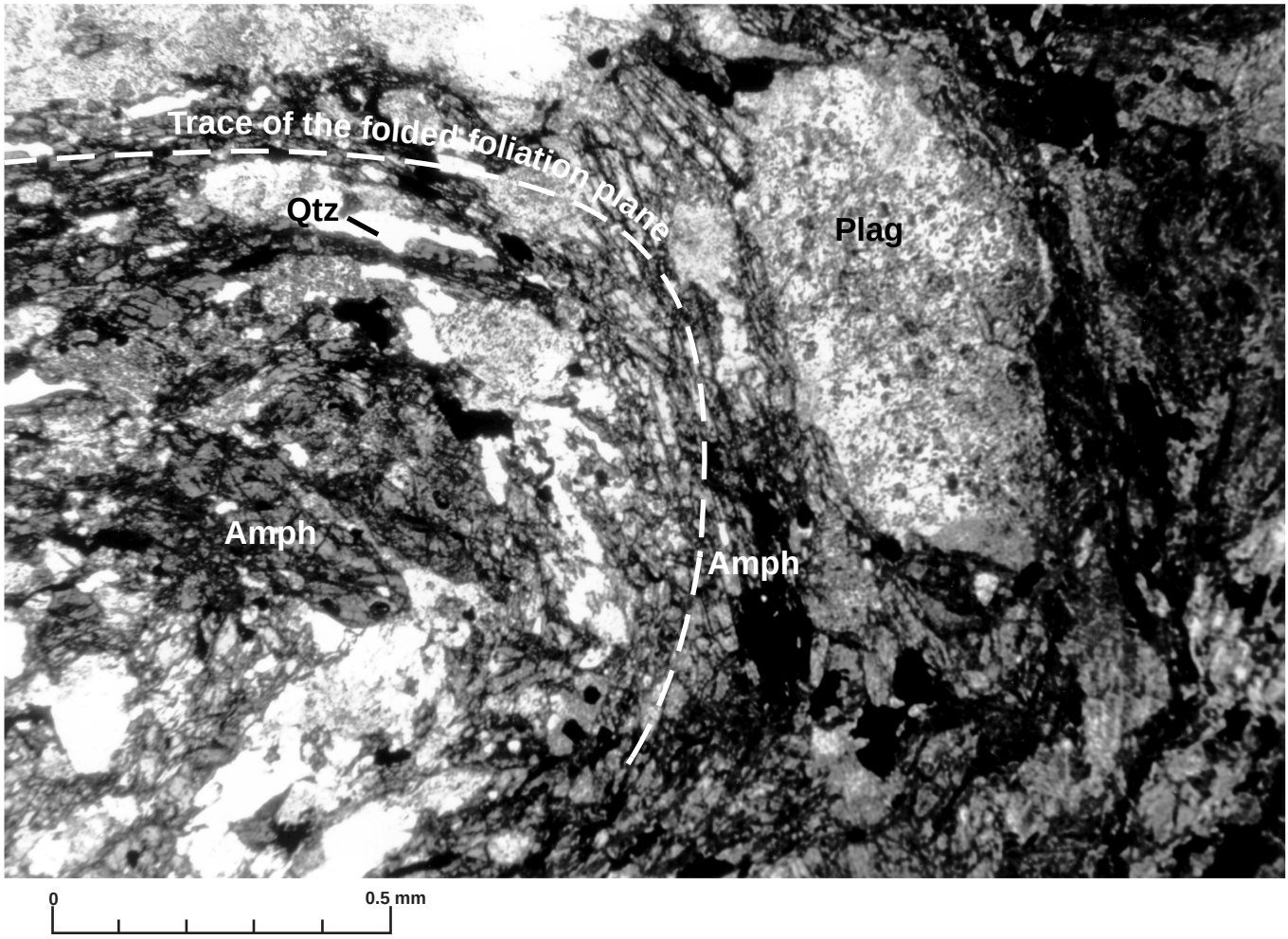

Figure 29. Photomicrograph of Unit 1 folded amphibolite (Sample 173-1067A-16R-1 [Piece 15, 103–106 cm]). Mineral abbreviations are the same as those in Table 7.

oxides and sphene (see "Petrography" subsection). Mobile elements, such as Ba and Sr, display compositional ranges of similar magnitudes (variation by a factor of 2 to 3) as the immobile elements. These abundances are 0 to 122 ppm Ba and 78 to 216 ppm Sr in the amphibolites, 116 ppm Ba and 101 ppm Sr in the tonalite gneiss, and 46–163 ppm Ba and 194–275 ppm Sr in the breccia matrix samples (Fig. 38). The compositional range exhibited by the breccia matrix samples of Unit 2 is thus consistent with petrographic and XRD evidence that these samples are variable mixtures of amphibolite and metaanorthosite.

Comparison of this suite of amphibolites with basement rocks obtained from the southern Iberia Abyssal Plain cored during Leg 149 and with rocks produced at mid-ocean ridges, such as oceanic gabbros, may provide insight into the origin of these metamorphic rocks. Hole 1067A is located 800 m from Leg 149 Hole 900A on the same basement structural high. Metagabbros from Site 900 (Sawyer, Whitmarsh, Klaus, et al., 1994; Cornen et al., 1996; Seifert et al., 1996) are more primitive (higher Mg-numbers and higher compatible element abundances such as Ni) and have significantly lower incompatible element abundances such as TiO_2 (Fig. 39) compared to the amphibolites from Site 1067. Metamicrogabbros from Site 899 (Cornen et al., 1996), from a breccia deposit on a basement structural high 52 km to the west of Site 1067, also appear to be slightly more primitive than the amphibolites from Site 1067 (Fig. 39). Amphibolites from Site 1067 also remain distinct in whole-rock trace element composition from the Site 899 metamicrogabbros and the Site 900 metagabbros (Figs. 39, 40). When compared with oceanic gabbros, Site 900 metagabbros are comparable to primitive gabbros from the Southwest Indian Ridge recovered during Leg 118 (Robinson, Von Herzen, Adamson, et al., 1989) and primitive gabbros from the Mid–Atlantic Ridge recovered during Leg 153 (Cannat, Karson, Miller, et al., 1995). Metamicrogabbros from Site 899 are comparable to the Fe–Ti gabbros from Leg 118 (Fig. 40), whereas the Site 1067 amphibolites are similar to the most evolved gabbroic rocks from Leg 118 (Fig. 40).

To understand better the trace element characteristics of the basement rocks from Site 1067, we have compared them with average values for normal mid-ocean ridge basalt (N-MORB), enriched mid-ocean ridge basalt (E-MORB), and ocean island basalt (OIB). When the trace element compositions of Site 1067 amphibolites are normalized to average N-MORB values, they exhibit enrichments over N-MORB with an inclined extended trace element pattern (Fig. 41). When normalized to E-MORB, the Site 1067 amphibolites show a flatter extended trace element pattern (Fig. 41). Relative to ocean is-

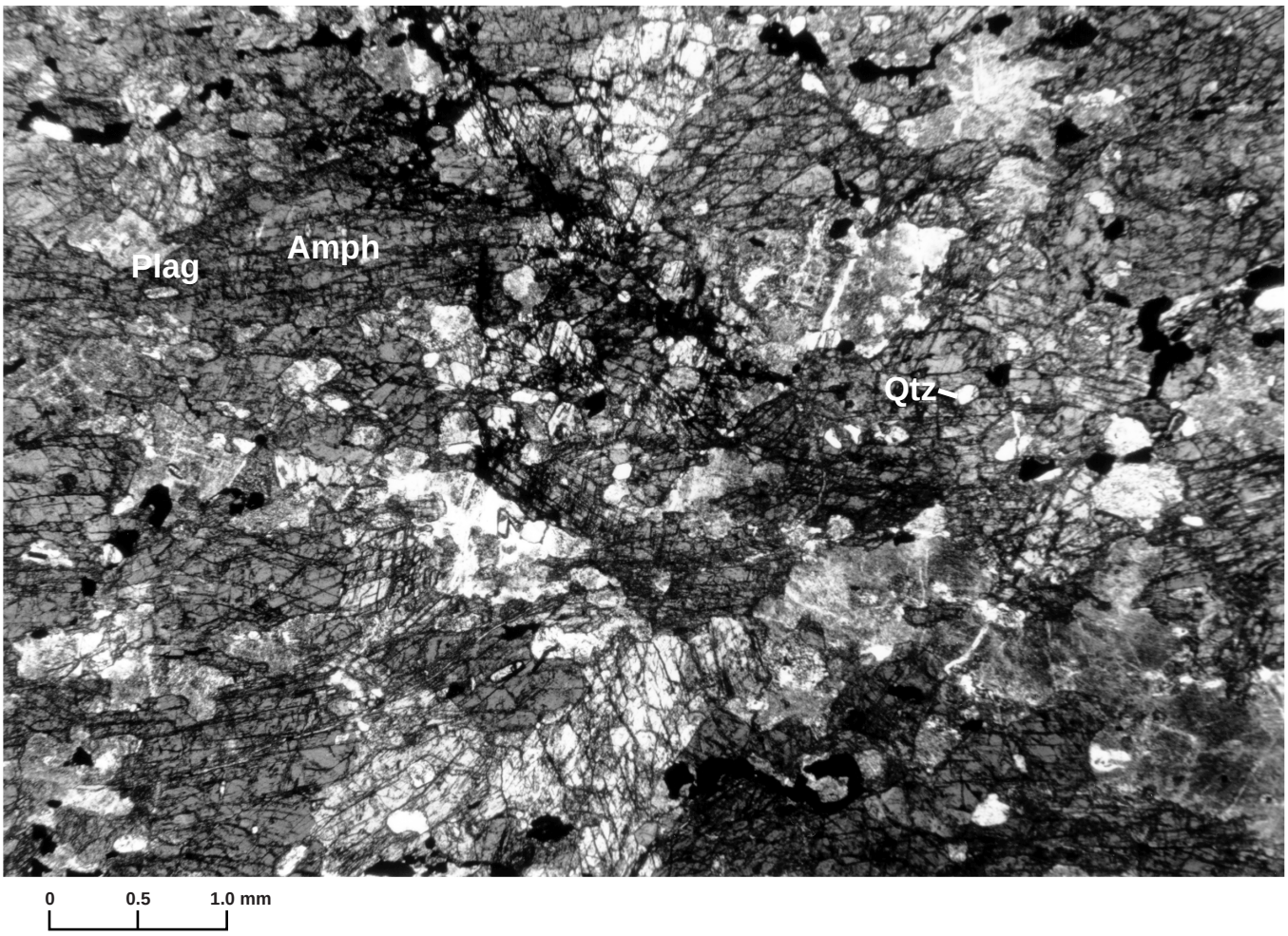

Figure 30. Photomicrograph of relict igneous textures, including euhedral plagioclase hosted in poikilitic amphibole (Sample 173-1067A-22R-2 [Piece 4, 92–96 cm]). Mineral abbreviations are the same as those in Table 7.

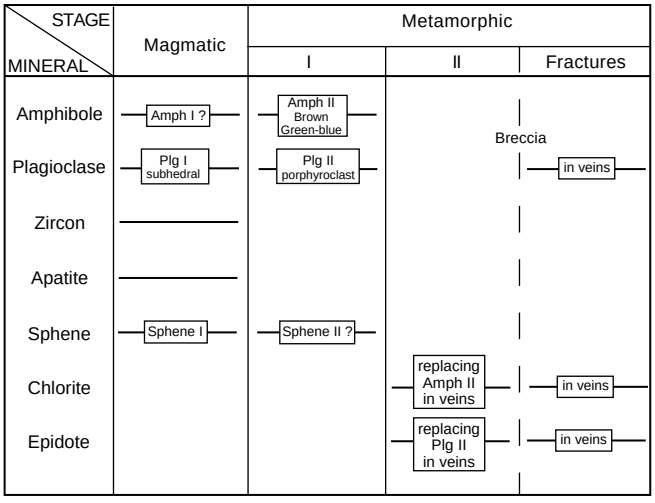

Figure 31. Mineralogical evolution of amphibolites.

land basalts (OIB), the Hole 1067A amphibolites are depleted (Fig. 41). If the protoliths for Site 1067 amphibolites were evolved oceanic gabbros, then the melts from which they originally crystallized were probably similar to enriched tholeiitic E-MORB rather than alkalic (OIB) magmas. This result is consistent with the Site 900 metagabbros crystallizing possibly from a tholeiitic liquid that was transitional between N- and E-MORB compositions (Cornen et al., 1996) but does not distinguish between a mid-ocean ridge, island arc, or continental magmatic origin. Additionally, the Site 1067 amphibolites are more evolved than the Site 900 metagabbros despite the close proximity of the sites which are both located on the same basement high.

STRUCTURAL GEOLOGY

Site 1067 is located on the eastern flank and close to the top of a basement ridge in the ocean/continent transition of the southern Iberia Abyssal Plain. It is situated 800 m east of Site 900 (Leg 149), where the basement consists predominantly of flaser gabbro (Sawyer, Whitmarsh, Klaus, et al., 1994). Hole 1067A penetrated Eocene and Paleocene sediments and 92 m of basement rocks, which are mainly amphibolite, tonalite gneiss, meta-anorthosite, breccias, and fault gouge.

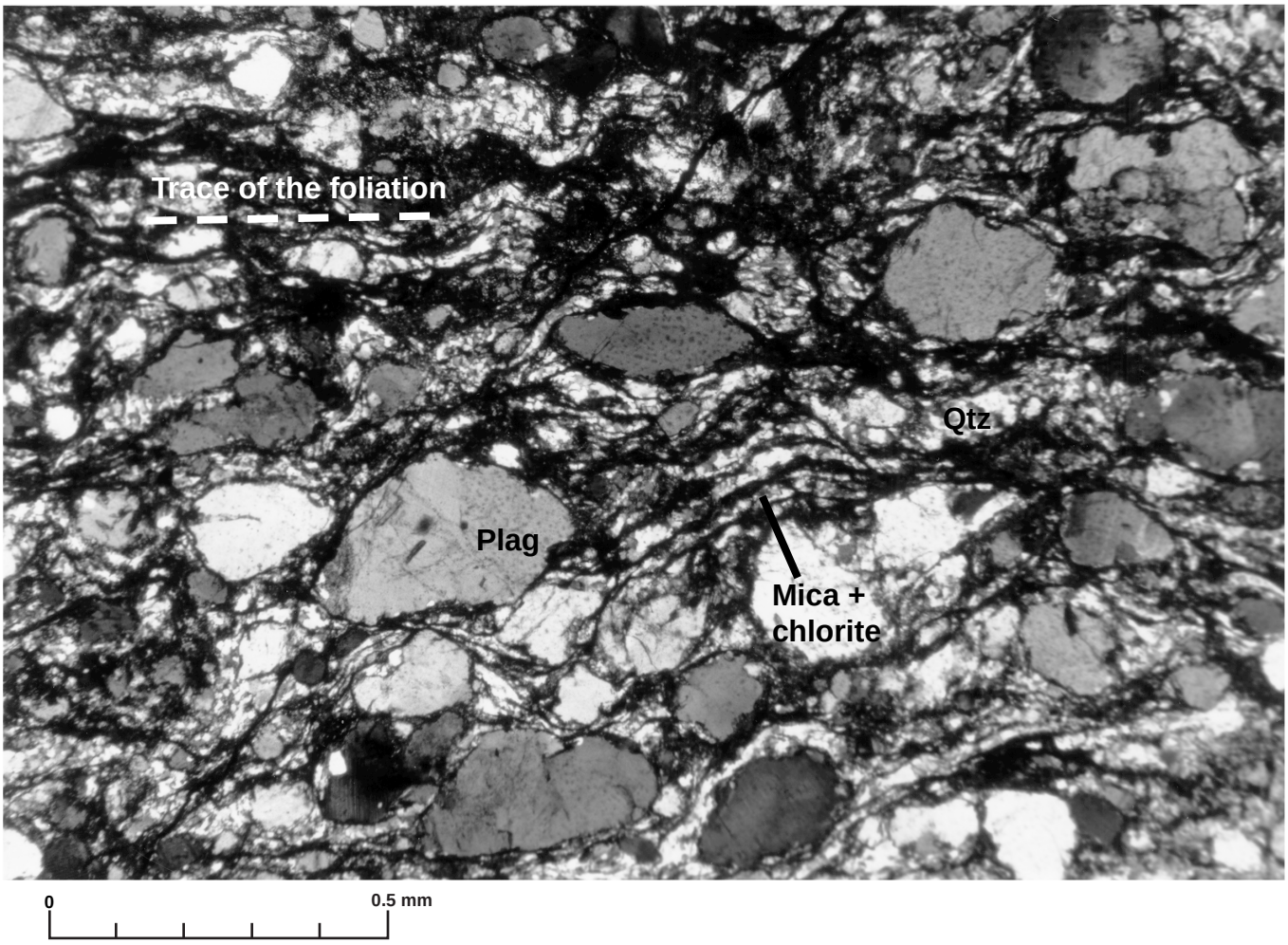

Figure 32. Photomicrograph of Unit 1 tonalite gneiss (Sample 173-1067A-15R-1 [Piece 8A, 34–39 cm]). Mica refers to biotite. Mineral abbreviations are the same as those in Table 7.

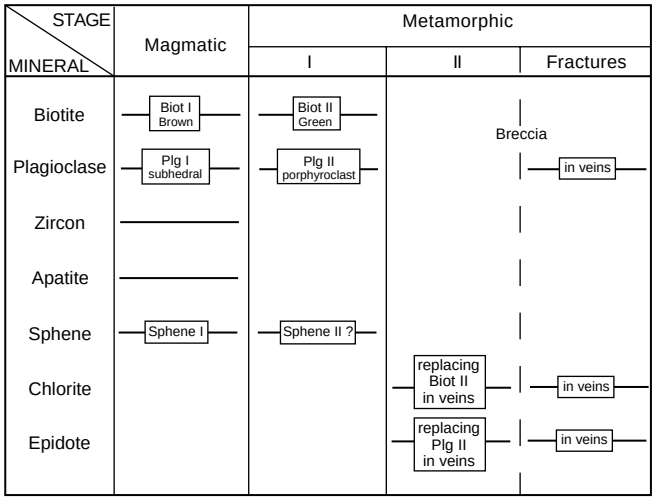

Figure 33. Mineralogical evolution of tonalite gneisses.

The basement has been subdivided into three units based mainly on structural criteria, and the rocks record deformation under decreasing metamorphic conditions. A high-temperature foliation, formed under amphibolite-facies conditions, is observed in amphibolite and tonalite gneiss. This foliation is well developed and steeply inclined in basement Unit 1 and is less intense and moderately inclined in Unit 3, except in the deepest part where the foliation intensity increases again. Chlorite-rich breccias, microbreccias, and fault gouge were formed under lower greenschist-facies conditions and during cooling to surface conditions; these form the dominant rock types in Unit 2. The formation of ubiquitous epidote, chlorite, and calcite veins accompanied the brittle deformation that formed the breccias.

Sedimentary Rocks

Hole 1067A passed through 116 m of Eocene and Paleocene sedimentary rocks interpreted as mainly post-rift contourites, turbidites, and hemipelagites (see “Lithostratigraphy” section, this chapter). We took 137 measurements on the cores of true dip in the core reference frame (Tables 9, 10 on CD-ROM, back pocket, this volume). Dips are dominantly between 0° and 20° with a mean of 11.5° and a standard deviation of 5.3°, with no obvious trend with increasing depth (Fig.

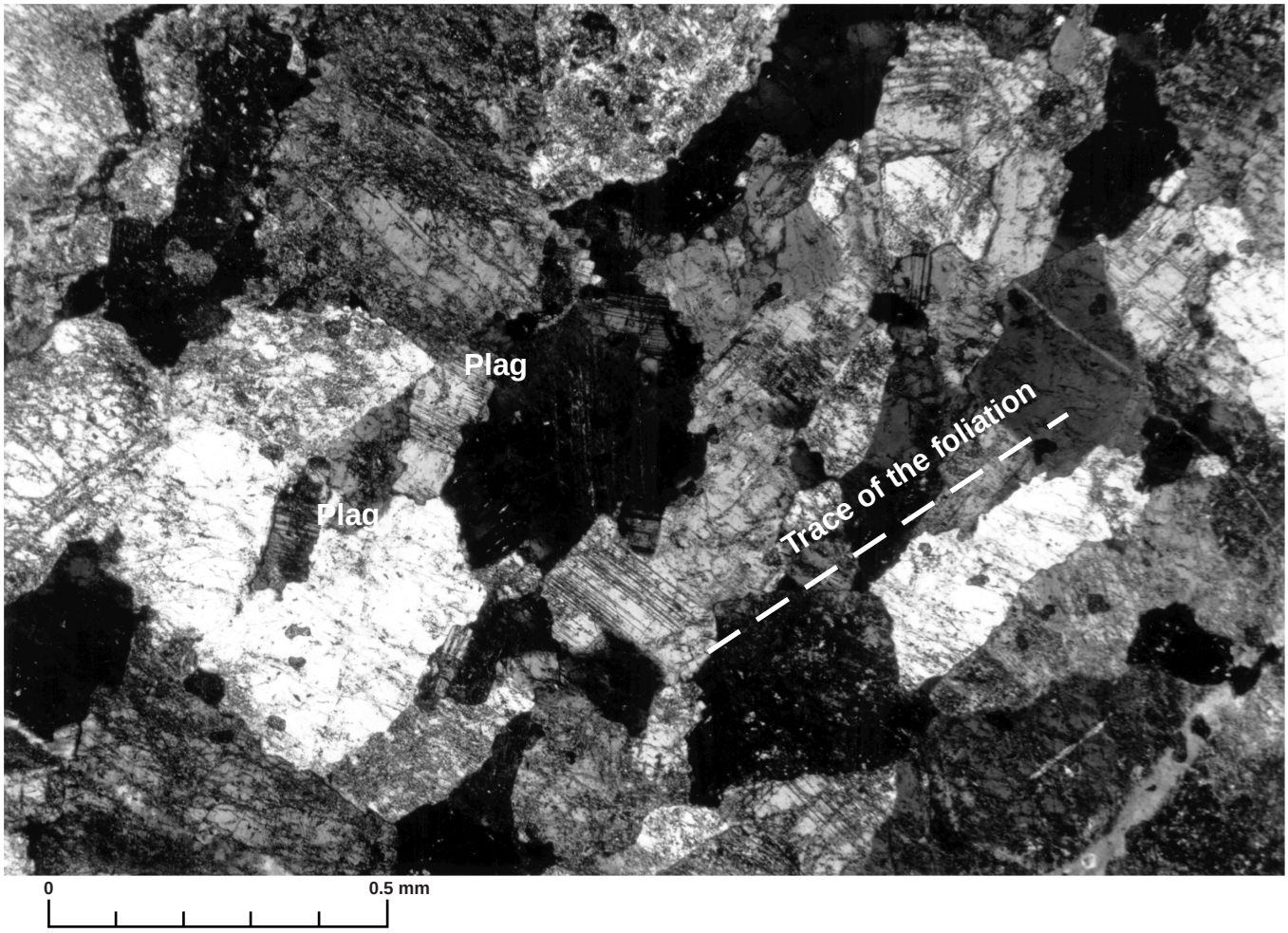

Figure 34. Photomicrograph of Unit 3 meta-anorthosite (Sample 173-1067A-23R-5 [Piece 4, 33–36 cm]). See Table 7 for mineral abbreviations.

STAGE	MAGMATIC	METAMORPHIC I	METAMORPHIC II	FRACTURES
Thermal Conditions	Cpx or Hbl Gabbro	Amphibolite Facies	Greenschist Facies	Very Low Grade
Amphibolite	Igneous Texture	Recrystallization Foliation/Folding	Foliation/Breccia Epi + Chl Veins	Calcite Veins
Tonalite Gneiss	Igneous Texture	Recrystallization Foliation/Folding	Foliation/Breccia Epi + Chl Veins	Calcite Veins
Meta-anorthosite	Occurrence ?	Foliation ?	Foliation/Breccia	Calcite Veins

Time

Figure 35. Timing and conditions of emplacement for the amphibolite, tonalite gneiss and meta-anorthosite.

42). No evidence for ductile or brittle deformation is visible in the cores. The dip of the bedding may be explained by tectonic tilting of the sequence after its deposition, by originally nonhorizontal bedding caused by bed-form migration (see Wilson et al., 1996), or by lateral differences in sediment compaction on and off the basement high. Whereas no significant tilt of reflectors is visible at this site on an east-west profile (see Fig. 10, "Introduction" chapter, this volume), there is some evidence of local flexure affecting the deeper part of the sediments on a nearby north-south profile (Fig. 5). Possible Viscous Remanent Magnetization (VRM) components of sedimentary samples were used to reconstruct the orientation of the bedding in the geographical reference frame (see "Paleomagnetism" section, "Explanatory Notes" chapter, this volume). This was done by rotating the orientation measured in the core reference frame around a vertical axis by the angle of declination of the VRM. The results indicate that the dip direction of the bedding in Hole 1067A varies between northwest and northeast (Table 9 on CD-ROM, back pocket, this volume).

A comparison of bedding planes measured on the cores and on digital images acquired using the DMT CoreScan system was conducted on split Core 173-1067A-10R to test the reliability of automated image processing (see "Core Imaging" section, "Explanatory Notes" chapter, this volume). Before the core was split, the pieces of this core were reoriented in the opened core liner in such a way that the dip direction in the individual pieces was uniform and parallel to the eventual split surface. Binary images were created to identify the alternating color sequence of upward-darkening red-brown (calcareous siltstone/sandstone, calcareous silty sandstone, and claystone) and light gray (calcareous siltstone/sandstones) beds in the core (see "Lithostratigraphy" section, this chapter). One hundred thirty-eight calcareous siltstone/sandstone beds were identified and measured on the core (Table 11 on CD-ROM, back pocket, this volume), compared to 126 measurements on the processed image. Initial analysis of dip data obtained from image analysis shows a good correlation

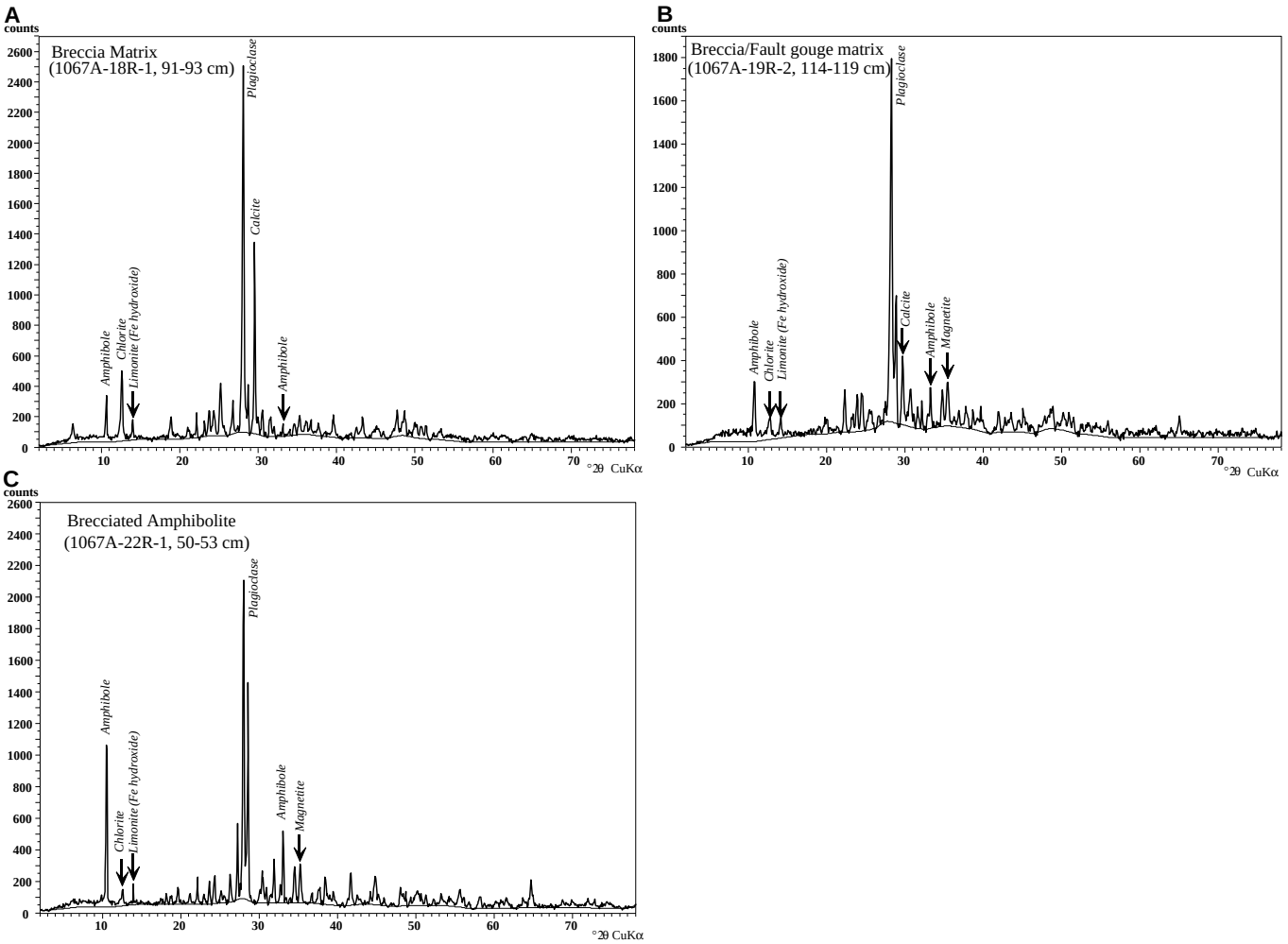

Figure 36. °2θ CuK_{α} vs. intensity X-ray diffraction patterns for (**A**) breccia matrix (Sample 173-1067A-18R-1, 91–93 cm), (**B**) breccia/fault gouge matrix (Sample 173-1067A-19R-2, 114–119 cm), and (**C**) brecciated amphibolite (Sample 173-1067A-22R-1, 50–53 cm).

with the measurements on core (Fig. 43). Median dip angles for core and image measurements are 10° and 11.65°, respectively. The mean dip values differ to a greater extent, being 9.37° and 15.41° for core and image measurements, respectively. Such a discrepancy is probably an artifact of fitting an ellipse to the images of sandstone beds, where the thickness approaches the width of the core, or from measurements made on rotated pieces.

Comparison of the two techniques suggests that automated image processing can quickly identify the general trend of core apparent dips. Future work postcruise to interactively remove erroneous data points based on image analysis will provide detailed and continuous plots of dips of identifiable lithologic beds from the images.

Basement Rocks

The basement rocks in Hole 1067A were subdivided into three units, based mainly on structural criteria (see "Igneous and Metamorphic Petrology" section, this chapter). Unit 1 exhibits a strongly developed, steeply dipping foliation (Fig. 44; Table 12) and moderate brecciation. The same foliation occurs in Unit 2 but usually is overprinted there by extensive brecciation. Unit 3 shows weaker and less pervasive (except in the deepest part) foliation with shallower dip (Fig. 44; Table 12) and only minor brittle deformation.

Foliation in Amphibolite

The foliation in the amphibolite, defined in the core by the alignment of elongate amphibole and plagioclase grains and aggregates (see Fig. 22, "Igneous and Metamorphic Petrology" section), is present in all three units, but it is generally weaker in Unit 3 where features interpreted as relict igneous textures are preserved in many samples (see below, and "Igneous and Metamorphic Petrology" section, this chapter).

In Units 1 and 2, the mineral assemblages in the amphibolites (blue-green to green-brown amphibole plus andesine) are typical of basic rocks metamorphosed in the lower amphibolite facies (see "Igneous and Metamorphic Petrology" section, this chapter). The foliation in the amphibolite is strongly developed, and in thin section is defined by the alignment of elongate amphibole, sphene, and, in some cases, individual plagioclase porphyroclasts. Sporadic evidence for plastic behavior of amphibole includes undulose extinction in some grains and aggregates. In most thin sections, plagioclase grains with lobate grain boundaries form interconnected layers and lens-shaped aggregates aligned with the foliation (see Fig. 27, "Igneous and Metamorphic Petrology" section, this chapter). Such aggregates, in which the neoblasts are in the range 0.1–0.4 mm, are interpreted as having recrystallized from larger grains. In Sample 173-

Table 8. Major and trace element whole-rock compositions and CIPW norms for Hole 1067A amphibolite, tonalite gneiss, and breccia matrix.

	Unit 1			Unit 2			Unit 3			
Rock name:	Foliated amphibolite	Tonalite gneiss	Amphibolite	Breccia matrix	Breccia matrix	Amphibolite	Amphibolite	Amphibolite	Foliated amphibolite	Amphibolite
Core, section:	14R-1	15R-1	16R-1	18R-1	19R-2	20R-1	22R-2	23R-2	23R-2	23R-3
Interval (cm):	22-26	0-4	5-9	91-93	114-116	80-83	43-47	80-83	107-111	19-23
Piece:	4	1	1B	15	6B	5B	3	1C	1D	1A
Depth (mbsf):	764.02	773.40	784.18	802.81	814.07	821.90	842.09	852.30	852.57	853.04
SiO_2 (wt%)	48.44	76.30	52.28	47.22	51.97	48.92	53.60	49.71	50.30	41.83
TiO_2	3.38	0.34	2.17	1.77	1.87	2.01	2.00	2.37	2.55	3.15
Al_2O_3	15.04	11.33	12.72	16.12	15.89	14.43	13.99	13.98	13.15	14.10
Fe_2O_3	16.11	2.14	13.31	11.75	9.52	14.43	12.46	13.95	14.59	20.64
MnO	0.27	0.02	0.20	0.36	0.17	0.32	0.25	0.27	0.26	0.32
MgO	6.52	1.13	6.07	5.08	5.26	7.44	6.09	7.04	7.13	10.59
CaO	7.82	0.75	9.45	13.17	9.40	8.06	6.54	8.48	8.60	6.69
Na_2O	2.72	5.81	2.62	4.27	4.30	3.51	5.12	3.83	3.84	1.90
K_2O	0.78	0.21	1.09	1.36	0.75	0.49	0.28	0.37	0.45	0.29
P_2O_5	0.40	0.04	0.29	0.31	0.22	0.26	0.20	0.32	0.36	0.07
Total	101.45	98.07	100.18	101.41	99.33	99.83	100.51	100.31	101.20	99.58
FeO^*/MgO	2.22	1.65	1.97	2.07	1.63	1.75	1.84	1.78	1.84	1.75
Mg/(Mg+.86 Fe)	50.9	58.2	53.9	52.6	58.6	56.9	55.6	56.4	55.6	56.8
LOI (%)	2.94	0.50	1.28	10.13	5.70	1.44	1.15	0.96	1.00	3.24
QZ	—	37.49	3.39	—	—	—	—	—	—	—
CO	—	0.28	—	—	—	—	—	—	—	—
OR	4.61	1.24	6.44	8.04	4.43	2.90	1.65	2.19	2.66	1.71
AB	23.02	49.16	22.17	9.20	36.39	29.70	43.32	32.41	32.49	16.08
AN	26.52	3.46	19.73	20.80	21.84	22.17	14.36	19.86	17.32	29.09
NE	—	—	—	14.59	—	—	—	—	—	—
DI	7.99	—	20.85	35.21	19.13	13.27	13.82	16.55	18.93	3.00
HY	24.86	5.09	18.98	—	3.62	9.85	13.22	8.65	9.43	11.06
OL	2.49	—	—	6.10	7.13	13.39	6.28	11.39	10.50	26.53
MT	3.28	0.43	2.70	2.38	1.93	2.93	2.52	2.83	2.96	4.19
IL	6.42	0.65	4.12	3.36	3.55	3.82	3.80	4.50	4.84	5.98
AP	0.95	0.09	0.69	0.73	0.52	0.62	0.47	0.76	0.85	0.17
Total	100.14	97.89	99.07	100.41	98.53	98.64	99.46	99.13	99.99	97.81
V (ppm)	427	39	408	268	397	407	417	371	357	437
Cr	200	22	267	115	367	312	240	190	224	458
Ni	58	11	52	40	78	80	58	96	90	273
Cu	34	59	17	52	45	184	26	39	34	126
Zn	144	12	110	100	85	125	109	112	118	189
Rb	14	2	21	13	9	8	3	2	6	4
Sr	129	101	118	194	275	139	169	216	153	78
Y	44	23	35	36	28	37	37	48	47	51
Zr	188	140	141	207	137	108	122	196	179	420
Nb	18	9	11	10	9	7	7	13	12	30
Ba	5	116	122	163	46	45	13	0	0	0
Ce	19	56	33	89	41	26	29	42	34	12

Notes: Total iron is reported as Fe_2O_3. CIPW norms were calculated assuming Fe^{2+} = 0.86 Fe total. — = concentration was below detection limit.

1067A-18R-2 (Piece 23, 89–91 cm), for example, elongate undulose plagioclase grains (up to 1 mm long) are in places partly surrounded by granular plagioclase aggregates averaging 0.1 mm grain size and showing triple-point grain boundary intersections (polygonal microstructure). The amphiboles, commonly elongated and anhedral, show a strong preferred orientation of grains. Undulose extinction and kinks are observed in amphiboles, but these may be related to folding that occurred after the main foliation event. Relict igneous microstructures were not observed in Units 1 and 2. Some amphibolites contain minor lenses of dynamically recrystallized quartz. Individual quartz grains in these lenses are lobate, undulose, and elongated. Euhedral grains of sphene, and in some cases apatite, are commonly aligned parallel to the foliation. In some examples (e.g., Sample 173-1067A-14R-1, 17–18 cm) shear bands deflect the main foliation. Retrograde chlorite is present in many amphibolite samples, generally as a replacement for amphibole, and is only locally aligned with the foliation (Sample 173-1067A-14R-1 [Piece 4, 17–18 cm]). In these cases, the chlorite habit suggests that the foliation was reactivated under greenschist facies conditions, or, more likely, chlorite growth was controlled by the aligned amphiboles in a "static" situation.

In Unit 3 the foliation in the amphibolite is generally weaker (except in the deepest cores), heterogeneously distributed, and shallower in dip (Fig. 44). A common microstructure in Unit 3 is characterized by amphibole grains that are aligned with the foliation, and granular aggregates of plagioclase, 0.2–0.5 mm in size, with grain-boundary triple junctions (e.g., Sample 173-1067A-21R-1 [Piece 16, 101–104 cm]). Where the foliation is weak, examples of igneous microstructures are preserved (e.g., ophitic and interstitial microstructures, see Fig. 30, "Igneous and Metamorphic Petrology" section, this chapter). In some samples (e.g., Samples 173-1067A-23R-2 [Piece 1D, 107–111 cm], and 1067A-23R-4 [Piece 8, 74–77 cm]), larger plagioclase grains 0.8–1.5 mm in size may represent relict igneous grains, as the overall textures are very similar to cumulate and subophitic textures commonly observed in gabbros. The deformation was, however, heterogeneously developed in Unit 3, and in Samples 173-1067A-20R-1, 80–83 cm, 23R-4, 1–4 cm, and 20R-1, 70–72 cm, the plagioclase occurs as undulose porphyroclasts enclosed by recrystallized aggregates where the grain size is as small as 0.01 mm. Intensely foliated amphibolites are observed in the lowermost two sections (Sections 173-1067A-23R-4 and 23R-5).

Foliation in Tonalite Gneiss

The tonalite gneiss is typically fine grained, and the foliation is difficult to discern in hand specimen. Some tonalite gneiss veins show augen microstructures (e.g., Sample 1067A-14R-1 [Piece 3, 8–15 cm]) whereas others show apparent igneous features in hand specimen (e.g., Sample 1067A-15R-1 [Piece 1, 0–4 cm]). Contacts be-

tween tonalite gneiss and amphibolite can be seen in Cores 173-1067A-14R, 15R, 16R, and 17R (see Fig. 24, "Igneous and Metamorphic Petrology" section, this chapter). These contacts are parallel to the foliation in both amphibolite and tonalite gneiss (Cores 173-1067A-14R to 17R). Such observations may mean that the tonalite veins were intruded parallel to the foliation during deformation, or, alternatively, that the tonalites pre-dated the foliation but the veins

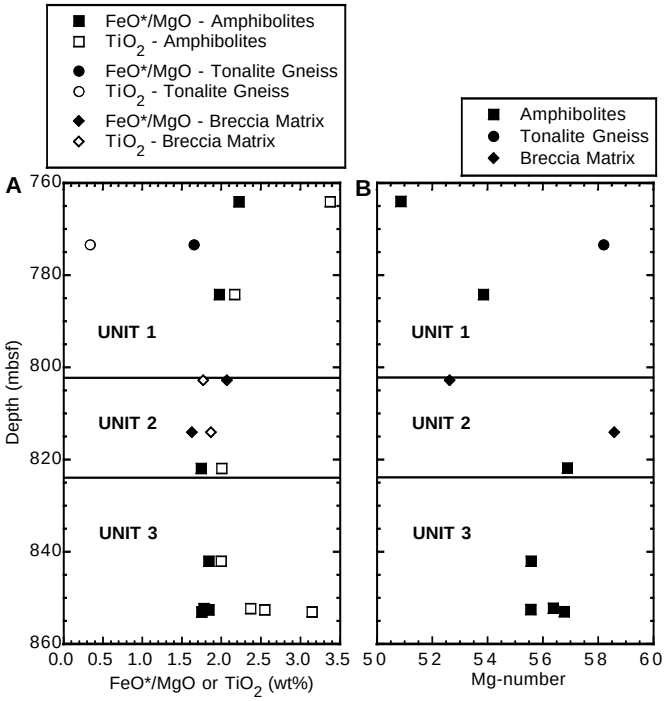

Figure 37. **A.** FeO*/MgO or TiO_2 (wt%) vs. depth (mbsf) diagram for samples from Site 1067. **B.** Mg-number vs. depth (mbsf) diagram.

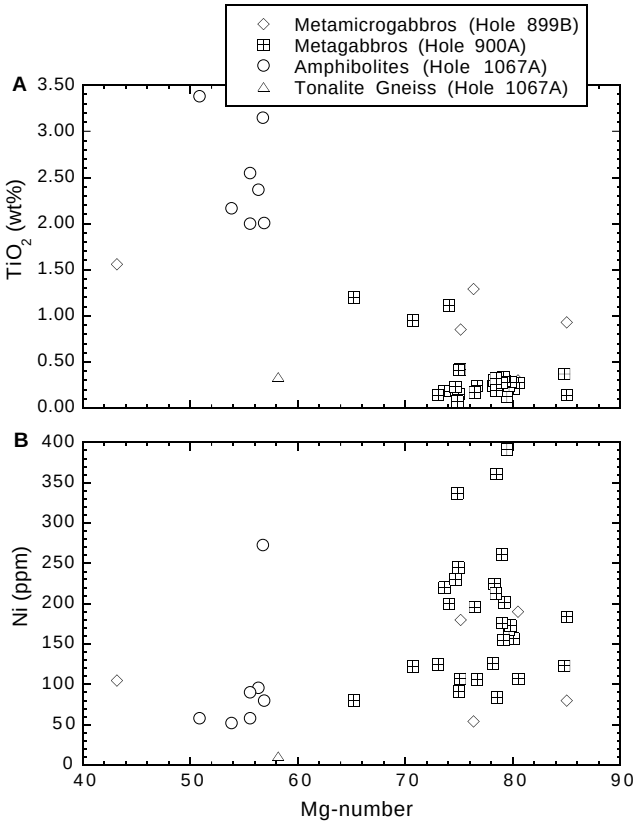

Figure 39. (**A**) Mg-number vs. TiO_2 (wt%) and (**B**) Mg-number vs. Ni (ppm) variation diagrams for the Site 1067 amphibolites and tonalite gneiss. Also shown are the data from Site 899 metamicrogabbros and Site 900 metagabbros for comparison. Data from Sawyer, Whitmarsh, Klaus, et al. (1994); Cornen et al. (1996); and Seifert et al. (1996).

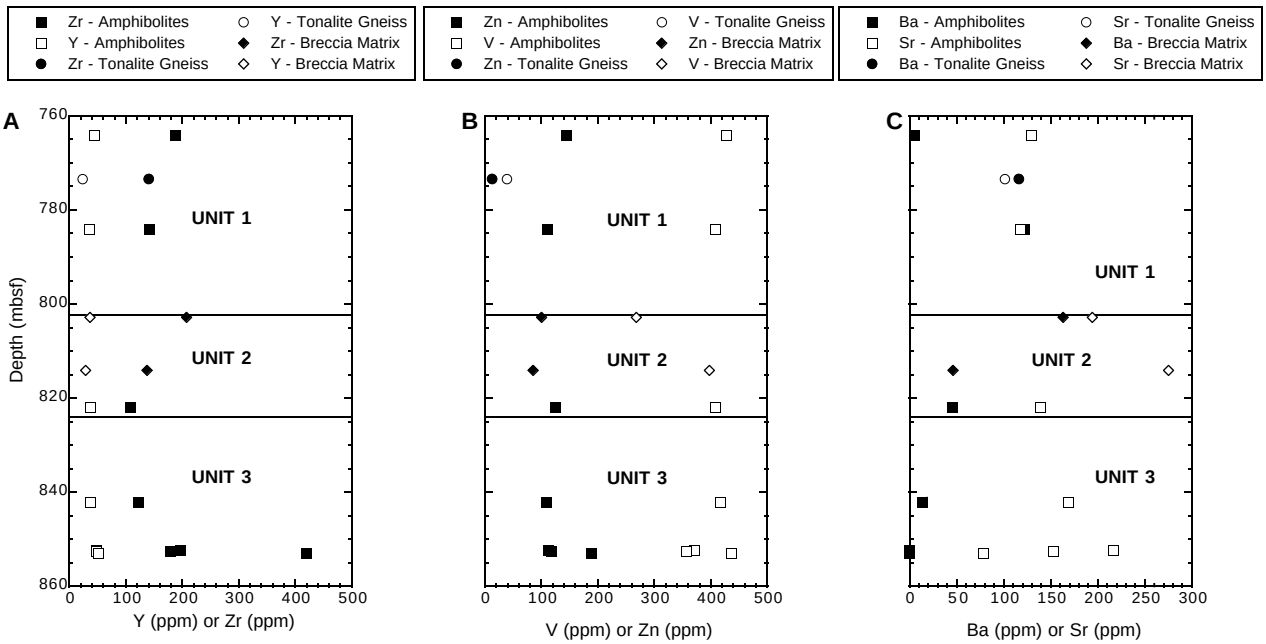

Figure 38. **A.** Y (ppm) or Zr (ppm) vs. depth (mbsf). **B.** V (ppm) or Zn (ppm) vs. depth (mbsf). **C.** Ba (ppm) or Sr (ppm) vs. depth (mbsf) diagrams for Site 1067 samples.

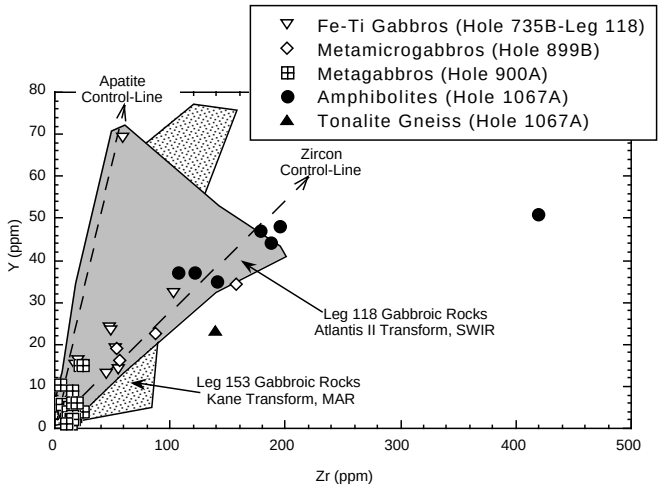

Figure 40. Zr (ppm) vs. Y (ppm) variation diagram. The evolved nature of the Site 1067 amphibolites is shown in relation to the Site 899 metamicrogabbros and Site 900 metagabbros. The fields of oceanic gabbro compositions from the Southwest Indian Ridge (Leg 118) and Mid-Atlantic Ridge (Leg 153) are displayed. Also shown are the approximate paths for apatite and zircon accumulation, based on Y compatibility in apatite (Deer et al., 1993) and Zr and Y compatibilities in zircon (Deer et al., 1982). Data from Robinson, Von Herzen, Adamson, et al. (1989); Sawyer, Whitmarsh, Klaus, et al. (1994); Cannat, Karson, Miller, et al., (1995); and Cornen et al. (1996).

happened to be oriented subparallel to the plane of subsequent overprinting foliation.

Under the microscope, the plagioclase occurs as porphyroclasts with undulose extinction. Igneous biotite and quartz are only rarely preserved within primary plagioclase porphyroclasts. The porphyroclasts are set in a matrix of quartz and phyllosilicates. Aggregates of fine-grained quartz wrap around plagioclase, thereby forming a micro-augen structure (see Fig. 32, "Igneous and Metamorphic Petrology" section, this chapter). Quartz occurs as variably strained, recovered, and recrystallized grains. Larger, relict quartz porphyroclasts characterized by undulatory extinction are surrounded by recrystallized smaller neoblasts with a preferred grain-shape and crystallographic orientation. The recrystallized grains are oriented with their long axes oblique to the main foliation, indicating a simple-shear component of deformation. In some tonalite samples, thin layers of chlorite are aligned with the foliation, and Sample 1067A-16R-2 (Piece 1B, 5–9 cm) shows elongate aggregates of epidote grains aligned parallel to the foliation. It is possible that the aligned chlorite represents reactivation of the foliation under greenschist facies conditions, but more likely it replaced previously aligned biotite under static conditions.

Foliation in Anorthosite

In Unit 3, the anorthosite veins are subparallel to the foliation where it is more strongly developed (e.g., Sample 173-1067A-19R-1 [Piece 5, 41–44 cm]). However, where the foliation is weaker, irregular patches of anorthosite merge into the enclosing amphibolite. Anorthosite patches and veins show microstructures that are very similar to those in the enclosing amphibolites, namely coarser undulose plagioclase grains partly surrounded by finer recrystallized aggregates, and alignment of amphibole in the more strongly foliated examples. In Sample 173-1067A-22R-3 (Piece 1, 43–47 cm), for example, coarser plagioclase porphyroclasts up to 1.5 mm in size are surrounded by granular matrix plagioclase, averaging 0.8 mm in anorthosite and 0.3 mm in amphibolite, interpreted as dynamically recrystallized

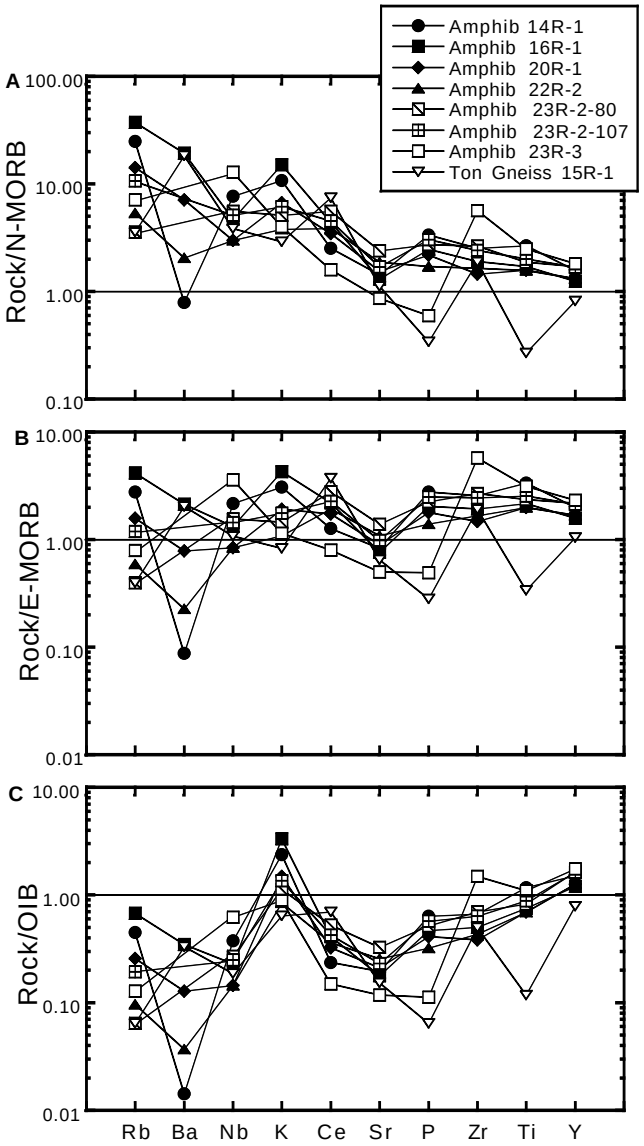

Figure 41. Extended trace element plots of Site 1067 amphibolites and one tonalite gneiss normalized to (**A**) N-MORB, (**B**) E-MORB, and (**C**) OIB. Normalization values are from Sun and McDonough (1989).

aggregates. In Sample 173-1067A-23R-5 (Piece 4, 33–36 cm), the foliation in the anorthosite is defined by aligned amphibole and amphibole aggregates, whereas the plagioclase is anhedral to subhedral and inequigranular (mainly 1.6- to 8-mm grain size). Whereas some grains are almost certainly relict igneous features, patches of plagioclase showing triple point junctions are interpreted as having formed by dynamic recrystallization. In Sample 173-1067A-19R-1 (Piece 5C, 41–44 cm), plagioclase grains greater than 1 cm in size show recrystallization along grain boundaries and microfractures to polygonal mosaics with grains averaging 0.4 mm (Fig. 45). On the basis of their microstructures, the anorthosite veins and patches are interpreted as having had a structural history similar to that of the amphibolites, with minor differences in foliation intensity and degree of recrystallization of plagioclase being possibly a function of lithologic differences. In amphibolites, diffusional processes (e.g., nucleation and preferred growth of amphibole as a new ferromagnesian phase) as well as physical processes (dynamic recrystallization) were in-

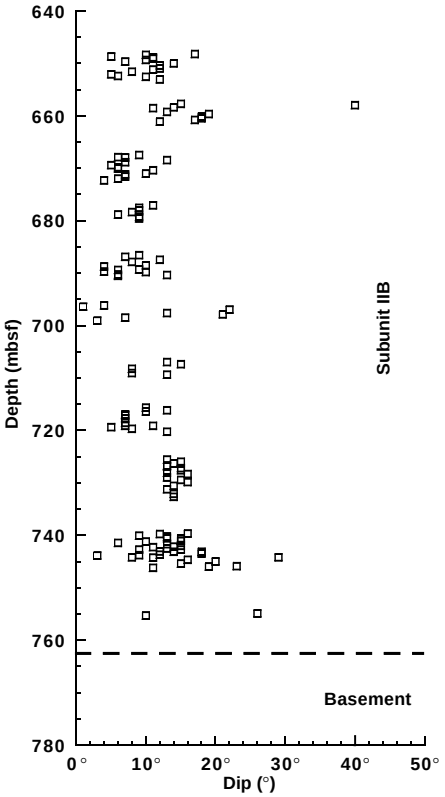

Figure 42. Dip of bedding vs. depth for sediments in Subunit IIB.

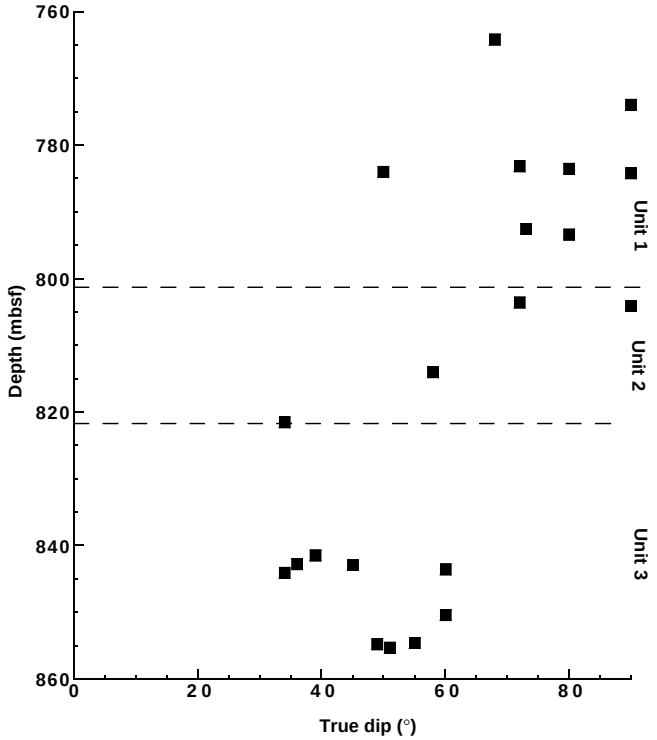

Figure 44. Dip of foliation vs. depth for the basement Units 1, 2, and 3.

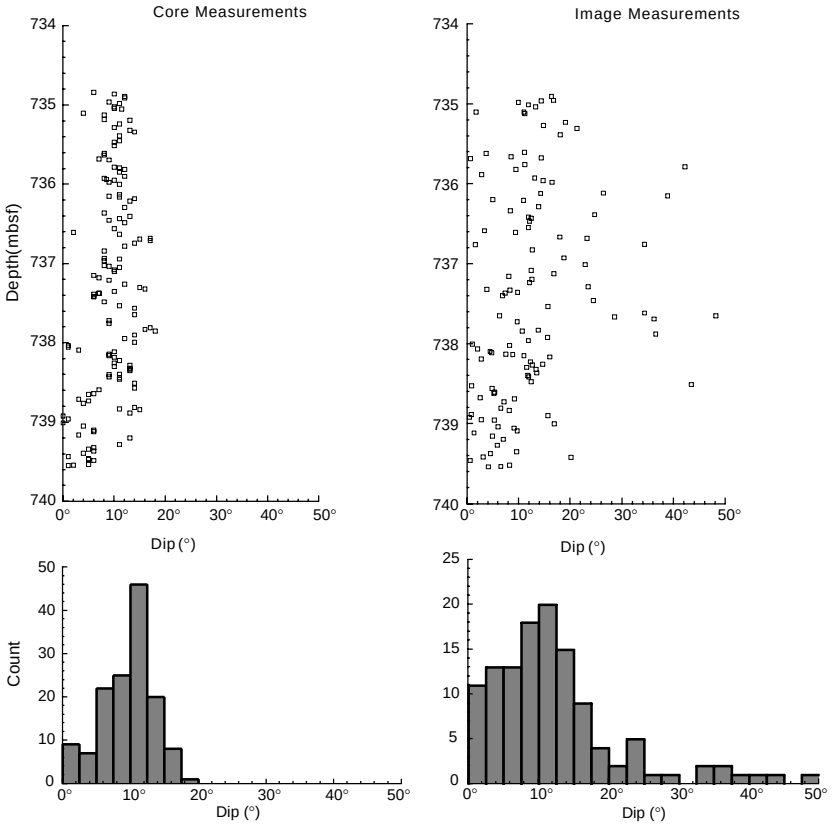

Figure 43. Dip of bedding vs. depth and histograms of dip from measurements made on the core and from binary processed images of Core 173-1067A-10R.

Table 12. Structural measurements from the basement Units 1, 2, and 3 of Hole 1067A.

Core, section, interval	Depth (mbsf)	Feature	Orientation		Comments
			Dip (°)	Direction (°)	
173-1067A-					
14R-1 (Piece 6, 32-52 cm)	764.2	Foliation	68	090	
15R-1 (Piece 8, 36-47 cm)	773.8	Fault	90	090	Lithologic contact
15R-1 (Piece 8, 36-47 cm)	773.9	Lineation	0	090	Lineation type not defined
15R-1 (Piece 11, 54-64 cm)	774.0	Foliation	90	090	
16R-1 (Piece 6, 26-34 cm)	783.2	Foliation	72	098	
16R-1 (Piece 11, 65-80 cm)	783.6	Foliation	80	092	
16R-1 (Piece 15, 99-113 cm)	783.9	Fold axial plane	62	097	Folded foliation
16R-1 (Piece 15, 99-113 cm)	783.9	Fold axis	20	180	Folded foliation
16R-2 (Piece 1, 0-36 cm)	784.0	Foliation	50	090	
16R-2 (Piece 1, 0-36 cm)	784.2	Foliation	90	090	
17R-1 (Piece 3, 15-25 cm)	792.6	Foliation	73	087	
17R-1 (Piece 10, 60-72 cm)	793.0	Fold axial plane	62	296	Folded foliation
17R-1 (Piece 10, 60-72 cm)	793.0	Fold axis	30	009	Folded foliation
17R-1 (Piece 15, 100-109 cm)	793.4	Foliation	80	090	
18R-1 (Piece 9, 46-61 cm)	802.4	Fault plane	6	090	
18R-2 (Piece 4, 21-40 cm)	803.6	Foliation	72	090	
18R-2 (Piece 7A, 65-105 cm)	804.1	Foliation	90	090	
19R-1 (Piece 5, 30-50 cm)	811.9	Fault	48	046	
19R-1 (Piece 7A, 51-85 cm)	812.2	Fault	59	090	
19R-1 (Piece 7A, 51-85 cm)	812.2	Slickensides	59	090	
19R-1 (Piece 7A, 51-85 cm)	812.3	Fault	70	090	
19R-1 (Piece 7A, 51-85 cm)	812.3	Slicken fibers	67	119	
19R-2 (Piece 6C, 79-140 cm)	814.0	Fault	58	109	
19R-2 (Piece 6C, 79-140 cm)	814.0	Slickensides	55	137	
19R-3 (Piece 9, 85-100 cm)	815.4	Fault	62	321	
19R-3 (Piece 9, 85-100 cm)	815.4	Slickensides	36	254	
19R-4 (Piece 1, 0-40 cm)	815.2	Fault	70	270	
19R-4 (Piece 1, 0-40 cm)	815.2	Slickensides	12	355	
20R-1 (Piece 4, 36-56 cm)	821.5	Foliation	34	270	
20R-1 (Piece 5B, 36-56 cm)	821.6	Fault	50	270	
20R-1 (Piece 5B, 36-56 cm)	821.6	Slickensides	26	339	
22R-1 (Piece 7, 60-78 cm)	841.1	Calcite vein	66	090	
22R-1 (Piece 7, 60-78 cm)	841.2	Calcite vein	45	270	
22R-1 (Piece 8, 78-110 cm)	841.3	Calcite vein	66	270	
22R-1 (Piece 8, 78-110 cm)	841.4	Calcite vein	90	090	
22R-1 (Piece 8, 78-110 cm)	841.5	Foliation	39	246	
22R-2 (Piece 1A, 0-32 cm)	842.0	Calcite vein	63	270	
22R-2 (Piece 3, 40-80 cm)	842.5	Calcite vein	76	083	
22R-2 (Piece 4, 80-100 cm)	842.8	Foliation	36	062	
22R-2 (Piece 4, 80-100 cm)	842.9	Foliation	45	065	
22R-2 (Piece 9, 131-147 cm)	843.3	Calcite vein	23	037	
22R-3 (Piece 1, 0-30 cm)	843.6	Foliation	60	270	
22R-3 (Piece 6, 61-87 cm)	844.1	Foliation	34	270	
23R-1 (Piece 1, 0-12 cm)	850.1	Fault	65	270	
23R-1 (Piece 1, 0-12 cm)	850.1	Slickensides	61	235	
23R-1 (Piece 2A, 12-45 cm)	850.3	Fault	66	270	
23R-1 (Piece 2A, 12-45 cm)	850.4	Fault	51	213	
23R-1 (Piece 2A, 12-45 cm)	850.4	Magmatic vein	46	215	
23R-1 (Piece 2A, 12-45 cm)	850.4	Foliation	60	270	
23R-1 (Piece 2B, 45-71 cm)	850.5	Epidote vein	24	270	
23R-1 (Piece 2B, 45-71 cm)	850.5	Magmatic vein	26	289	
23R-1 (Piece 2B, 45-71 cm)	850.6	Epidote vein	0	005	
23R-2 (Piece 1A, 0-28 cm)	851.6	Fault	10	019	
23R-2 (Piece 2A, 28-61 cm)	851.9	Fault	36	346	
23R-3 (Piece 1A, 0-50 cm)	853.3	Fault	46	177	
23R-3 (Piece 1A, 0-50 cm)	853.3	Slickensides	49	150	
23R-3 (Piece 1B, 50-67 cm)	853.6	Fault	39	189	
23R-3 (Piece 1B, 50-67 cm)	853.6	Slickensides	38	202	
23R-3 (Piece 3A, 85-115 cm)	854.0	Fault	38	008	
23R-3 (Piece 3A, 85-115 cm)	853.0	Slickensides	38	005	
23R-4 (Piece 1, 0-21 cm)	854.6	Foliation	55	270	
23R-4 (Piece 1, 0-21 cm)	854.6	Epidote vein	11	000	
23R-4 (Piece 3, 29-45 cm)	854.8	Foliation	49	090	
23R-4 (Piece 3, 29-45 cm)	854.8	Magmatic vein	40	090	
23R-4 (Piece 8, 74-85 cm)	855.3	Foliation	51	270	
23R-4 (Piece 10, 92-102 cm)	855.5	Calcite vein	72	270	
23R-4 (Piece 10, 92-102 cm)	855.5	Magmatic vein	45	270	

Note: Orientation is in the core reference frame.

volved, so that amphibolites would not be expected to show the same microstructural development as plagioclase-dominated anorthosites. Nevertheless, structural and microstructural criteria alone cannot distinguish whether the anorthosites formed before or during the development of the foliation. However, as igneous anorthosites are common in many layered gabbro complexes, and anorthosites and leucogabbros with typical cumulate textures are present in breccia clasts in Hole 1068A, the anorthosites in Hole 1067A are more likely to be igneous than syndeformational.

Folds

Folds were observed only in Unit 1. A tight, vergent fold in interval 173-1067A-16R-1, 99–112 cm, has an axis plunging 20° and a steeply inclined axial plane (Fig. 46). The fold deforms the foliation of the amphibolite and a foliation-parallel tonalite layer. The folding did not lead to the formation of a new axial-plane foliation. Quartz in the fold hinge accommodated the folding by dynamic recrystallization indicating that the fold formed at a still elevated temperature

Figure 45. Photomicrograph of deformed anorthosite from Sample 173-1067A-19R-1 (Piece 5C, 41–44 cm). Crossed nicols.

(>300°C). Retrogressive formation of chlorite and albite is associated with the fold. The fold is crosscut by younger epidote veins. Another fold, with a more open shape (interlimb angle 100°) and a shallowly inclined axial plane, occurs in interval 173-1067A-17R-1, 60–72 cm. Open kink folds are also present in Unit 1, generally with shallow-dipping axial planes. Epidote veins commonly occur along these kinks.

Veining, Brecciation, and Fluid-Rock Interaction

The basement cores of Hole 1067A exhibit evidence of pervasive brittle deformation associated with fluid-rock interaction. Since these are intimately related processes, the relevant observations will be described together.

Retrograde Veining and Wall Rock Alterations

Evidence for retrograde fluid-rock interaction is ubiquitous throughout the cores, in the form of veins and associated wall rock alteration that, respectively, crosscut and overprint the above-described foliation and subsequent folding. In general, the veining and alteration can be related to two discrete phases of fluid-rock interaction.

Phase 1 is characterized by abundant, 1- to 3-mm-thick veins of epidote, chlorite, iron oxide, and rare calcite that crosscut foliation and folds in the tonalites and the amphibolites. Epidote veins commonly occur as anastomosing bundles, which in thin section appear as complex networks of microfractures or grain boundary channels, and which grade into more pervasive epidotization and cataclasis of the wall rock. Chlorite veins are common and localize minor shearing, although it is unclear whether chloritization initiated shearing or vice versa.

In the amphibolites, wall rock amphiboles have commonly retrogressed to chlorite (Fig. 47) and, in a sample from interval 173-1067A-18R-2, 89–91 cm, to chlorite + calcite, suggesting carbonation by the greenschist facies reaction: amphibole + epidote + CO_2 + H_2O = chlorite + calcite + quartz. In the uppermost part of Unit 1, this retrogression is pervasive, and as much as 30% of modal amphibole is replaced by chlorite along grain boundaries, cleavage planes, and internal fractures. These textures are clear indicators of sluggish reaction kinetics, as might be expected at lower temperatures and/or

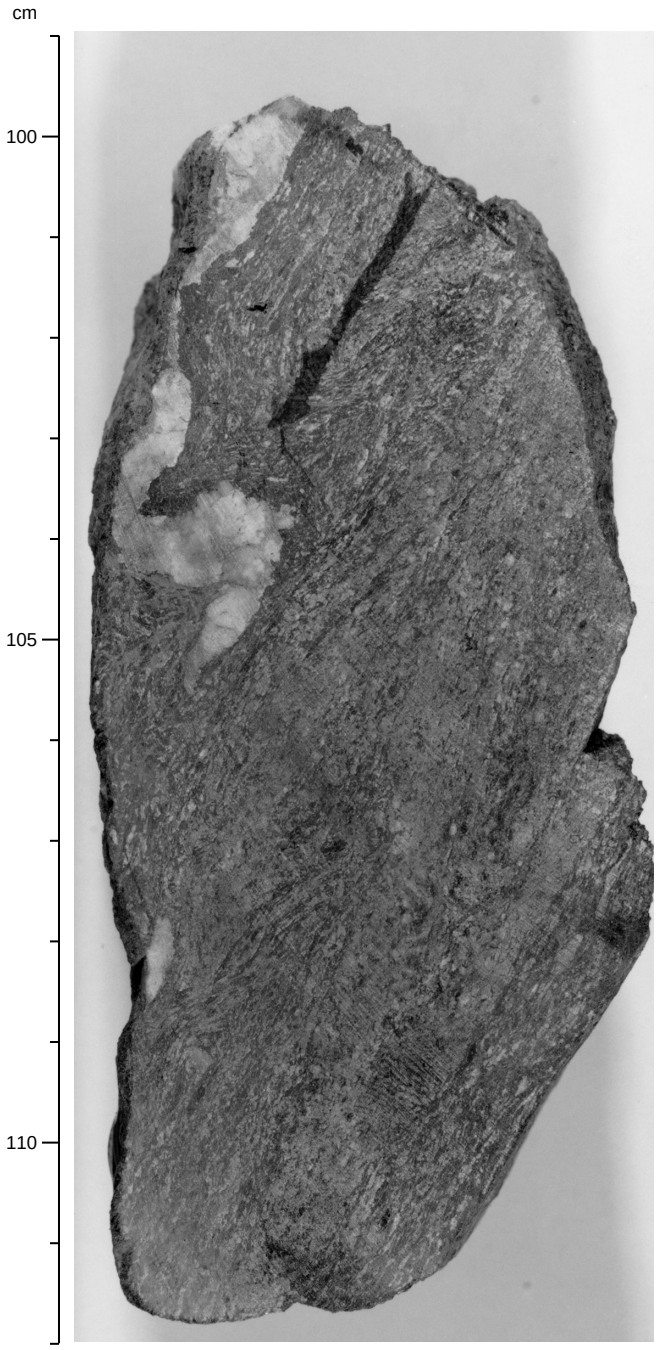

Figure 46. Folded amphibolite with tonalite layer in Unit 1. Interval 173-1067A-16R-1, 99–112 cm.

if fluid flow is less pervasive (e.g., where flow is largely along fractures) and/or if fluid fluxes are small. In Units 2 and 3, this retrogression is largely restricted to the margins of epidote and chlorite veins, suggesting that these are the conduits for the fluids responsible for retrogression.

Phase 2 is characterized by 2- to 5-mm veins of calcite and iron oxide. These veins commonly contain void spaces. They crosscut,

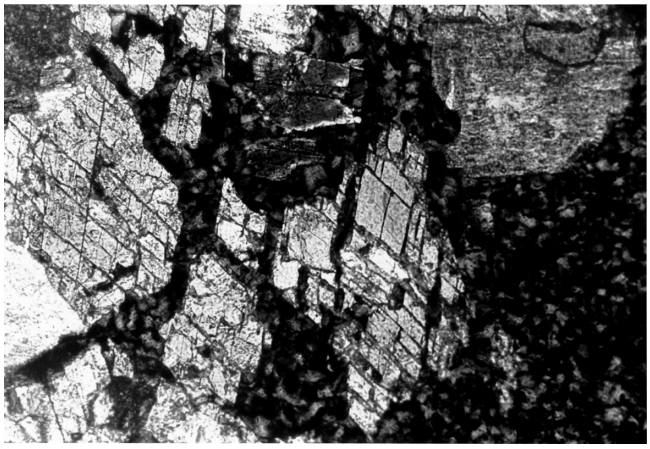

Figure 47. Photomicrograph showing retrogressed amphibole in the wall rock adjacent to a chlorite vein. Dark material is chlorite. Sample 173-1067A-23R-2, 107–111 cm. Crossed nicols.

and therefore postdate, Phase 1 veins (Fig. 48). There is little evidence for associated wall rock alteration, other than for submillimetric seams of iron oxide, which flank the vein margins.

Orientation of Veins

Figure 49 shows the dips of Phase 1 and 2 veins as measured by hand on the cores. Note that the dip of Phase 1 (epidote) veins is moderate to steep in Unit 1 (25° to 65°) and grades to shallow (0° to 25°) in Unit 3. This is similar to the trend of downward shallowing shown by the foliation (see Fig. 44). In contrast to the epidote veins, the dip of Phase 2 (calcite) veins is typically steep (60° to 90°, 9 measurements). Moderately to shallowly dipping calcite veins were only measured in Units 2 and 3 (3 measurements). At any particular depth, calcite veins are generally steeper than epidote veins. "Magmatic veins" (anorthosite pods) in Unit 3 are shallowly to moderately inclined.

Geometric Analysis of Vein Systems Using Core Image Analysis

Digital images of whole-round continuous core pieces (Sections 173-1067A-23R-1 and 23R-2) were acquired using the DMT CoreScan system for the analysis of planar elements. Different vein types and anorthositic pods were identified on the images by comparing them with the core. The dip and azimuth of planar structures in the core reference frame were measured by fitting a sinusoidal function to the images of the structures using the DMT software Corelog. Epidote veins exhibit shallow to moderate dips (Fig. 50) and strike between "NE" and "SE" in the core reference frame (Fig. 51). The dip of anorthositic pods is rather uniform around 40° (Fig. 50). The stereographic representation (Fig. 51) suggests the existence of two subsets of anorthositic pods, dipping "SW" and "N" to "NE". The similar orientations of anorthositic pods and epidote veins suggests a close relationship between these elements. On the other hand, faults and chlorite veins do not show a clear geometric relationship with the epidote veins or the anorthositic pods. The results from core image analysis are in good agreement with structural observations made on cores and thin sections.

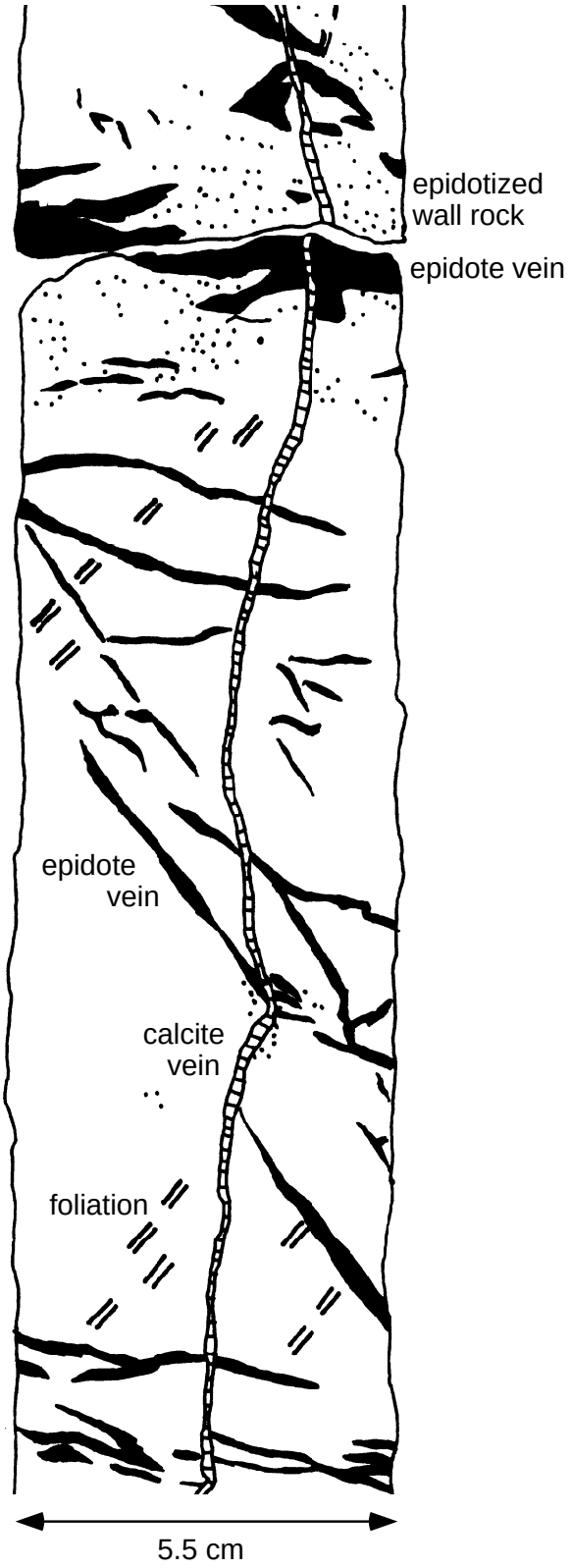

Figure 48. Sketch showing crosscutting relationships between Phase 1 epidote veins, forming two conjugate sets, and a Phase 2 calcite vein. Core 173-1067A-23R-2, 20–47 cm.

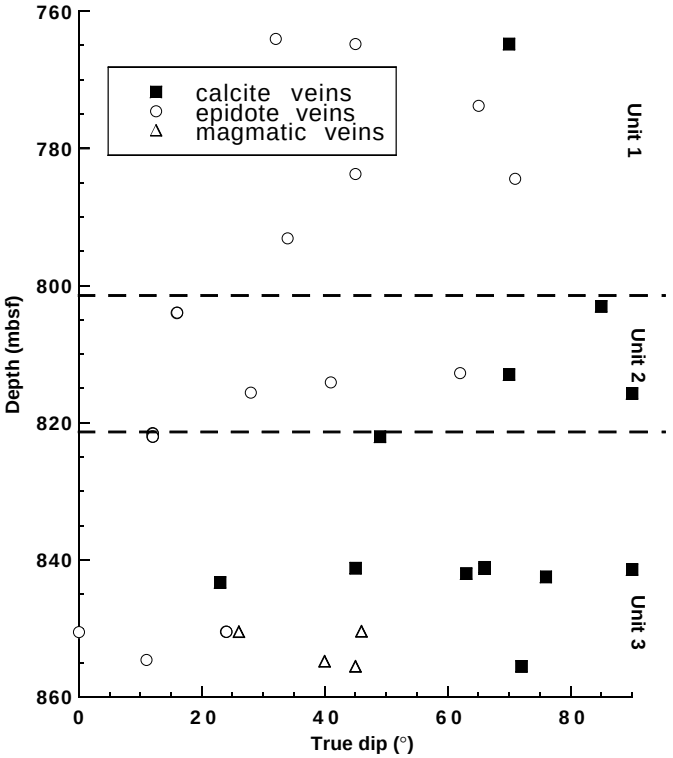

Figure 49. Dip of veins vs. depth for basement Units 1, 2, and 3.

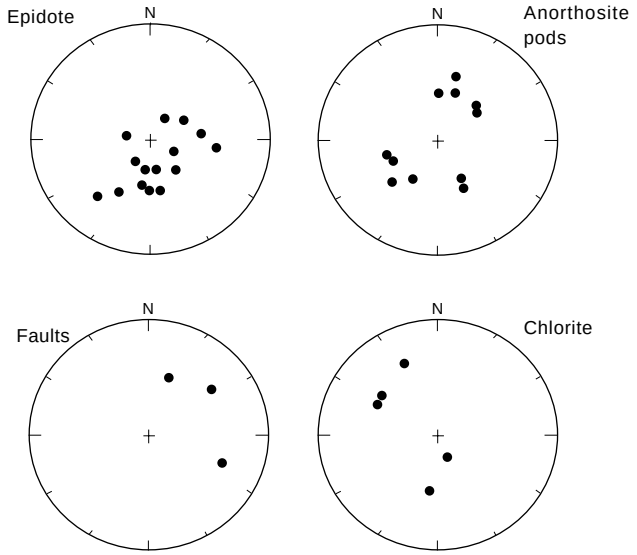

Figure 51. Stereographic representation of faults and epidote and chlorite veins in continuous section of Core 173-1067-23R as determined by core image analysis (lower hemisphere, Schmidt projection, orientation in the core reference frame).

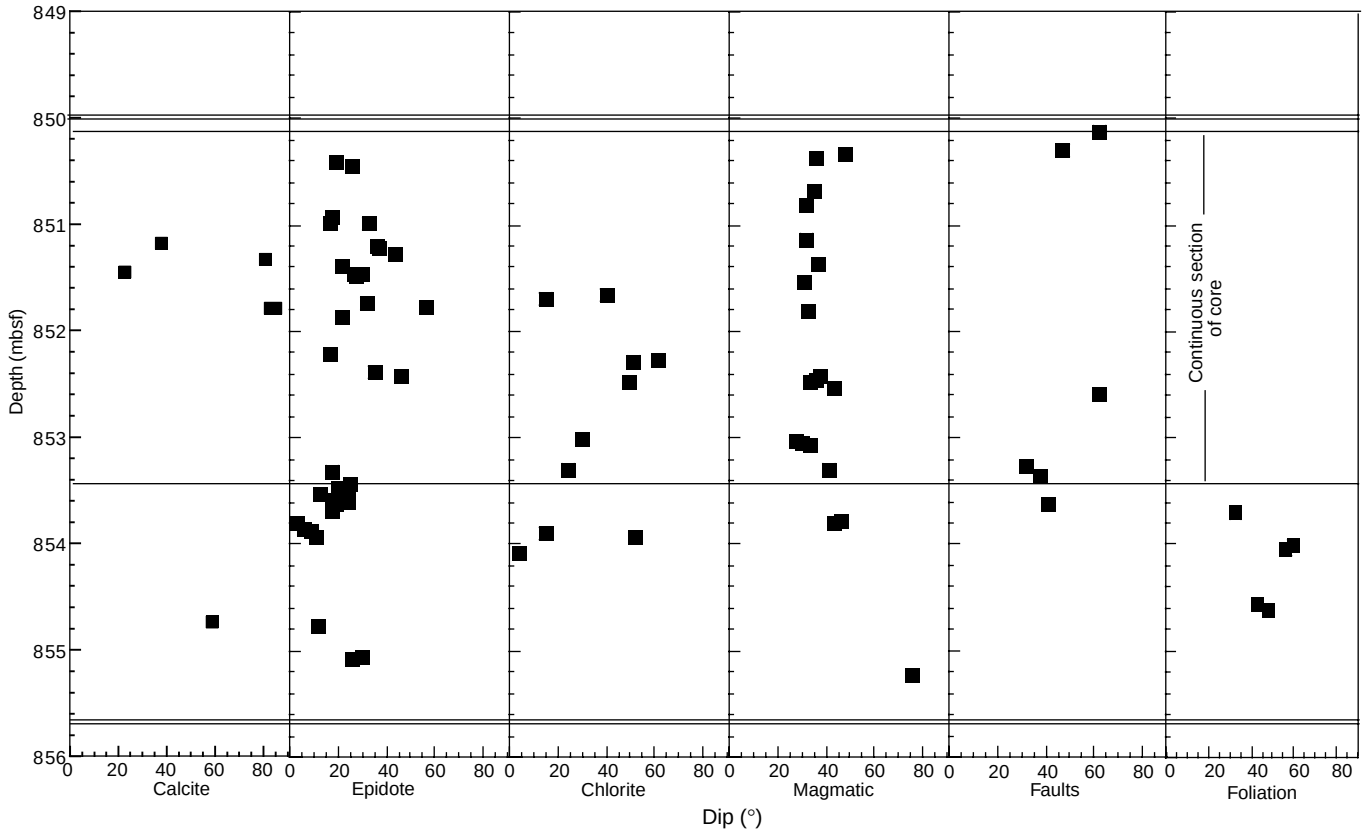

Figure 50. Dips of faults, calcite, epidote, chlorite, and magmatic veins, and foliation in Core 173-1067-23R as determined by core image analysis. The two single horizontal lines bound a continuous section of core.

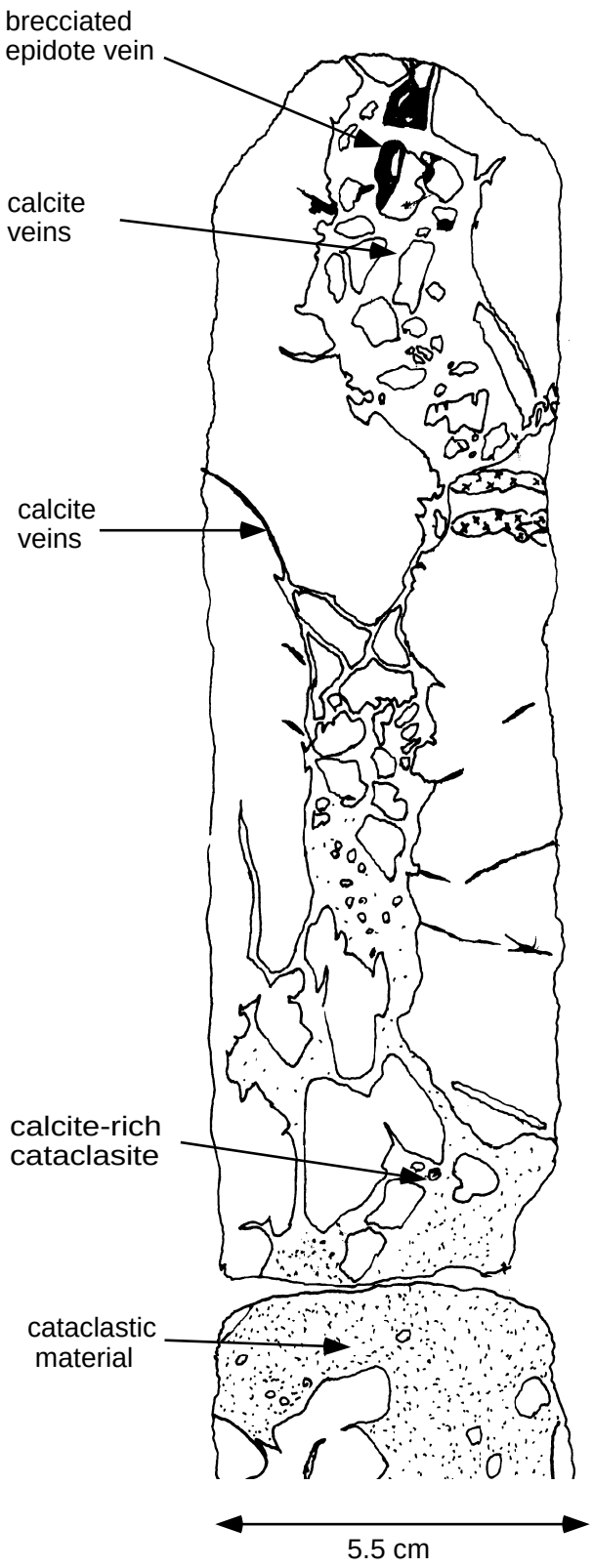

Figure 52. Sketch showing different stages in the development of tectonic breccia. Sample 173-1067A-19R-2, 79–98 cm.

Fluid Inclusions

The variably deformed quartz-rich veins or dikelets in foliated amphibolites, which are discussed above, contain a range of secondary inclusions, which occur along intercrystalline and intracrystalline healed fracture planes, and as small plastic secondary inclusions, which decorate subgrain and recrystallized grain boundaries. The fluid inclusions show a diverse range of sizes, and range in shape from highly irregular necked shapes to negative morphologies. The smallest inclusions generally decorate subgrain boundaries. The commonest inclusion type occurs as linear secondary trails, which crosscut arrays of subgrains. These inclusions are two-phase (liquid and vapor) and occasionally show a consistent liquid-vapor ratio within liquid-rich inclusions from individual trails. In such cases, the liquid-vapor

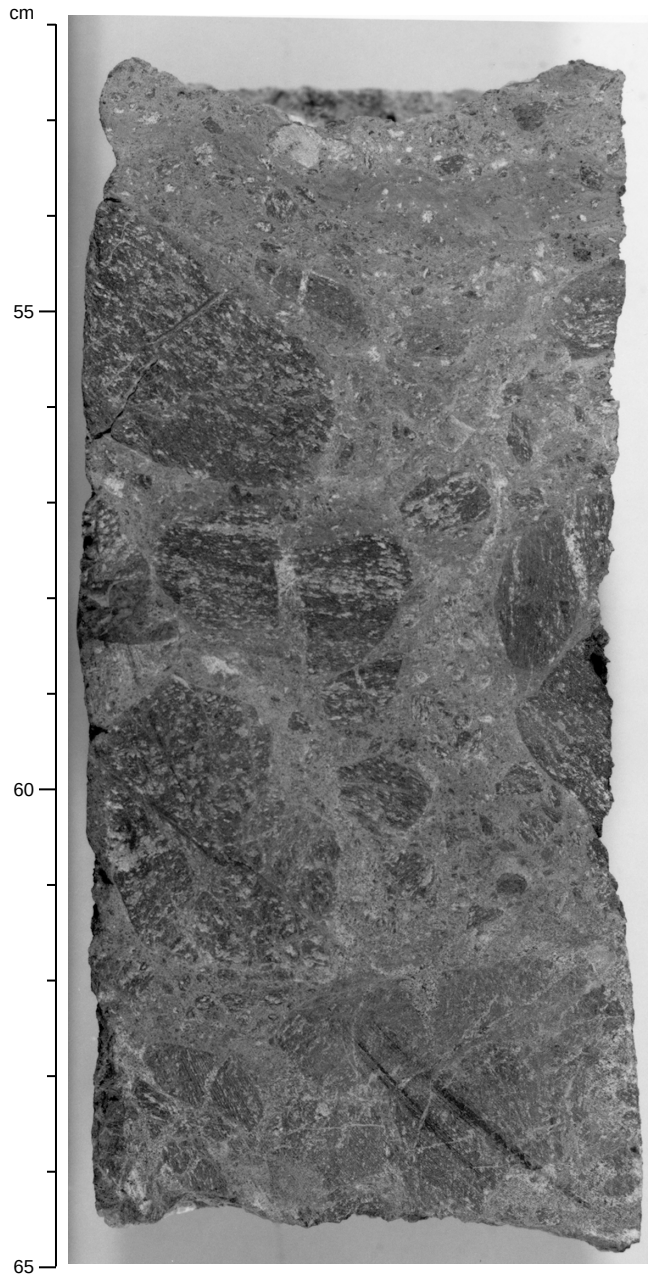

Figure 53. Clast supported breccia (lower part) and matrix supported breccia (upper part). Clasts consist of amphibolite. Note similar orientation of foliation in several amphibolite clasts. Interval 173-1067A-19R-1, 52–65 cm.

ratios are indicative of densities of 0.80 to 0.90 g/cm^3. Less commonly, liquid-rich inclusions also show extensive vapor bubble activity at room temperature, and, rarely, the presence of immiscible fluid types with associated vapor bubbles. In two cases, small liquid-rich inclusions show a transparent daughter mineral phase. The apparent variability in the densities and chemistries of fluid inclusions suggests temporal and/or spatial heterogeneities in salinity and volatile content of the hydrothermal-metamorphic fluid phase(s).

Breccia, Microbreccia, and Fault Gouge

Breccia, microbreccia, and fault gouge overprint the above-described foliation in the amphibolite and tonalite gneiss and are common in the uppermost part of Unit 1 and throughout Unit 2. The relative timing of breccia formation and the above described phases of veining is difficult to ascertain because these processes are intimately involved. However, the following generalized observations can be made in hand specimen: (1) discrete Phase 1 epidote veins are commonly crosscut by fractures and occur within clasts in the breccias, and (2) Phase 2 calcite veins both cut structures in the breccia and elsewhere grade continuously into zones of brecciation (Fig. 52). Thus, in general, brecciation appears to postdate epidote veining and occur before or during calcite veining.

Breccias occur mainly in Units 1, 2, and, to a minor extent, 3, and form zones ranging from 0.2 to 2 m in thickness. The proportion of breccias in Hole 1067A is probably much higher than the proportion in the recovered material (see Fig. 21, "Igneous and Metamorphic Petrology" section, this chapter). Breccia and microbreccia range from clast-supported to matrix-supported (Fig. 53).

Clast-supported breccias are dominated by millimeter- to decimeter-sized, angular clasts (e.g., interval 173-1067A-19R-2, 80–97 cm). "Jigsaw" clast aggregates are commonly observed in the vicinity of the wall rocks. The foliation in the clasts is randomly oriented. However, where the size of the clasts is large relative to the thickness of the breccia zone, the preexisting orientation of the foliation is maintained, as seen by the parallelism between the foliation in the clasts and in the wall rocks.

Matrix-supported breccias commonly occur within clast-supported breccias (e.g., interval 173-1067A-19R-2, 110–140 cm; Fig. 53). The higher the matrix to clast ratio, the rounder and smaller the clasts and the more localized the deformation. The rounded shape of clasts suggests frictional wear during rotation. Commonly, a weak foliation can be observed in matrix supported breccias.

Clasts in all breccia types correspond to the lithologies of the wall rocks. The matrix is mainly formed, as shown by the results of XRD analysis, by plagioclase, amphibole, epidote, calcite, and/or chlorite (see "Igneous and Metamorphic Petrology" section, this chapter), suggesting that the fragmentation of clasts (e.g., plagioclase and amphibole) as well as alteration processes (e.g., formation of calcite and possibly also chlorite and epidote) were important during brecciation.

Microbreccias are composed of millimetric angular rock and mineral fragments. Under the microscope, angular clasts, mainly of plagioclase, are surrounded by fine-grained crystal aggregates. Whereas crystals over 0.05 mm are usually angular, smaller crystals show lobate grain boundaries, suggesting a grain-size–sensitive recrystallization process. However, further studies are necessary to understand this deformation process.

Fault gouges occur along narrow (5–20 cm) zones and are characterized by a high matrix to clast ratio, rounded or elongated clasts, and bands several centimeters thick comprised of fine-grained material (Fig. 54). Together with the elongated clasts, the bands define a weak foliation. An XRD analysis of the gouge matrix yielded a similar composition to that obtained for the breccia matrix (see above and XRD results in "Igneous and Metamorphic Petrology" section, this chapter). The sizes of the clasts range from several tens of millimeters down to a few tenths of a millimeter. The fault gouges can be attributed to moderately to steeply dipping normal faults (Fig. 54).

A possible pseudotachylite was observed in interval 173-1067A-14R-1, 8–15 cm. It occurs as a 0.6-cm-thick band in tonalite gneiss, parallel to the foliation of the latter. Rounded porphyroclasts of plagioclase, amphibole, sphene and epidote and elongate lenses of recrystallized quartz are embedded in a greenish-brown, cryptocrystalline matrix, possibly representing devitrified glass. Alternatively, this rock may represent an ultracataclasite.

Conclusions

Figure 55 summarizes the structural observations on basement rocks recovered at Site 1067. Overall, the rocks are highly deformed. The foliation in the amphibolites formed under amphibolite-facies conditions. The foliation intensity in the amphibolite generally decreases downward, and relict igneous textures are only preserved in Unit 3. However, in the deepest section, there is a recurrence of well-developed foliation. In the absence of clear overprinting relations, the relative timing of the ductile deformation in the amphibolite and the intrusion of the protolith of the tonalite gneiss remain unclear. The protolith may have been intruded during the ductile deformation. Clearly, it must have been intruded before the folding because the tonalitic layers are folded together with the amphibolite host rock. A similar problem refers to the anorthositic pods and patches in Units 2 and 3. The similarity of deformation-related microstructures in the amphibolite and in the anorthosite indicates that these two rock types experienced a similar high-temperature deformation. In some cases, however, the deformation in the anorthosite appears to be less intense than in the surrounding amphibolite, suggesting that the anorthosite pods and patches formed during deformation, but, alternatively, such intensity variations may reflect different chemical/mechanical responses to deformation in amphibole-plagioclase rocks vs. plagioclase-dominated rocks. On the basis of the common occurrence of anorthosites in layered gabbros, coupled with the lack of evidence in the cores of the metamorphic consequences of injecting high-temperature anorthosite magmas into amphibolite facies rocks, it is proposed that the anorthosites are more likely to have formed contemporaneously with the crystallization of the gabbroic precursors of the amphibolites.

At least two phases of retrograde veining and associated wall rock alteration are ubiquitous throughout the core, indicating that fluid-assisted brittle deformation played an important role in the tectonic evolution of the ocean/continent transition in the southern Iberia Abyssal Plain. The foliation and the Phase 1 epidote veins show a systematic decrease of dip with increasing depth. This change in dip may be explained by rotation along brittle fault zones like the one represented by the breccia of Unit 2.

ORGANIC AND INORGANIC GEOCHEMISTRY

Concentrations of carbonate, organic carbon, and total nitrogen in sediments from Hole 1067A were measured on two to four samples per core throughout the cored interval (648.0–855.6 mbsf). Routine measurements were also made of headspace gas compositions as part of the drilling safety program. A single interstitial water sample was collected from Section 173-1067A-9R-3 (729.55 mbsf). Sediments from below this depth were too lithified for interstitial water sampling.

Inorganic and Organic Carbon

Concentrations of carbonate carbon in sediments at Site 1067 vary from 0.18% to nearly 8%, equivalent to $CaCO_3$ concentrations (as-

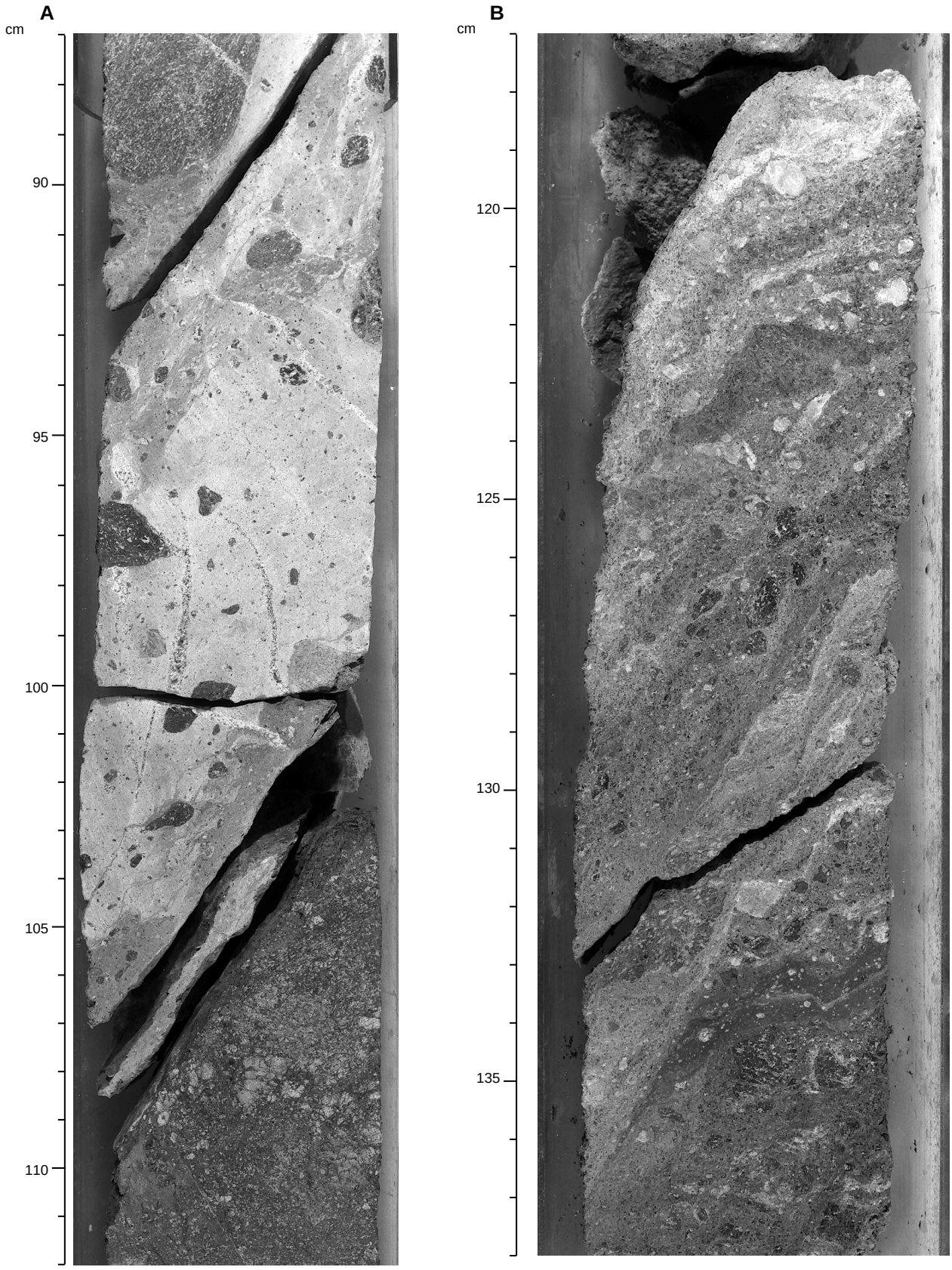

Figure 54. **A.** Zone of calcite-rich fault gouge and two steeply dipping normal fault surfaces with down-dip slickenside lineation (interval 173-1067A-19R-1, 87–112 cm). **B.** Fault gouge with compositional banding, cut by discrete normal faults (interval 173-1067A-19R-2, 117–138 cm).

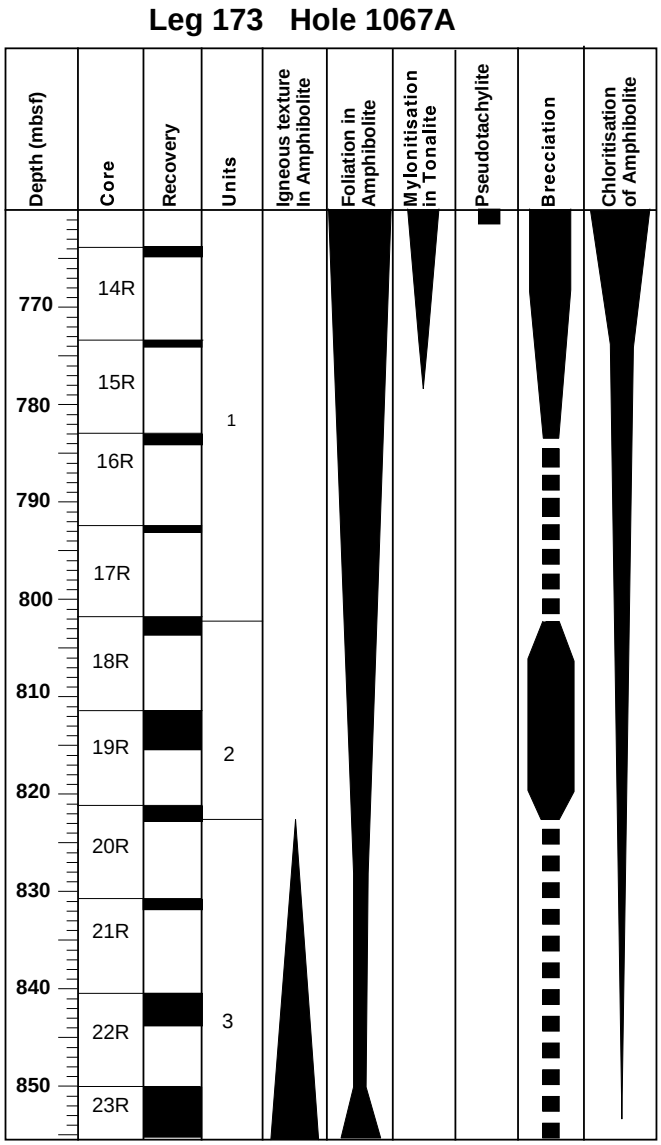

Figure 55. Schematic representation of structural observations on basement lithologies from Hole 1067A.

suming that all the carbonate is present as pure calcite) of 1.5% to 65% (Table 13). All analyzed sediments belong to lithostratigraphic Subunit IIB, which consists of upward-darkening units (3 to 25 cm thick) of basal siltstone/sandstone overlain by calcareous claystone, and capped by claystone (see "Lithostratigraphy" section, this chapter). Shown in Figure 56 are the $CaCO_3$ contents of sediments from the three different lithologic types within individual upward-darkening sequences. In general, the basal siltstone and sandstone layers are more carbonate rich (≤60%) than the overlying calcareous claystone (mostly 20%–30%). The dark claystones that typically form the caps of the upward-darkening sequences have even lower $CaCO_3$ contents, varying from 1.5% to nearly 20%. This pattern is consistent with the interpretation that the basal siltstone and sandstone and overlying calcareous claystone were deposited near or below the CCD by turbidity currents carrying carbonate-rich material from shallower depths, whereas the dark claystones represent hemipelagic sediments.

Table 13. Carbonate, carbon, and nitrogen in sediments from Site 1067.

Core, section, interval (cm)	Depth (mbsf)	Inorganic C (wt%)	$CaCO_3$ (wt%)	Organic C (wt%)	N (wt%)	Organic C/N
173-1067A-						
1R-1, 53-55	648.53	2.57	21.4	0.03	0.05	0.5
1R-3, 43-45	651.43	1.66	13.8	—	—	—
2R-1, 76-77	658.36	2.99	24.9	—	0.05	—
2R-2, 47-48	659.57	5.48	45.6	—	—	—
3R-1, 74-76	668.04	1.80	15.0	0.13	—	—
3R-2, 68-69	669.48	6.19	51.6	—	—	—
4R-2, 36-37	678.76	2.47	20.6	0.04	0.04	1.1
4R-2, 59-61	678.99	5.69	47.4	0.12	—	—
5R-1, 48-49	686.98	4.79	39.9	0.01	0.04	0.3
5R-1, 111-112	687.61	3.06	25.5	0.15	0.05	2.9
5R-2, 55-56	688.55	0.35	2.9	0.11	0.06	1.9
5R-3, 46-47	689.74	7.41	61.7	—	0.04	—
6R-1, 56-57	696.66	2.84	23.7	0.16	0.05	3.1
6R-2, 15-16	697.75	7.76	64.7	—	—	—
7R-1, 75-76	706.55	2.00	16.6	0.37	0.05	7.5
7R-2, 131-133	708.61	5.65	47.1	0.12	—	—
8R-1, 135-136	716.85	2.71	22.6	0.01	0.04	0.3
8R-3, 114-117	719.64	0.93	7.7	0.07	0.04	1.7
9R-1, 69-70	725.89	0.41	3.4	0.02	0.07	0.3
9R-3, 70-71	728.90	2.29	19.1	0.26	0.05	5.2
10R-1, 122-124	736.02	0.18	1.5	0.01	0.05	0.2
10R-3, 66-67	738.46	0.30	2.5	—	0.05	—
11R-1, 89-91	740.49	0.23	1.9	0.02	0.06	0.3
11R-3, 62-64	743.22	1.26	10.5	—	—	—
12R-1, 29-30	744.79	1.08	9.0	0.01	0.06	0.2
12R-2, 24-25	745.74	7.55	62.9	—	0.04	—
13R-1, 45-46	754.65	1.95	16.2	0.10	0.06	1.7

Note: — = concentration was below detection limit.

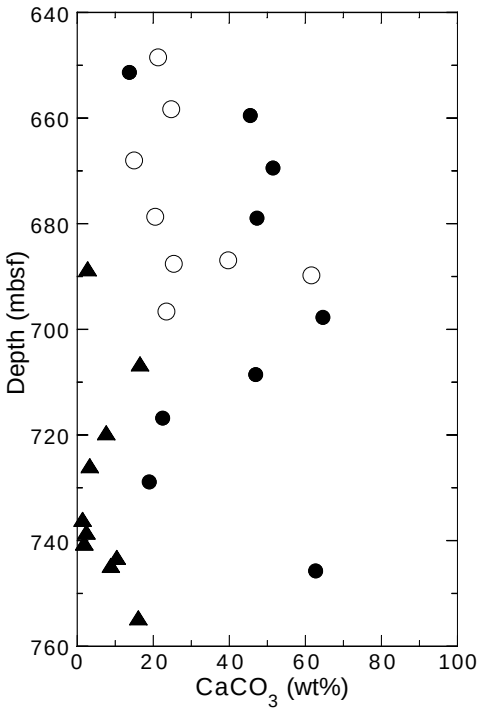

Figure 56. Downhole plot of $CaCO_3$ in sediments from Hole 1067A. Basal siltstone and sandstone layers from individual upward-darkening sequences are shown as solid circles, overlying calcareous claystones as open circles, and hemipelagic claystone as solid triangles.

Table 14. Methane concentrations in headspace gases from Site 1067.

Core, section, interval (cm)	Depth (mbsf)	Methane (ppm)
173-1067A-		
1R-1, 148-150	649.48	3
2R-2, 149-150	660.59	3
3R-3, 149-150	671.79	3
4R-1, 149-150	678.39	5
5R-2, 0-1	688.00	4
6R-1, 149-150	697.59	3
7R-3, 68-69	709.48	3
8R-3, 0-1	718.50	3
9R-3, 149-150	729.69	2
10R-3, 98-100	738.78	3
11R-1, 0-1	739.60	3
12R-1, 0-1	744.50	3

Note: Methane concentrations in all samples are close to the minimum detection limit. No heavier hydrocarbons were found in any of the gas samples.

Table 15. Interstitial water chemistry data for Site 1067.

Core, section, interval (cm)	Depth (mbsf)	SO_4^{2-} (mM)	K^+ (mM)	Cl^- (mM)	Ca^{2+} (mM)	Mg^{2+} (mM)	Na^+ (mM)
173-1067A-							
9R-3, 135-150	729.55	2.93	1.3	516.4	39.7	23.6	382.9

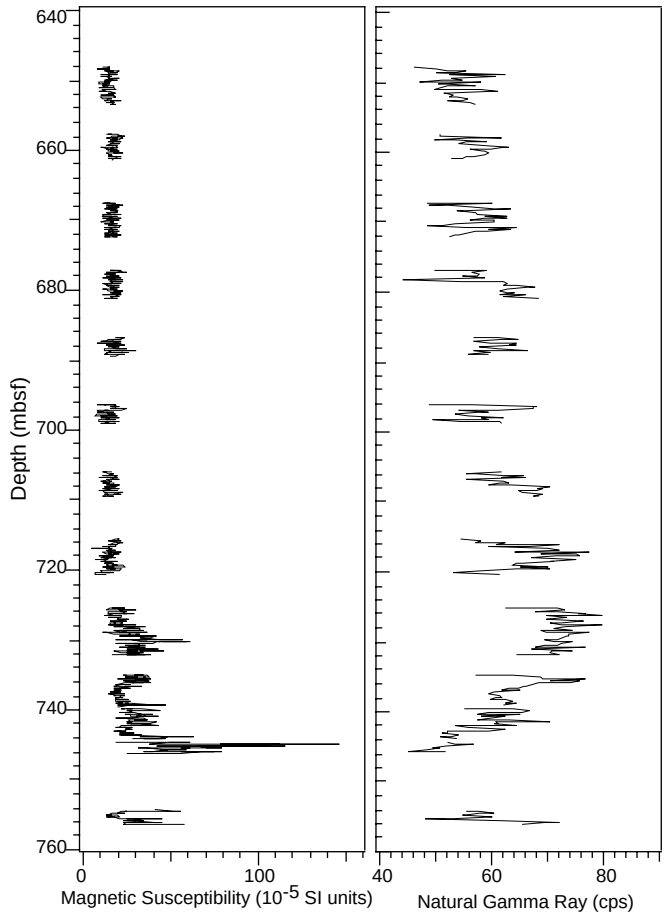

Figure 57. Magnetic susceptibility and natural gamma ray vs. depth at Hole 1067A.

Concentrations of organic carbon are generally quite low (mostly <0.2%) in sediments from Subunit IIB, but values as high as 0.37% are present (Table 13). Nitrogen contents were near or below detection in all samples. The C/N ratios of samples with the highest organic C vary from 3 to 7.5, which indicate a predominantly marine source for the organic matter. The lower C/N ratios of the other samples are probably an artifact of organic C contents that are close to the detection limit.

Headspace Gas Measurements

Methane concentrations in headspace gases were very low at Site 1067, varying from 2 to 5 ppm, and concentrations of heavier hydrocarbons and CO, CO_2, and H_2S were generally below detection (Table 14). Such low values for headspace methane are not surprising given the low organic C contents of the sediments. Similar low values were found in sediments at Site 900 (Shipboard Scientific Party, 1994a), located 0.8 km to the west of Site 1067.

Interstitial Water

The single interstitial water sample collected from 729.55 mbsf in Hole 1067A has cation and anion concentrations (Table 15) that are very similar to those in interstitial water collected from a similar depth (721.5 mbsf) at Site 900 (Shipboard Scientific Party, 1994a). At the latter site, a complete profile of interstitial water compositions was determined from 12.6 to 721.5 mbsf.

PHYSICAL PROPERTIES

For convenience, Hole 1067A physical property data were separated into two sections: sedimentary units and basement units. The same physical properties were measured on both sediment and basement samples; however, because of the variation in competency of these samples, some measurement techniques differed. Also, classifications of hard rock lithologies have been simplified for the discussion of physical property data, because trends in the data are recognizable for only two major rock types: amphibolites and breccias. Only one lithostratigraphic unit was identified at Site 1067.

For all lithologies, physical properties were measured on both split cores and discrete samples. Because of voids between sedimentary rocks and core liners, as well as discontinuity of recovery, GRAPE and compressional-wave velocity measurements were not conducted on the multisensor track (MST). MST measurements of magnetic susceptibility and natural gamma radiation were made on all sedimentary cores in Hole 1067A at a 5-cm sampling interval. Although the magnetic susceptibility and natural gamma radiation measurements were inaccurate and scattered, they may be useful when used semi-quantitatively.

Compressional-wave velocities were measured using split cores and discrete samples, while thermal conductivity measurements required the exclusive use of split core samples. Unlike most of the sediment cores in Hole 1067A, the basement rock was competent enough to allow for polishing samples for thermal conductivity measurements. As a result, most thermal conductivities are reported for basement samples. The index properties of minicore samples included wet and dry mass and dry volume, which were then used to calculate porosity, grain and bulk density, void ratio, and water content.

Multisensor Track

Only measurements of magnetic susceptibility and natural gamma radiation were performed on the whole-round sediment cores (Fig. 57; Tables 16, 17 on CD-ROM, back pocket, this volume). Values of magnetic susceptibility are mostly less than 20×10^{-5} SI units above

Table 18. Index properties data from Hole 1067A.

Core, section, interval (cm)	Depth (mbsf)	Bulk density (g/cm^3)	Grain density (g/cm^3)	Porosity (%)	Water content (% dry mass)	Lithology
173-1067A-						
Sediments						
1R-1, 53-55	648.53	2.14	2.68	32	48	Claystone
1R-3, 43-45	651.43	2.17	2.52	24	31	Sandstone
2R-1, 76-78	658.36	2.15	2.71	33	49	Claystone
2R-2, 47-49	659.57	2.51	2.67	10	11	Sandstone
3R-1, 74-76	668.04	2.10	2.70	36	55	Claystone
3R-2, 67-69	669.47	2.54	2.70	10	11	Sandstone
4R-2, 37-39	678.77	2.20	2.69	30	42	Claystone
4R-2, 60-62	679.00	2.51	2.69	11	12	Sandstone
5R-1, 52-54	687.02	2.34	2.70	22	28	Claystone
5R-3, 48-50	689.76	2.38	2.70	19	24	Claystone
6R-1, 56-58	696.66	2.27	2.70	26	34	Claystone
6R-2, 13-15	697.73	2.62	2.69	4	4	Sandstone
7R-1, 74-76	706.54	2.16	2.68	32	46	Claystone
7R-2, 131-133	708.61	2.57	2.68	6	7	Sandstone
8R-1, 135-137	716.85	2.58	2.67	5	5	Sandstone
8R-3, 114-116	719.64	2.15	2.71	33	49	Claystone
9R-1, 67-69	725.87	2.08	2.71	38	60	Claystone
9R-3, 69-71	728.89	2.33	2.70	22	28	Sandstone
10R-1, 121-123	736.01	2.13	2.70	34	51	Claystone
10R-3, 64-66	738.44	2.09	2.68	35	55	Claystone
11R-1, 88-90	740.48	2.11	2.69	35	54	Claystone
11R-3, 60-62	743.20	2.08	2.61	34	51	Claystone
12R-1, 32-34	744.82	2.08	2.66	36	55	Claystone
12R-2, 24-26	745.74	2.41	2.72	18	22	Sandstone
13R-1, 46-48	754.66	2.18	2.70	31	45	Claystone
Basement						
16R-1, 83-85	783.73	2.80	2.99	10	11	Amphibolite
16R-2, 9-11	784.22	2.75	2.93	10	11	Amphibolite
18R-1, 49-51	802.39	2.54	2.76	13	15	Breccia
18R-2, 28-30	803.43	2.98	3.05	3	3	Amphibolite
18R-2, 87-89	804.02	2.88	2.95	4	4	Amphibolite
19R-2, 33-35	813.26	2.81	3.01	10	11	Breccia
20R-2, 43-45	823.03	2.90	2.98	4	4	Amphibolite
22R-1, 97-99	841.37	2.80	2.92	7	7	Amphibolite
22R-2, 25-27	841.91	2.80	2.89	5	5	Amphibolite
23R-1, 23-25	850.23	2.82	3.01	9	10	Breccia
23R-2, 7-9	851.57	2.89	2.98	4	4	Amphibolite
23R-4, 13-15	854.13	2.93	2.98	3	3	Amphibolite

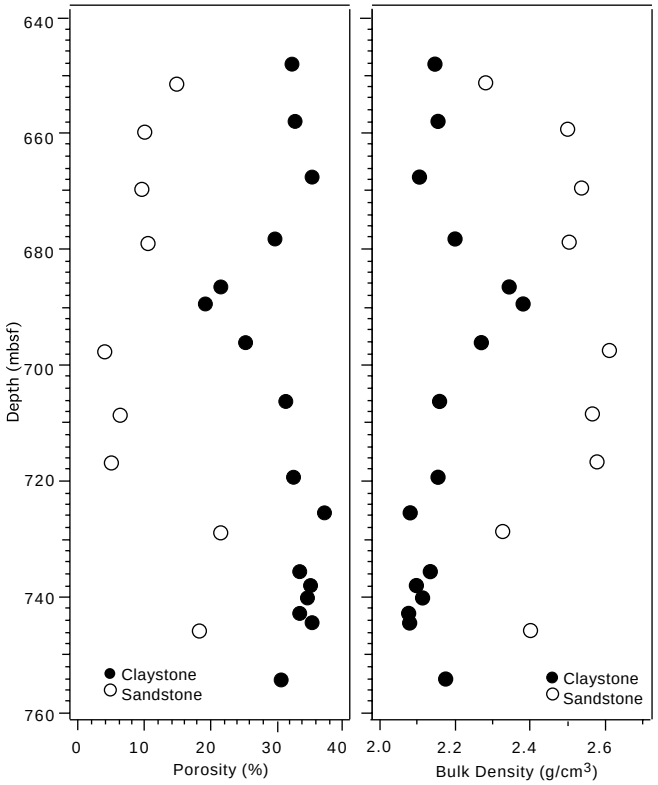

Figure 58. Sediment porosity and bulk density vs. depth at Hole 1067A. Solid circles = claystones, open circles = sandstones.

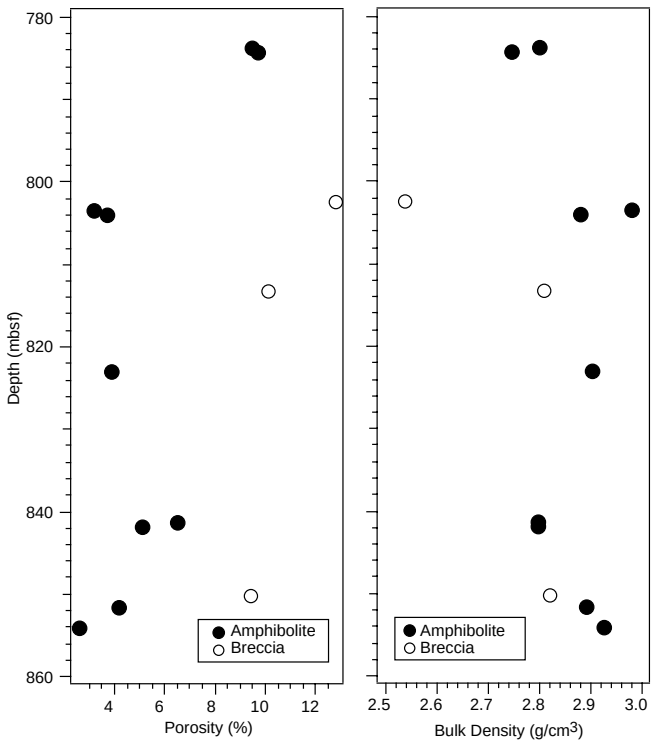

Figure 59. Basement porosity and bulk density vs. depth at Hole 1067A.

720 mbsf and average ~30–40 × 10^{-5} SI units below this depth. The maximum value is over 140 × 10^{-5} SI units near 745 mbsf. Natural gamma radiation ranges from 44 to 80 total counts per second through the entire core with a local maximum near 727 mbsf. This peak reflects enrichment in U, Th, or K and is roughly coincident with an increased abundance of red-brown claystone relative to green-gray claystone.

Index Properties

Standard procedures were followed for measuring sample mass and volume except that discrete minicore samples (basement units only) had to be saturated with Nanno-Pure water in a vacuum chamber before wet properties could be measured. This was necessary because sampling of hard rock cores for shipboard measurements was done only once per day, allowing evaporation of rock pore fluids. The sampling frequency for index property measurements (Table 18) was approximately twice per core and all sedimentary samples were classified as either claystone or sandstone (see "Lithostratigraphy" section, this chapter). Grain and bulk density, porosity, water content, and void ratio were calculated from sample mass and volume (Table 18).

Sediments

Sediment bulk densities range from 2.08 to 2.62 g/cm^3 and their porosities range from 4% to 38%. With the exception of one sample (Sample 173-1067A-1R-3, 43 cm), values for grain density are tightly clustered around 2.7 g/cm^3 through the entire unit. The grain density of 2.52 g/cm^3 for Sample 173-1067A-1R-3, 43 cm, may be an error because chemical and XRD data indicate no change in grain composition when compared to other samples.

Plots of bulk density and porosity vs. depth (Fig. 58) indicate that claystones and sandstones separate into two distinct populations. Whereas claystones have porosities greater than 20% and bulk densities less than 2.4 g/cm^3, sandstones tend to have porosities less than 20% and bulk densities greater than 2.3 g/cm^3. Some samples, which are composed of both sand and clay, have properties in between the two end-members. There appears to be a local minimum in claystone porosity near 690 mbsf. Claystones vary in color, from red-brown to green-gray, but there is no distinct correlation of index properties with color.

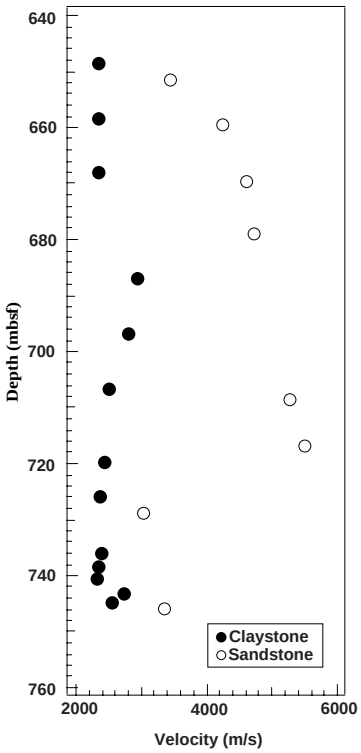

Figure 60. Sediment compressional-wave velocity vs. depth at Hole 1067A.

Basement Units

The bulk density and porosity measurements for all basement samples are shown in Figure 59. Bulk densities for the two dominant lithologies are comparable; however, porosities for the two lithologies have distinct distributions. The nine amphibolite samples, which dominate in basement, have a lower average porosity (5.4%) than the three less abundant breccias (10.8%). Amphibolite bulk densities range from 2.75 to 2.98 g/cm^3 and breccia densities vary from 2.54 to 2.82 g/cm^3. Because both moisture content and void ratio are directly proportional to porosity, they vary with lithology in the same manner. Grain densities are also comparable, with the amphibolites and breccias having averages of 2.93 g/cm^3 and 2.96 g/cm^3, respectively.

Table 20. Compressional-wave velocity data from Hole 1067A.

Core, section, interval (cm)	Depth (mbsf)	Velocity (m/s)	Lithology
173-1067A-			
Sediments			
1R-1, 53	648.53	2351	Claystone
1R-3, 43	651.43	3439	Sandstone
2R-1, 76	658.36	2337	Claystone
2R-2, 47	659.57	4248	Sandstone
3R-1, 74	668.04	2344	Claystone
3R-2, 67	669.47	4595	Sandstone
4R-2, 62	679.02	4715	Sandstone
5R-1, 54	687.04	2928	Claystone
6R-1, 58	696.68	2799	Claystone
7R-1, 74	706.54	2503	Claystone
7R-2, 131	708.61	5265	Sandstone
8R-1, 135	716.85	5490	Sandstone
8R-3, 114	719.64	2424	Claystone
9R-1, 67	725.87	2356	Claystone
9R-3, 69	728.89	3020	Sandstone
10R-1, 121	736.01	2393	Claystone
10R-3, 64	738.44	2348	Claystone
11R-1, 90	740.50	2328	Claystone
11R-3, 62	743.22	2727	Claystone
12R-1, 34	744.84	2551	Claystone
12R-2, 26	745.76	3345	Sandstone
13R-1, 46	754.66	2427	Claystone
Basement			
14R-1, 51	764.31	5152	Amphibolite
15R-1, 0.1	773.40	5489	Amphibolite
15R-1, 29	773.69	5909	Amphibolite
16R-1, 67	783.57	5897	Amphibolite
16R-1, 67	783.57	5884	Amphibolite
16R-1, 83	783.73	5891	Amphibolite
16R-2, 11	784.24	5284	Amphibolite
18R-1, 49	802.39	4375	Breccia
18R-2, 28	803.43	6195	Amphibolite
18R-2, 87	804.02	5566	Amphibolite
19R-1, 96	812.46	4554	Breccia
19R-2, 8	813.01	4525	Breccia
19R-2, 33	813.26	4643	Breccia
19R-2, 123	814.16	4498	Breccia
19R-4, 46	815.79	5339	Amphibolite
19R-4, 52	815.85	5586	Amphibolite
20R-2, 43	823.03	6131	Amphibolite
22R-1, 37	840.77	4911	Amphibolite
22R-1, 95	841.35	5593	Amphibolite
22R-1, 97	841.37	5391	Amphibolite
22R-2, 25	841.91	5697	Amphibolite
22R-2, 45	842.11	5351	Amphibolite
22R-3, 70	843.83	5507	Amphibolite
22R-3, 142	844.55	6353	Amphibolite
23R-1, 23	850.23	4629	Breccia
23R-1, 130	851.30	5814	Amphibolite
23R-2, 7	851.57	5450	Amphibolite
23R-2, 68	852.18	5260	Amphibolite
23R-3, 60	853.45	5439	Amphibolite
23R-4, 13	854.13	6358	Amphibolite
23R-4, 67	854.67	5147	Amphibolite

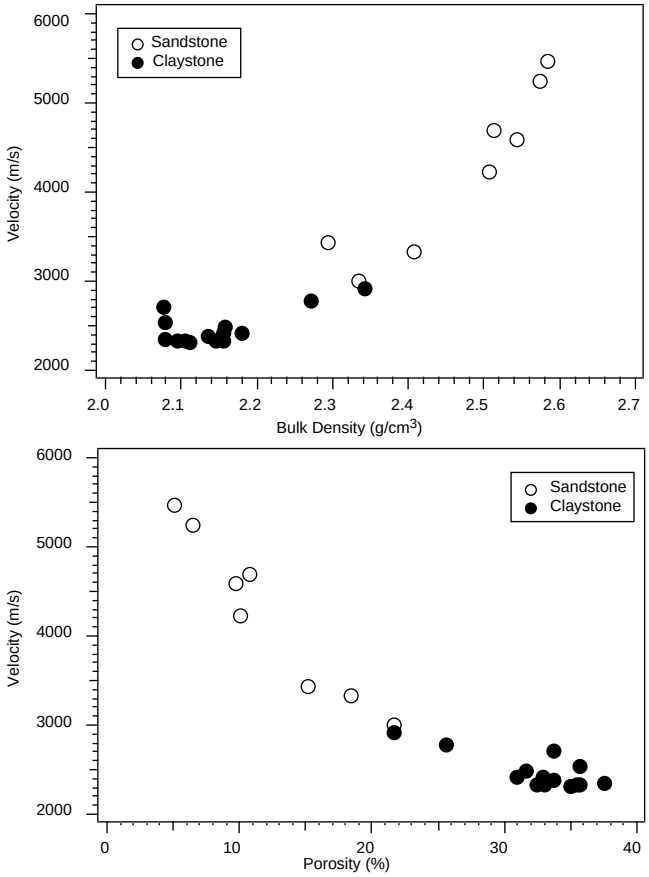

Figure 61. Bulk density and porosity vs. compressional-wave velocity for sediment at Hole 1067A.

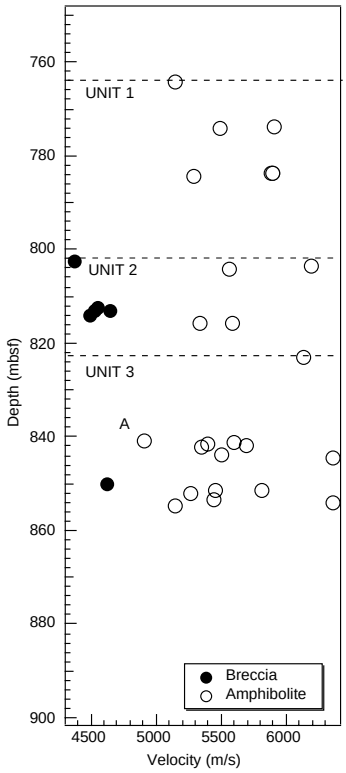

Figure 62. Basement compressional-wave velocity vs. depth at Hole 1067A. A = Sample 173-1067A-22R-1, 37 cm, which has a breccia-amphibolite transitional velocity.

Thermal Conductivity

Thermal conductivities were measured on split core sections using a half-space probe configuration. Most sediment cores were not competent enough to allow for surface polishing which facilitates adequate sample-probe coupling; therefore, the determination of thermal conductivity in sediment cores was limited to five measurements (Table 19 on CD-ROM, back pocket, this volume). Sediment thermal conductivity measurements range from 1.60 to 1.90 W/(m·K). The sampling frequency in basement cores, starting with Core 173-1067A-14R, was much greater than for sedimentary lithologies, but the six data points, clustering around 2.00 W/(m·K), show no systematic variation with rock type or depth below seafloor (Table 19 on CD-ROM, back pocket, this volume). Amphibolites dominate crystalline basement. Given our sampling interval, variations in rock mineralogy would probably not be resolved by the thermal conductivity data.

Acoustic Velocity

All acoustic velocity measurements were made with the Hamilton-Frame Velocimeter. The MST compressional-wave logger transducers were ineffective on the undersized cores, so no MST compressional-wave data were recorded.

Sediments

Compressional-wave velocity measurements were made on split cores when the material was soft or on minicores when sediments were sufficiently competent. All sediment samples were classified as either claystone or sandstone. A plot of velocity vs. depth for sediments is shown in Fig. 60, and the corresponding data are listed in Table 20.

The velocities of the claystones are relatively uniform with depth and average 2.4 km/s with several measurements of somewhat higher velocities within a depth interval of increased density (Fig. 58). Sandstone velocities increase with depth from less than 4.0 km/s at 650 mbsf to 5.7 km/s at 714 mbsf. Below 714 mbsf, sand layers are increasingly mixed with clays and a pure sand end-member was not recovered. Velocity measurements displayed a simple curved trend when plotted against bulk density and porosity measurements (Fig. 61).

Basement Units

The compressional-wave velocities of basement cores show the same bimodal distribution as the porosities. The relationship between velocity and depth below seafloor is illustrated in Figure 62. Amphibolites have higher velocities than the breccias. Amphibolite velocities range from 4.9 to 6.4 km/s with only three measurements below 5.2 km/s. The breccia velocities range from 4.4 to 4.6 km/s. This result was expected assuming that the breccias have a larger microcrack and fracture porosity. One sample (labeled “A” in Fig. 62), which has the lowest velocity in the amphibolite suite, seems to have a transitional velocity. This sample (Sample 173-1067A-22R-1, 37 cm) appears to be an amphibolite that is less brecciated than those in the breccia units, and, consequently, has a velocity value that is diagnostic of neither lithology.

Cross-correlation plots of density and porosity vs. velocity for basement samples are displayed in Figure 63. Both the amphibolites

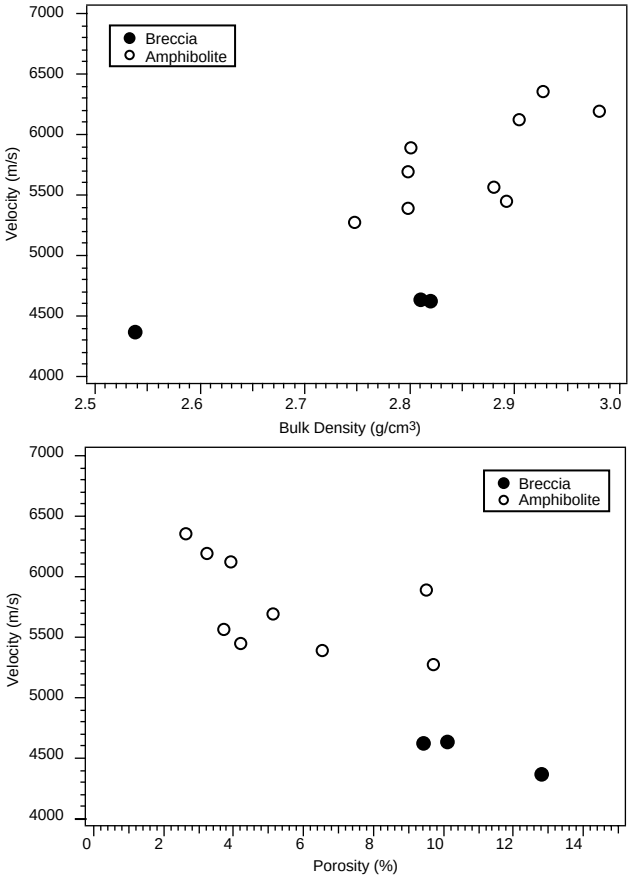

Figure 63. Bulk density and porosity vs. compressional-wave velocity for basement at Hole 1067A.

and the breccias exhibit the expected negative correlation between velocity and porosity; however, when plotted against density, two breccia samples from Units 2 and 3 (Fig. 63) have unexpectedly low velocities. These two samples (Samples 173-1067A-19R-2, 33 cm, and 23R-1, 23 cm) do not show outlying values on the porosity vs. velocity plot (Fig. 63). This phenomenon suggests that the breccia samples have a different relationship between density and velocity compared to the amphibolites.

SUMMARY AND CONCLUSIONS

Summary

The history of this site began with the formation of the mafic rocks recovered from the basement. The preliminary shipboard geochemical and tectono-metamorphic analysis of the amphibolites indicates a gabbroic protolith that formed from differentiated mafic magma with incompatible trace element abundances similar to those in enriched MORB. They could represent former gabbro metamorphosed under amphibolite facies conditions. However, as no relict pyroxene was even tentatively identified in these rocks, the hypothesis of magmatic hornblende gabbro cannot be excluded, such rocks being described in the Variscan belt as part of a water-rich bimodal magmatism related to a former rifting event (Briand et al., 1995). The amphibolite underwent heterogeneous ductile deformation under amphibolite facies conditions, retrograde metamorphism, and intense extensional deformation under greenschist facies conditions. The timings of intrusion of the protoliths of the tonalite gneiss and meta-anorthosites were not resolved with certainty; they may have crystallized along with gabbro before amphibolite facies metamorphism, or, alternatively, the tonalite and anorthosite may have been emplaced during metamorphism. The meta-anorthosite occurs either as veins folded and aligned with the foliation or as irregular patches. The tonalite gneiss, which is observed only in the upper part of the cored section, displays a foliation mainly concordant with that of the host amphibolite. The origin of the meta-anorthosite is not constrained at present by any shipboard geochemical data. Anorthosite can occur as both layers and irregular patches within gabbros (e.g., Irvine, 1980), so that hand sample and petrographic observations of the meta-anorthosites can be explained in terms of pre-metamorphic igneous processes.

Whatever their origin, the tonalite gneiss, the meta-anorthosite, and the amphibolites underwent a common evolution under amphibolite to greenschist facies conditions. The intensity of the ductile deformation generally decreases from the top toward the bottom of the cored section, although it is intense again in the deepest section. It created a clear foliation in the upper and the lowermost parts of the section while magmatic textures are locally preserved in between. Some textural features suggest a simple shear component during the deformation. This observation suggests that a ductile shear zone developed in the amphibolite at a level that is now at the top of the basement. The late heterogeneous deformation under greenschist facies conditions is mainly localized in the middle part of the cored section, which indicates that the accommodation of the deformation varied through time and space during the retrograde evolution.

The magnetic properties of basement Units 1 and 2 appear to be dominated by magnetite (average intensity $>5 \times 10^{-2}$ A/m and $Q \geq 0.5$) whereas those of Unit 3 are dominated by pyrrhotite (about 2×10^{-3} A/m and $Q = 0.07$). There is also a positive correlation between the inclination angles of the stable magnetic vectors and the foliation planes of the basement cores. The amphibolites have velocities in the range from 4.9 to 6.4 km/s (mostly >5.2 km/s), whereas the more fractured breccia has velocities of 4.4 to 4.6 km/s. All these velocities are well in excess of the interval velocity of 4.06 km/s predicted for the layer above the H reflector from depth focusing error analysis (Krawczyk et al., 1996).

The sedimentary history at this site began in the late Paleocene and the top of the cored section was dated as middle Eocene. The sediment/basement contact was not cored. All the cored sediments belong to a single lithostratigraphic subunit that consists of claystone and calcareous claystone with subordinate calcareous silty claystone, calcareous siltstone, and sandy siltstone. These sediments appear to be a mixture of (1) nannofossil-rich, carbonate-rich turbidites, and (2) carbonate-poor hemipelagic material that was deposited at the base of the continental rise below the carbonate compensation depth. The turbidites could have come from the north or from the Iberian margin to the east. The hemipelagic sediments appear to have been brown when first deposited, but subsequent chemical reduction has locally turned them green. Relatively deep water is indicated by the occurrence of certain benthic foraminifer species. There are also signs of reworking by contour currents. Near the base of the section there is a thin matrix-supported conglomerate with 1- to 5-mm clasts of shallow-water limestone and pebbles of pelite. The clasts are very similar in appearance to the clasts in the Upper Jurassic and Miocene sediments of Site 1065. A possible source for all these clasts is the shallow-water banks and seamounts that lie to the north of the sites. Angular quartz grains (63–500 µm) suggest a nearby source and heavy minerals such as hornblende and feldspar probably came from outcrops of the underlying basement. The bedding planes show true dips of unknown origin between 0° and 20° (average 11.5° ± 5.3°), without showing a clear systematic trend downhole. The green sediment is about an order of magnitude more weakly magnetized than, and has about half the susceptibility of, the brown sediment.

Discussion and Conclusions

The two most probable hypotheses for the formation of the amphibolite and intrusive tonalite gneiss and meta-anorthosite are that (1) they represent synrift melting products of the mantle or (2) they are part of the Variscan continental crust remobilized during Mesozoic rifting.

The metagabbro recovered at Site 900 (Leg 149), located 800 m westward on the same structural basement high, displays transitional to typical MORB affinities (Cornen et al, 1996; Seifert et al., 1996, 1997). These rocks were strongly sheared in granulite facies conditions (Cornen et al., 1996), and this deformation ended by 136 Ma (Féraud et al., 1996). These gabbros then underwent a mainly static metamorphism and an intense fluid-assisted extensional deformation under greenschist facies conditions. This tectono-metamorphic evolution suggests that the gabbros represent melting products of the mantle, which were underplated at the base of the thinned continental crust during rifting, and were then tectonically unroofed and exposed in the continental breakup zone (Beslier et al., 1995; Cornen et al., 1996; Brun and Beslier, 1996). Geochemical data show that the Site 1067 amphibolites are more differentiated than the Site 900 metagabbros. These results suggest that the two types of rocks may be genetically linked (different stages of differentiation of the same mantle-derived magma emplaced during the same magmatic event) and that they had a comparable post-igneous evolution. However, the metagabbro retains the memory of a higher grade early intense deformation, suggesting that the two types of rock were not at the same structural level during their evolution. At Site 900, the foliation in the metagabbro generally dips from 15° to 45° (Shipboard Scientific Party, 1994a). As no reorientation of the cores was possible, the dip direction of the foliation is not determined. On the multichannel seismic profile Lusigal-12 across Sites 900 and 1067, the H reflector, which appears to crosscut the basement surface in the vicinity of Site 900, dips toward the east (Krawczyk et al., 1996). Assuming that this strong reflector represents a major synrift tectonic contact, as suggested by the very intense shear deformation observed in the metagabbro, it is most probable that the foliation in the metagabbro is parallel to this reflector and dips toward the east. In this case, the amphibolites may overlie the metagabbros and this geometry is consistent with an evolution of the amphibolites at a shallower structural level than the metagabbros. The intense ductile deformation observed in the upper amphibolite and in the metagabbro shows that two shear zones may have developed, simultaneously or consecutively, and could be responsible for the tectonic unroofing of these rocks from deeper crustal levels toward the surface.

These previous results and the very preliminary studies of the Site 1067 rocks suggest that the Site 1067 amphibolite, meta-anorthosite, and tonalite gneiss may have an origin and an evolution compatible with that of the Site 900 metagabbro, the amphibolite having evolved probably at a shallower structural level than the metagabbro. Hence, both types of rock may represent products of synrift mantle melting, probably underplated and then tectonically unroofed during the last stages of continental rifting and crustal breakup.

Further shorebased studies, including radiometric dating, are needed to define the origin and petrostructural evolution of basement rocks from Site 1067 and to test these hypotheses.

REFERENCES

Berggren, W.A., Kent, D.V., Swisher, C.C., III, and Aubry, M.-P., 1995. A revised Cenozoic geochronology and chronostratigraphy. *In* Berggren, W.A., Kent, D.V., Aubry, M.-P., and Hardenbol, J. (Eds.), *Geochronology, Time Scales and Global Stratigraphic Correlation.* Spec. Publ.—Soc. Econ. Paleontol. Mineral., 54:129–212.

Beslier, M.-O., 1996. Data report: Seismic line LG12 in the Iberia Abyssal Plain. *In* Whitmarsh, R.B., Sawyer, D.S., Klaus, A., and Masson, D.G. (Eds.), *Proc. ODP, Sci. Results,* 149: College Station, TX (Ocean Drilling Program), 737–739.

Beslier, M.-O., Bitri, A., and Boillot, G., 1995. Structure de la transition continent-océan d'une marge passive: sismique réflexion multitrace dans la Plaine Abyssale Ibérique (Portugal). *C. R. Acad. Sci. Ser. 2,* 320:969–976.

Beslier, M.-O., and Brun, J.-P., 1991. Boudinage de la lithosphère et formation des marges passives. *C. R. Acad. Sci. Ser. 2,* 313:951–958.

Boillot, G., Girardeau, J., and Kornprobst, J., 1988. Rifting of the Galicia Margin: crustal thinning and emplacement of mantle rocks on the seafloor. *In* Boillot, G., Winterer, E.L., et al., *Proc. ODP, Sci. Results,* 103: College Station, TX (Ocean Drilling Program), 741–756.

Bouma, A.H., 1962. *Sedimentology of Some Flysch Deposits: A Graphic Approach to Facies Interpretation:* Amsterdam (Elsevier).

Briand, B., Bouchardon, J.L., Ouali, H., Piboule, M., and Capiez, P., 1995. Geochemistry of bimodal amphibolitic-gneiss complexes from the eastern Massif Central, France. *Geol. Mag.,* 132:321 337.

Brun, J.P., and Beslier, M.-O., 1996. Mantle exhumation at passive margins. *Earth Planet. Sci. Lett.,* 142:161–173.

Cannat, M., Karson, J.A., Miller, D.J., et al., 1995. *Proc. ODP, Init. Repts.,* 153: College Station, TX (Ocean Drilling Program).

Cornen, G., Beslier, M.-O., and Girardeau, J., 1996. Petrology of the mafic rocks cored in the Iberia Abyssal Plain. *In* Whitmarsh, R.B., Sawyer, D.S., Klaus, A., and Masson, D.G. (Eds.), *Proc. ODP, Sci. Results,* 149: College Station, TX (Ocean Drilling Program), 449–469.

Dean, S.M., Minshull, T.A., Whitmarsh, R.B., Louden, K., and Chian, D., 1996. A seismic study of the ocean-continent transition in the Iberia Abyssal Plain. *Eos,* 77:F668.

de Charpal, O., Guennoc, P., Montadert, L., and Roberts, D.G., 1978. Rifting, crustal attenuation and subsidence in the Bay of Biscay. *Nature,* 275:706–711.

Deer, W.A., Howie, R.A., and Zussman, J., 1982. *Zircon: Rock-forming Minerals* (Vol. 1A): *Orthosilicates* (2nd ed.): London (Longman), 412–442.

————, 1993. *Apatite: The Rock-forming Minerals* (3rd ed.): London (Longman), 663–669.

Denelle, E., Dezard, Y., and Raoult, J., 1986. 2-D prestack depth migration in the (S-G-W) domain. *56th SEG Meet., Houston, TX.* (abstract)

Féraud, G., M.-O. Beslier, and Cornen, G., 1996. $^{40}Ar/^{39}Ar$ dating of gabbros from the ocean/continent transition of the western Iberia Margin: preliminary results. *In* Whitmarsh, R.B., Sawyer, D.S., Klaus, A., and Masson, D.G. (Eds.), *Proc. ODP, Sci. Results,* 149: College Station, TX (Ocean Drilling Program), 489–495.

Froitzheim, N., and Eberli, G.P., 1990. Extensional detachment faulting in the evolution of a Tethys passive continental margin, Eastern Alps, Switzerland. *Geol. Soc. Am. Bull.,* 102:1297–1308.

Groupe Galice, 1979. The continental margin off Galicia and Portugal: acoustical stratigraphy, dredge stratigraphy, and structural evolution. *In* Sibuet, J.-C., Ryan, W.B.F., et al., *Init. Repts. DSDP,* 47 (Pt. 2): Washington (U.S. Govt. Printing Office), 633–662.

Irvine, T.N., 1980. Magmatic infiltration metasomatism, double-diffusive fractional crystallization, and adcumulus growth in the Muskox Intrusion and other layered intrusions. *In* Hargraves, R.B. (Ed.), *Physics of Magmatic Processes:* Princeton, NJ (Princeton Univ. Press), 325–384.

Keen, C.E., Boutilier, R., De Voogd, B., Mudford, B., and Enachescu, M.E., 1987a. Crustal geometry and extensional models for the Grand Banks, eastern Canada: constraints from deep seismic reflection data. *In* Beaumont, C., and Tankard, A.J. (Eds.), *Sedimentary Basins and Basin-Forming Mechanisms.* CSPG Mem., 12:101–115.

Keen, C.E., Stockmal, G.S., Welsink, H., Quinlan, G., and Mudford, B., 1987b. Deep crustal structure and evolution of the rifted margin northeast of Newfoundland: results from Lithoprobe East. *Can. J. Earth Sci.,* 24:1537–1549.

Krawczyk, C.M., 1995. Detachment tectonics during continental rifting off the west Iberian Margin: seismic reflection and drilling constraints. *GEOMAR Rep. 37.*

Krawczyk, C.M., Reston, T.J., Beslier, M.-O., and Boillot, G., 1996. Evidence for detachment tectonics on the Iberia Abyssal Plain rifted margin. *In* Whitmarsh, R.B., Sawyer, D.S., Klaus, A., and Masson, D.G. (Eds.), *Proc. ODP, Sci. Results,* 149: College Station, TX (Ocean Drilling Program), 603–615.

Kuhnt, W., and Collins, E.S., 1996. Cretaceous to Paleogene benthic foraminifers from the Iberia Abyssal Plain. *In* Whitmarsh, R.B., Sawyer, D.S., Klaus, A., and Masson, D.G. (Eds.), *Proc. ODP, Sci. Results,* 149: College Station, TX (Ocean Drilling Program), 203–216.

Le Pichon, X., and Barbier, F., 1987. Passive margin formation by low-angle faulting within the upper crust: the northern Bay of Biscay margin. *Tectonics*, 6:133–150.

Lister, G.S., and Davis, G.A., 1989. The origin of metamorphic core complexes and detachment faults formed during Tertiary continental extension in the Northern Colorado River region, U.S.A. *J. Struct. Geol.*, 11:65–94.

Lister, G.S., Etheridge, M.A., and Symonds, P.A., 1986. Detachment faulting and evolution of passive continental margins. *Geology*, 14:246–250.

Liu, L., 1996. Eocene calcareous nannofossils from the Iberia Abyssal Plain. *In* Whitmarsh, R.B., Sawyer, D.S., Klaus, A., and Masson, D.G. (Eds.), *Proc. ODP, Sci. Results*, 149: College Station, TX (Ocean Drilling Program), 61–78.

Ludden, J.N., and Thompson, G., 1979. An evaluation of the behavior of the rare earth elements during the weathering of sea floor basalt. *Earth Planet. Sci. Lett.*, 43:85–92.

Martini, E., 1971. Standard Tertiary and Quaternary calcareous nannoplankton zonation. *In* Farinacci, A. (Ed.), *Proc. 2nd Int. Conf. Planktonic Microfossils Roma:* Rome (Ed. Tecnosci.), 2:739–785.

Mauffret, A., and Montadert, L., 1987. Rift tectonics on the passive continental margin off Galicia (Spain). *Mar. Pet. Geol.*, 4:49–70.

Minshull, T.A., 1995. *A Geophysical Study of the Ocean-continent Transition in the Iberia Abyssal Plain, R.R.S. Discovery Cruise 215*. Bullard Labs., Dep. Earth Sci., Cambridge Univ.

Montadert, L., de Charpel, O., Roberts, D., Guennoc, P., and Sibuet, J.-C., 1979. Northeast Atlantic passive continental margins: rifting and subsidence processes. *In* Talwani, M., Hay, W., and Ryan, W.B.F. (Eds.), *Deep Drilling Results in the Atlantic Ocean: Continental Margins and Paleoenvironment.* Am. Geophys. Union, Maurice Ewing Ser., 3:154–186.

Okada, H., and Bukry, D., 1980. Supplementary modification and introduction of code numbers to the low-latitude coccolith biostratigraphic zonation (Bukry, 1973; 1975). *Mar. Micropaleontol.*, 5:321–325.

Perch-Nielsen, K., 1971. Einige neue Coccolithen aus dem Paläozän der Bucht von Biskaya. *Bull. Geol. Soc. Den.*, 21:347–361.

————, 1985. Cenozoic calcareous nannofossils. *In* Bolli, H.M., Saunders, J.B., and Perch-Nielsen, K. (Eds.), *Plankton Stratigraphy:* Cambridge (Cambridge Univ. Press), 427–554.

Pickup, S.L.B., Whitmarsh, R.B., Fowler, C.M.R., and Reston, T.J., 1996. Insight into the nature of the ocean-continent transition off West Iberia from a deep multichannel seismic reflection profile. *Geology*, 24:1079–1082.

Reston, T.J., Krawczyk, C.M., and Klaeschen, D., 1996. The S reflector west of Galicia (Spain). Evidence for detachment faulting during continental breakup from prestack depth migration. *J. Geophys. Res.*, 101:8075–8091.

Robinson, P.T., Von Herzen, R., et al., 1989. *Proc. ODP, Init. Repts.*, 118: College Station, TX (Ocean Drilling Program).

Sawyer, D.S., Whitmarsh, R.B., Klaus, A., et al., 1994. *Proc. ODP, Init. Repts.*, 149: College Station, TX (Ocean Drilling Program).

Seifert, K., Gibson, I., Weis, D., and Brunotte, D., 1996. Geochemistry of metamorphosed cumulate gabbros from Hole 900A, Iberia Abyssal Plain. *In* Whitmarsh, R.B., Sawyer, D.S., Klaus, A., and Masson, D.G. (Eds.), *Proc. ODP, Sci. Results*, 149: College Station, TX (Ocean Drilling Program), 471–488.

Seifert, K.E., Cheng-Wen, C., and Brunotte, D.A., 1997. Evidence from ODP Leg 149 mafic igneous rocks for oceanic crust in the Iberia Abyssal Plain ocean-continent transition zone. *J. Geophys. Res.*, 102:7915–7928.

Shipboard Scientific Party, 1994a. Site 900. *In* Sawyer, D.S., Whitmarsh, R.B., Klaus, A., et al., *Proc. ODP, Init. Repts.*, 149: College Station, TX (Ocean Drilling Program), 211–262.

————, 1994b. Site 901. *In* Sawyer, D.S., Whitmarsh, R.B., Klaus, A., et al., *Proc. ODP, Init. Repts.*, 149: College Station, TX (Ocean Drilling Program), 263–268.

Sibuet, J.-C., 1992. New constraints on the formation of the non-volcanic continental Galicia-Flemish Cap conjugate margins. *J. Geol. Soc. London*, 149:829–840.

Stork, C., 1992. Reflection tomography in the postmigrated domain. *Geophysics*, 57:680–692.

Stow, D.A.V., and Piper, D.J.W., 1984. Deep-water fine-grained sediments: facies models. *In* Stow, D.A.V., and Piper, D.J.W. (Eds.), *Fine-Grained Sediments: Deep-Water Processes and Facies.* Geol. Soc. Spec. Publ. London, 15:611–645.

Sun, S.-S., and McDonough, W.F., 1989. Chemical and isotopic systematics of oceanic basalts: implications for mantle composition and processes. *In* Saunders, A.D., and Norry, M.J. (Eds.), *Magmatism in the Ocean Basins.* Geol. Soc. Spec. Publ. London, 42:313–345.

Wernicke, B., 1985. Uniform sense normal simple shear of the continental crust. *Can. J. Earth Sci.*, 22:108–125.

Wernicke, B., and Burchfiel, B.C., 1982. Modes of extensional tectonics. *J. Struct. Geol.*, 4:105–115.

Wilson, R.C.L., Sawyer, D.S., Whitmarsh, R.B., Zerong, J., and Carbonell, J., 1996. Seismic stratigraphy and tectonic history of the Iberia Abyssal Plain. *In* Whitmarsh, R.B., Sawyer, D.S., Klaus, A., and Masson, D.G. (Eds.), *Proc. ODP, Sci. Results*, 149: College Station, TX (Ocean Drilling Program), 617–633.

Ms 173-105

NOTE: For all sites drilled, core-description forms ("barrel sheets") and core photographs can be found in Section 3, beginning on page 295. Forms containing smear-slide data, sedimentary thin-section descriptions, and igneous/metamorphic thin-section descriptions can be found on CD-ROM. See Table of Contents for material contained on CD-ROM.

APPENDIX

PRESTACK DEPTH MIGRATION OF SEISMIC REFLECTION PROFILES[3,4,5]

Several east-west multichannel seismic reflection profiles, which cross the ocean/continent transition east of Site 1067, show deep continuous intrabasement reflectors that extend over several kilometers both laterally and vertically (Fig. 2). The reflectors have a geometry on time sections that is consistent with their being important tectonic contacts, possibly low-angle faults. Sites 1067 and 1068 had as their main objective the investigation of one such reflector, the H reflector of Krawczyk et al. (1996), which extends up to near the top of the basement high on which the sites lie (see "Background and Objectives" sections, "Site 1067" and "Site 1068" chapters, this volume).

Knowledge of the precise geometry of these reflectors and, particularly, the location of the H reflector's intersection with the top of acoustic basement were important constraints on the choice of site location. In a region of probable lateral heterogeneity, such as the basement high where the velocity distribution cannot be assumed, it is important to use the best possible velocity model when applying migration algorithms so that the most accurate reflector geometry is obtained, preferably in a depth section. Segments of three different profiles, on which the deep H reflector was clearly seen on time sections, were chosen therefore for the application of prestack depth migration. Prestack depth migration has two main advantages as compared to standard poststack migration (Krawczyk et al., 1996). First, as a migration before stack it avoids the smearing effects of common mid-point (CMP) stacking; such smearing can cause significant distortion of the seismic image in regions of complex geology. Second, it helps to remove effects such as ray-path bending and velocity pull-up/push-down. The processing of the three segments was slightly different in each case and is described briefly below.

Profile Lusigal-12[4]

Profile Lusigal-12 was acquired by *Le Suroît* in 1990 and the whole profile has been presented by Beslier et al. (1995) and Beslier (1996). The profile runs from west to east over Sites 1068, 900, and 1067. The following description of the profile, and of the prestack depth migration applied to it, in the vi-

[3]S.M. Dean, Bullard Labs, Cambridge University, Madingley Road, Cambridge, United Kingdom.

[4]C.M. Krawczyk, Geoforschungs Zentrum Potsdam, Telegrafenberg C2, Potsdam, Federal Republic of Germany.

[5]T.A. Minshull, Bullard Labs, Cambridge University, Madingley Road, Cambridge, United Kingdom.

cinity of Sites 1067 and 1068 (Fig. 2) is taken from Beslier (1996) and Krawczyk et al. (1996), where more details can be found. The source used for the profile was an array of eight 80-in^3 water guns (shot interval 50 m). A 2.4-km, 96-channel streamer with 25-m receiver spacing was used, resulting in a CMP interval of 12.5 m and an average fold of 24. As stacking velocity is not optimal for depth-migrating seismic data, a detailed velocity function was constructed using depth-focusing error analysis applied at closely spaced intervals along the profile (Denelle et al., 1986). This analysis is an essential part of performing depth migration before stack because of the importance of velocity both in converting a time section to depth and in the migration of diffraction and reflection hyperbolae at different offsets in order to produce a final section. Using Migpack software every 10 shotpoints (500 m), a velocity model was created iteratively from the ocean bottom down to deeper levels through depth-focusing error analysis (Krawczyk, 1995). The model is created from top to bottom of the section, determining velocity in one layer at a time because the velocity structure of one layer is affected by the velocity determinations in all overlying levels. As this method relies on clear and strong reflections for reliable focusing of reflected and diffracted energy, it is difficult to determine different velocity layers within the basement where reflections are neither clear, strong, nor laterally extensive. Thus, while the sedimentary layers provide a clear image, as long as highly reflective interfaces are picked, basement was migrated with a nearly constant half-space velocity of 5.5–6.0 km/s, as revealed by the bright reflections within it. The resulting smoothed velocity structure that was used to generate the prestack depth-migrated section is shown in Figure 64 and the resulting depth section is in Figure 10 of the "Introduction" chapter, this volume.

The depth-migrated section shows the H reflector rising from a depth of 9 km toward the basement high. A strong east-dipping seismic reflector can also be seen between 6.5 and 7.5 km below sea level under the crest of the high. One interpretation is that these two reflectors are continuous between shots 4025 and 4060 but are hard to image because of the relatively steep dip of the reflector in that region (Fig. 10, "Introduction" chapter, this volume). Another interpretation, supported by the processed lines CAM146 and CAM159, is that these two reflectors are not continuous but are offset vertically by a steeper reflector. No deeper intrabasement reflector is seen on this profile under the basement high.

Profile CAM146[3]

Profile CAM146 was aligned east-west and passed 3.5 km south of Site 1067 (Fig. 2). The CAM profiles were acquired during *Discovery* cruise 215 in 1995 (Minshull, 1995) using a 6346 in^3 airgun array and a 48-channel streamer with 50-m receiver spacing and 50-s shot interval (~125-m shot spacing). A CMP bin width of 25 m was selected giving an average fold of 10. Processing of CAM146 was carried out at Bullard Labs, Cambridge, using Promax software. Initially, poststack depth migration was applied to construct a depth velocity model based on stacking velocities for the sediment layers and local Ocean Bottom Seismograph (OBS) wide-angle velocities for the lower parts of the section. After various tests, Kirchhoff depth migration was used in preference to a finite difference algorithm, since it proved more successful at imaging the steeply dipping events on the Site 1067 basement high.

Initial prestack depth-migration models used the same velocity structure as the final poststack migration. A migration aperture (maximum offset) of 7.5 km was determined to be a sufficient compromise between computation time and the imaging of dipping events. Unlike Migpack, depth focusing analysis is not available on Promax. Instead, common reflection point (CRP) gathers are used to indicate the existence of an error in velocity above a reflection event and the direction in which the velocity needs to be adjusted (Stork, 1992). Four iterations of velocity adjustment and migration gave the preferred section and the corresponding smoothed velocity model (Fig. 65). The main improvements over the poststack migration were found in the upper basement structure by lowering some velocities across the model. Figure 65 shows a steeply east-dipping reflector between 10 and 12.5 km under the east flank of the Site 1067 high (FFID 6860), which is apparently onlapped at a high angle by the gently west-dipping H reflector at a depth of 10 km. The deepest reflector on the section (at ~14.5–16.5 km depth) is reflector L.

Profile CAM159[5]

Profile CAM159 was aligned northeast-southwest and passed within 3.2 km of Site 1067 (Fig. 2). Details of the acquisition parameters for the CAM lines are given in the previous section. The shot spacing along the depth-migrated part of CAM159 closest to Site 1067 was ~103 m; for convenience in processing, a 100-m shot interval was assumed, since the resulting distortion is negligible. Semblance velocity analyses were conducted at ~1 km intervals and velocities were then smoothed to provide a model for the first migration. Migrations were carried out using Promax 6.1 at the Instituto de Ciencias de la Tierra "Jaume Almera" in Barcelona. The velocity model was refined for subsequent migration runs by perturbing velocities to improve the horizontal alignment of migrated CRP gathers. Examination of these gathers provides information on the direction of velocity perturbation required, but not the magnitude, so successive stages gave only minor improvements in the depth-migrated image. The final depth-migrated section and the velocity model used for migration are shown in Figure 66.

The H reflector can be seen as a concave upward feature between FFID 11400 and 11490, at a depth of 8.5–10.0 km. As on CAM146, the H reflector appears to intersect a steeper east-dipping reflector at about FFID 11400, but at a more acute angle. Neither reflector can be followed to the top of acoustic basement. However, this observation may be the result of the oblique angle between the north-northeast–trending basement ridge on which Site 1067 lies and the track of CAM159. The L reflector is not seen clearly on this section.

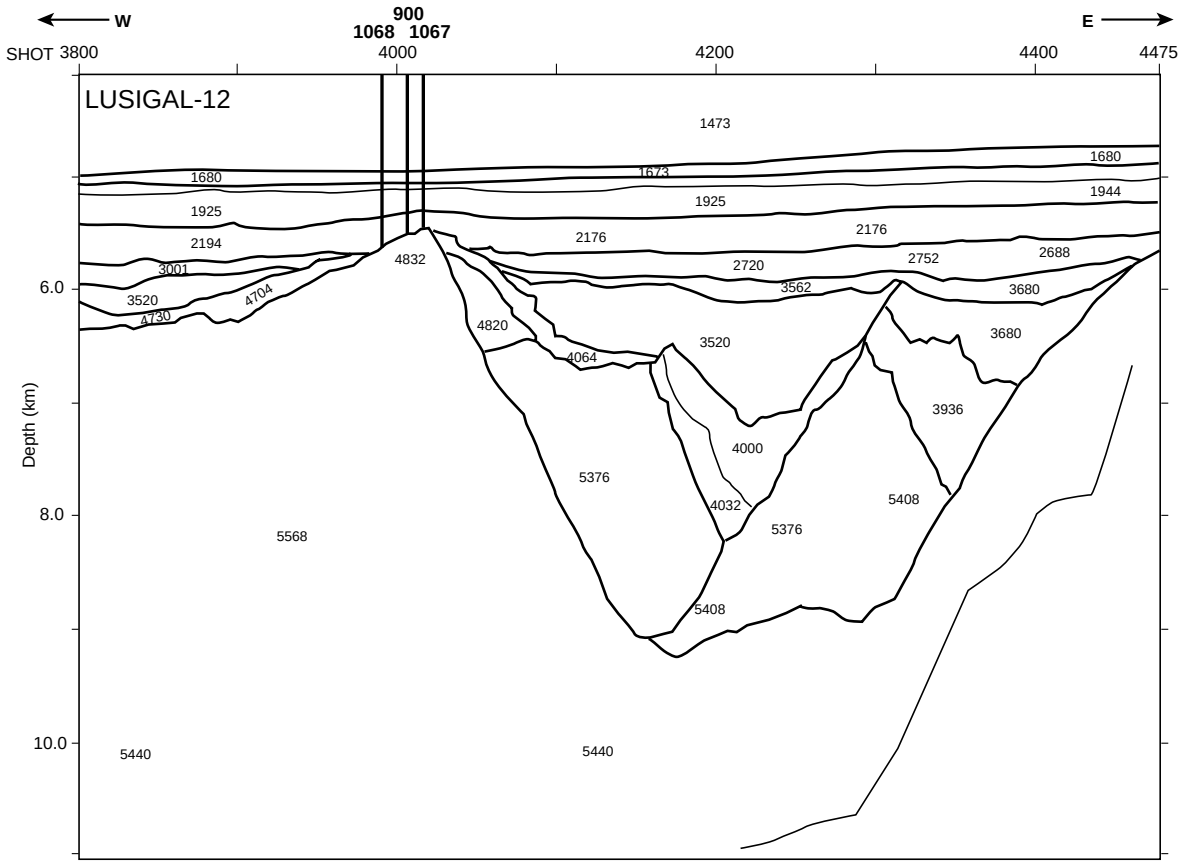

Figure 64. Velocity model from depth-focusing analysis (C.M. Krawczyk, pers. comm., 1995) used to prestack depth migrate the section displayed in Figure 10, “Introduction” chapter (this volume). Locations of Sites 900, 1067, and 1068 are indicated.

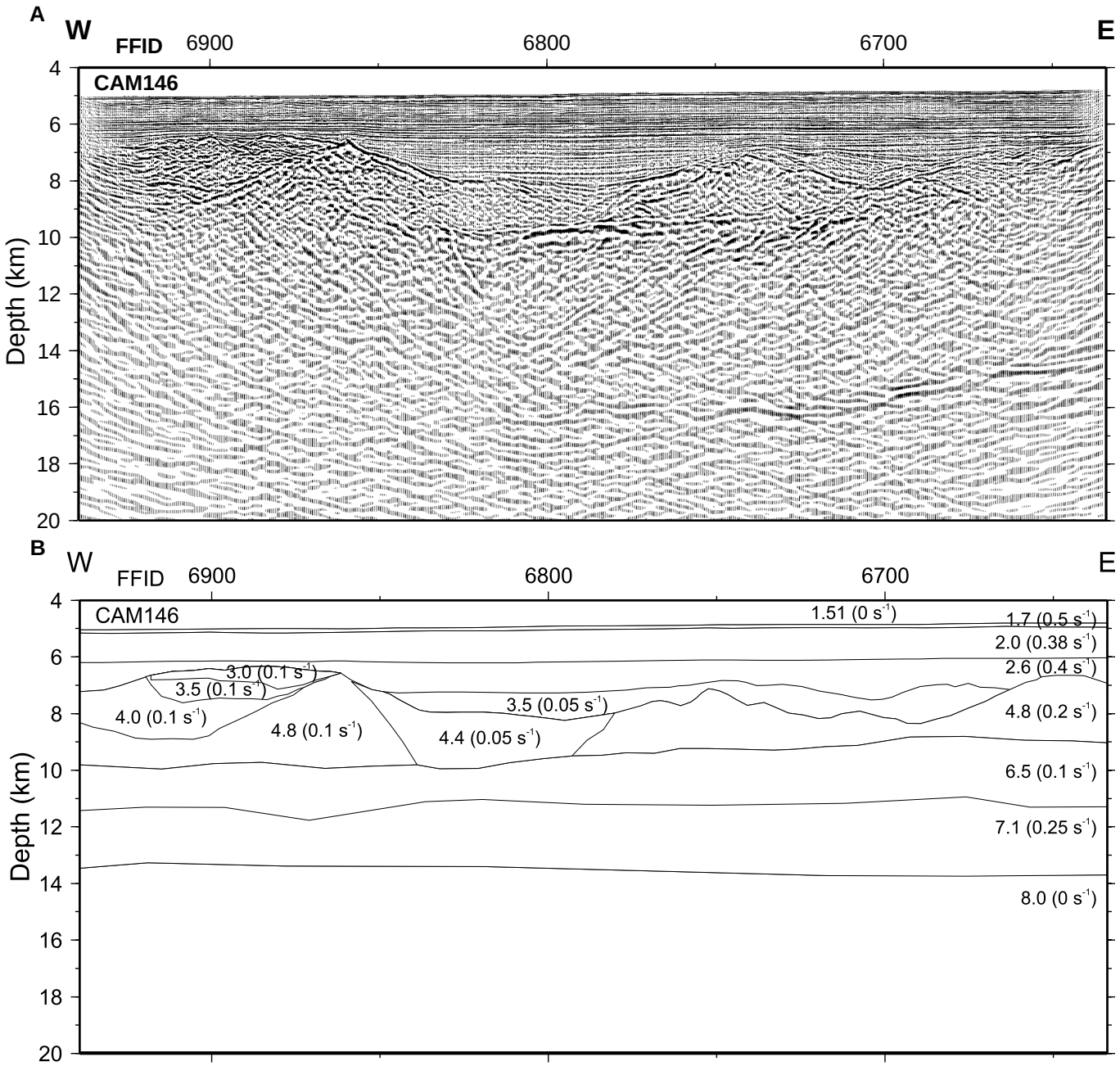

Figure 65. **A.** Multichannel seismic reflection profile CAM146 processed by S. Dean using Kirchhoff poststack depth migration. No vertical exaggeration. The profile crosses the southern edge of the triangular basement high on which Sites 1067, 1068, and 900 are located (left half of the figure). **B.** Velocity model used in the migration process. Migration velocities in kilometers per second; numbers in parentheses indicate vertical gradients in meters per second per kilometer.

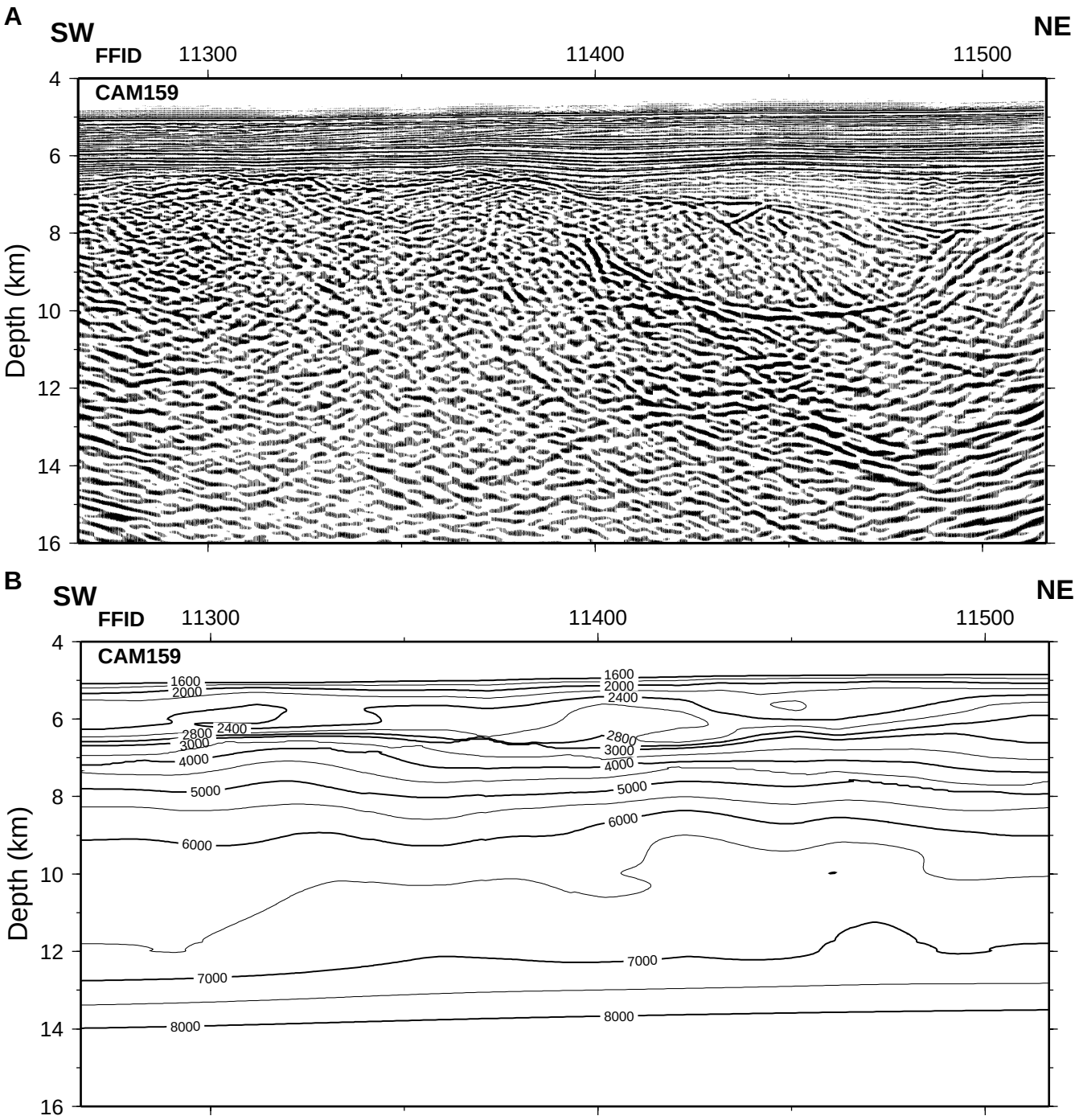

Figure 66. **A.** Multichannel seismic reflection profile CAM159 processed by T.A. Minshull using prestack depth migration. The profile crosses the south and southeast flank of the basement high on which Sites 1067, 1068, and 900 lie. Displayed section is at true scale (no vertical exaggeration) and true amplitude. **B.** Smoothed velocity model used in the prestack depth migration process; isovelocity contours in meters per second.

Prior Chapter Contents Next Chapter